NRL/5340/FR--2022/3

Calibration and Optimization of a Wideband Circular Array Using a Phase-Mode Beamformer

DAN P. SCHOLNIK

Surveillance Technology Branch
Radar Division

December 15, 2021

PLEASE DO NOT RETURN YOUR FORM TO THE ABOVE ORGANIZATION

1. REPORT DATE 12-15-2021	2. REPORT TYPE NRL Formal Report	3. DATES COVERED	
		START DATE 10-01-2018	**END DATE** 12-31-2021

4. TITLE AND SUBTITLE
Calibration and Optimization of a Wideband Circular Array Using a Phase-Mode Beamformer

5a. CONTRACT NUMBER	5b. GRANT NUMBER	5c. PROGRAM ELEMENT NUMBER 62271N
5d. PROJECT NUMBER	**5e. TASK NUMBER** EW-271-001	**5f. WORK UNIT NUMBER** 6B48

6. AUTHOR(S)
Dan P. Scholnik

7. PERFORMING ORGANIZATION / AFFILIATION NAME(S) AND ADDRESS(ES) U. S. Naval Research Laboratory 4555 Overlook Avenue, SW Washington, DC 20375-5320	8. PERFORMING ORGANIZATION REPORT NUMBER NRL/5340/FR--2022/3

9. SPONSORING / MONITORING AGENCY NAME(S) AND ADDRESS(ES) Office of Naval Research One Liberty Center 875 N. Randolph Street, Suite 1425 Arlington, VA 22203-1995	10. SPONSOR / MONITOR'S ACRONYM(S) ONR	11. SPONSOR / MONITOR'S REPORT NUMBER(S)

12. DISTRIBUTION / AVAILABILITY STATEMENT
DISTRIBUTION STATEMENT A. Approved for public release. Distribution is unlimited.

13. SUPPLEMENTAL NOTES

14. ABSTRACT
Circular and cylindrical arrays are advantageous when 360-degree azimuthal coverage is desired, as they do not suffer the angle-dependent beam broadening and scan loss characteristic of linear and planar arrays. A phase-mode beamformer (implemented as a Butler matrix) transforms an ideal wideband circular array into a frequency-invariant virtual linear array, greatly simplifying wideband beamforming. The nonideal responses of a physical analog beamformer and antenna elements, however, necessitate equalization to realize this frequency invariance. In this report, we first define a signal-processing model of the entire beamformer system, from antenna to final array weights. For the array, Butler matrix, and equalization filters, we define error metrics which can be used to evaluate the relative contributions of each component to the overall error. We focus on the design and performance of equalization filters located at the phase mode outputs, that can be implemented either as analog tapped-delay-line (TDL) filters or as digital FIR filters. We then compare wideband array patterns from the system using standard tapers, optimized array weights, and adaptive beamforming.

15. SUBJECT TERMS
circular arrays, phase-modes, phase-mode beamformer, wideband adaptive beamforming

16. SECURITY CLASSIFICATION OF:			17. LIMITATION OF ABSTRACT UU	18. NUMBER OF PAGES 98
a. REPORT U	**b. ABSTRACT** U	**c. THIS PAGE** U		

19a. NAME OF RESPONSIBLE PERSON Dan P. Scholnik	19b. PHONE NUMBER *(Include area code)* 202-404-1943

This page intentionally left blank

CONTENTS

FIGURES

TABLES

EXECUTIVE SUMMARY

This report documents the signal-processing and beamforming aspects of the NRL 6.2 Base project "Transmit and Receive Wideband Adaptive Nulling for Cylindrical Phased Array Antennas" (WU 6B48), which ran from October 2018 through December 2021. The project was developed in order to show the potential advantages of using a phase-mode beamformer to drive and receive from a circular or cylindrical array, particularly for wideband operation. One major component of this effort was the actual hardware design of the phase-mode beamformer (in the form of a wideband Butler matrix) along with the array and a tapped-delay-line filter for mode equalization; these efforts were documented separately in yearly reports[1][2][3]. This report then uses those designs as building blocks for a full system simulation, illustrating the general phase-mode theory and tying it together with analysis and design techniques developed during the project.

Phase-mode analysis is essentially the application of Fourier-series analysis to the periodic response of a circular array in azimuth. The advantage of phase-mode analysis is that it provides a way to separate the effects of the individual elements from the behavior of the entire array, much in the spirit of the array factor in linear and planar arrays. The end result is a virtual linear-array model of the circular array, with the phase modes serving as the virtual elements. A major distinction from true linear arrays is that the ideal phase-mode model is frequency invariant and thus suitable for wideband operation without time-delay steering. Phase-mode analysis is not a new concept, but here we go beyond the usual analysis to develop a detailed error model for each major component of the system. An error model for the array itself already exists in terms of "distortion modes," which are higher-order modes that alias onto the desired modes somewhat like grating lobes in a planar array. This model is paired here with a new error model for the Butler matrix; the latter measures undesired mixing between the desired modes. A unified error model including both the array and the Butler matrix is then derived and related to the Fourier series of the patterns induced by the Butler matrix. This provides the ability to quantify errors for each component separately even when individual characterizations are not practical or available. Finally, an error model for the equalization filters required to combine the phase modes is derived.

The virtual-array model of a phase-mode beamformer can be flipped to provide circular array synthesis of wideband beams. Ideal synthesis using the virtual linear array is straightforward, but here we consider design procedures for nonideal hardware. We first consider the design of equalization filters, both in the form of digital FIR filters and analog tapped-delay-line filters depending on where array digitization takes place. Basic optimization approaches suffice for the FIR filters, but the nonideal hardware responses of the TDL filters, including amplitude/phase quantization, require more-complicated iterative procedures. Once the EQ filters are designed, then we can incorporate the nonideal system responses into optimal beamforming weight design in either a deterministic or adaptive framework, both of which are presented.

[1]R. Mital, M. P. Parent, and A. Stumme, "Circular Array Beamforming Using Phase Modes," Memorandum Report NRL/MR/5317–19-9908, US Naval Research Laboratory, Washington, DC, Dec. 2019.

[2]R. Mital, W. R. Pickles, and M. G. Parent, "Design and Development of Butler Matrices for Circular Array Beamforming," Memorandum Report NRL/MR/5317–20-10,130, US Naval Research Laboratory, Washington, DC, Sept. 2020.

[3]R. Mital and W. R. Pickles, "Final Report on Modal Beamformers using Passive Butler Matrices," Memorandum Report NRL/IR/5317–21-13-U, US Naval Research Laboratory, Washington, DC, Dec. 2021. In review.

The general analysis and synthesis tools developed in the early chapters of the report are then applied to the simulated system responses from the hardware component of this project. This includes two 16-element arrays: a basic dipole array, and a stepped-notch array, a 16 × 16 wideband Butler matrix, and 8-tap FIR and TDL equalization filters. Each piece of hardware is individually characterized, and equalization-filter coefficients are designed for both FIR and TDL cases, the latter incorporating commercial, off-the-shelf attenuators and phase-shifters. With EQ filters characterized, as series of deterministic and adaptive beamforming designs is shown, characterizing the performance bounds and the effects of hardware errors on performance. In the process, it is shown that a circular array has the ability to perform localization in both azimuth and elevation, which is not the case for a true linear array.

CALIBRATION AND OPTIMIZATION OF A WIDEBAND CIRCULAR ARRAY USING A PHASE-MODE BEAMFORMER

1. INTRODUCTION

Circular and cylindrical arrays have attractive properties for applications that require 360° surveillance in azimuth, since their inherent symmetry ensures no significant deviation in performance across angle. This stands in contrast to linear and planar arrays, which must be deployed in sets of three or more to provide continuous coverage and require various tradeoffs due to degraded performance at off-boresight angles [1, 2]. Nonetheless, over the years, planar arrays have proliferated, while circular arrays seem to have remained largely a niche architecture despite the ever-growing need for 360° coverage. This sentiment itself is not new, having been expressed nearly 40 years prior [3]. Presumably, the historical aversion has been due to some combination of mechanical and manufacturability concerns, the perceived higher analytical difficulty vis-à-vis planar arrays, and simple herd mentality.

All that notwithstanding, circular arrays have seen somewhat of a revival in interest in recent years. Despite the fact that much of the foundational analysis on circular arrays took place in the 1950's and 1960's [3; 4, Ch. 2], over half (785/1531) of the papers returned from an IEEE search for "circular array" were published between 2011 and 2020. Applications include radar surveillance [5, 6], polarimetric weather radar [7, 8], source localization and direction-of-arrival (DOA) estimation [9, 10], and communications [11, 12].

1.1 Circular-Array Phase Modes — The Elevator Pitch

Because phase modes are so central to this project and report, it seems appropriate to offer some motivation up front before asking the reader to wade through to the math in Section 3.2, where they are formally described. Phase modes in circular arrays result from applying Fourier-series analysis to the element and array patterns in azimuth, which are inherently periodic with period 2π. Phase modes play much the same role in circular arrays that the Fourier transform plays in linear and planar arrays to separate the effects of the element patterns from the array factor due to the weights applied to the elements. Indeed, the key result of phase-mode analysis is that it allows us to represent the circular array mathematically as an equivalent linear array, where the modes themselves play the role of the elements. This virtual array exhibits inherent frequency invariance with simple complex weights applied to each "element" (mode); that is, the beamshape (including nulls) and direction are nominally constant across possibly wide frequency ranges. This is in contrast to a physical linear array, in which the beamwidth narrows and the mainbeam and null directions "squint" toward boresight with increasing frequency. To obtain similar frequency invariance in linear arrays requires custom filters at each element [13], which significantly complicates real-time processing such as adaptive filtering. Thus, in addition to 360° azimuth coverage, circular arrays offer wideband performance with potentially reduced complexity compared to linear arrays.

Phase-mode beamformers can be realized in analog, digitally, or as a hybrid approach. In analog form, they consist of a Butler matrix and (fixed) tapped-delay-line equalization filters, while the digital equivalents

are a DFT and FIR filters. The usual tradeoffs between analog and digital hardware apply; analog offers significant inherent parallelism at the cost of lower precision and stability. Here the focus is on analog implementations and their design and error modeling, with the digital implementations serving as an ideal reference for comparison.

1.2   Relationship to Orbital Angular Momentum Modes

Traditional circular arrays, and those of interest in this project, are designed with the horizon as the nominal boresight direction, and with elements that are uniformly spaced and rotated about the *z*-axis and radiate outward from the center. There is, however, a second circular array geometry that makes heavy use of the terminology of "modes," which is associated with the nascent (and controversial) concept of RF "orbital angular momentum" (OAM) beams [14, 15]. OAM is a terminology borrowed from quantum mechanics and used primarily in the field of optics to describe light beams with a rotating phase front. For this reason, OAM beams are also sometimes referred to as "vortex" beams. They were recently introduced in the RF world [16], initially using modified dish antennas and then later using circular arrays. An OAM "mode" can be generated by driving the elements of a circular array with a conventional phase mode input of the same index, with the key differences that here the element (and array) boresight direction is oriented along the *z*-axis rather than in the *x*-*y* plane, and the elements are not sequentially rotated about the *z*-axis. (Effectively, it is a planar array with the elements arranged around a circle, rather than a true circular array.) The periodic phase characteristic of the phase mode now encircles boresight, rather than the horizon. This geometry implies, among other things, that the corresponding far-field pattern has a boresight null for all OAM modes other than $m = 0$.

The primary claim made in the OAM literature is that, since OAM modes of different indices are orthogonal, they provide virtually unlimited ability to multiplex data signals and increase communications capacity in a given spectral band. Unfortunately, as the terminology implies, these claims were initially made by physicists with little to no background in communications, antennas, or signal processing. Upon examination, it was evident to relevant experts that what was being described was, in fact, merely a special case of the more general field of multiple-input, multiple-output (MIMO) communications [17–19]. While this was disputed by the original authors [20], it is generally accepted within the engineering community. Other problems with the OAM claims were amply documented from the perspectives of thermodynamics [21], fundamental antenna/electromagnetics theory [19, 22], and communications link budgets [23]. These all generally stem from the boresight null, which makes the beams unsuitable for far-field propagation as the amount of power received by a fixed-size antenna falls off much faster than $1/R^2$ as it falls further into the null with increasing range. This is in agreement with MIMO communication theory, which is reliant on multipath to effectively extend the near field out to what would be far-field distances in line-of-sight communication. Unfortunately, OAM multiplexing as generally described cannot benefit from multipath, as it depends on precise steering of the null on the receiving antenna [24] and has no provisions for spatial equalization.

Despite these well-documented problems and the lack of any credible rebuttal, the numbers of papers focusing on OAM applications to communications and imaging have not tapered off as one might have expected. Some of this is due to the proliferation of "pay-for-play" journals of dubious quality and standards, but plenty can still be found in reputable IEEE journals as well. The IEEE's *Transactions on Antennas and Propagation* and *Antennas and Wireless Propagation Letters* are home to many such papers. The applications have extended to radar as well [25], with the claims at best appearing to mirror MIMO radar results. What's worse, because the OAM "community" has effectively isolated itself from the greater antenna/communication/radar community, they are now reinventing well-known results such as phase-mode beam synthesis in the name of OAM [26].

1.3   Project Background and Report Overview

NRL has a strong record of research in circular arrays, both historically [27] and more recently [5, 6, 11, 28–30]. The NRL Base project "Transmit and Receive Wideband Adaptive Nulling for Cylindrical Phased Array Antennas" (WU 6B48) was developed in order to show the potential advantages of using a phase-mode beamformer to drive and receive from a circular or cylindrical array. The major thrust of this project was proof-of-concept development of suitable hardware for phase-mode beamforming. In this vein, yearly project reports documented the early design of a 16-element circular array and a 4 × 4 Butler matrix [31], the design of wideband phase shifters and an 8 × 8 Butler matrix [32], and the fabrication and testing of the 4 × 4 and 8 × 8 Butler matrices [33]. The final hardware report [33] also included a chapter on beamforming using both 8-element and 16-element arrays. Hardware limitations and delays due to the 2020-2021 COVID pandemic regrettably precluded fabrication and test of a 16×16 Butler matrix in combination with wideband equalization and a suitable array. However, the hardware efforts did produce simulated responses for both the Butler matrix and two different 16-element arrays. In addition, we have simulated responses for an 8-output tapped delay line and an 8 × 1 combiner, which can be used along with suitable attenuators and phase shifters to create tapped-deay-line (TDL) equalizer filters.

This report, intended to complement the hardware efforts, serves both to document the signal-processing aspects of a general modal beamformer system and to use the simulated responses from this project as the basis for a full system simulation. The report proceeds as follows: Chapter 2 establishes much of the mathematical notation and convention for the rest of the report, and contains general background material on wideband array analysis which will be used throughout the report. Chapter 3 provides a general phase-mode analysis of the uniform circular array (UCA), including analysis and synthesis and the representation of the UCA as a virtual linear array. Of particular note is the error analysis of Section 3.4, which incrementally builds an error model for a phase-mode system that independently accounts for errors from the array itself, the Butler matrix, and the equalization filtering. This chapter also includes analysis of the noise spectral density at each modal output, showing that it will not necessarily be white as typically assumed in uniform linear arrays. Chapter 4 focuses on wideband equalization filter design, which is critical to achieving frequency invariance. Here both digital (FIR) and analog (TDL) filter structures are considered, along with optimization techniques geared towards the hardware limitations in the latter case. Finally, in Chapter 5, we present the results of simulating the full system from array elements through beamforming, and apply the error analysis to the system and components.

2.   BACKGROUND

In this chapter, we will cover background material that will be needed for the rest of the report. We first review different notations and conventions for space-time and Fourier signal descriptions, which will be used extensively. We then introduce the Cartesian and spherical coordinate systems for describing arrays. We review the definitions of the wideband transmit and receive antenna pattern, and define some basic operations that can be used to generate wideband array patterns. This section may be lightly skimmed or skipped altogether for those familar with the topics.

2.1   Space-Time Fourier Notation and Conventions

A discussion on notation for space-time signals and their frequency-domain representations might be helpful here, as there are many competing conventions. A real scalar plane wave with frequency f_0 traveling in the $\hat{\mathbf{u}}_0$ direction can described variously as

$$p(\mathbf{x}, t) = \cos\left(2\pi\left(f_0 t - \frac{1}{\lambda_0}\hat{\mathbf{u}}_0^\mathsf{T}\mathbf{x}\right)\right) = \mathrm{Re}\left\{e^{\mathrm{j}2\pi\left(f_0 t - \frac{1}{\lambda_0}\hat{\mathbf{u}}_0^\mathsf{T}\mathbf{x}\right)}\right\} \tag{1a}$$

$$= \cos\left(2\pi\left(f_0 t - \mathbf{v}_0^\mathsf{T}\mathbf{x}\right)\right) \quad = \mathrm{Re}\left\{e^{\mathrm{j}2\pi\left(f_0 t - \mathbf{v}^\mathsf{T}\mathbf{x}\right)}\right\} \tag{1b}$$

$$= \cos\left(\omega_0 t - \mathbf{k}_0^\mathsf{T}\mathbf{x}\right) \quad = \mathrm{Re}\left\{e^{\mathrm{j}\omega_0 t - \mathrm{j}\mathbf{k}_0^\mathsf{T}\mathbf{x}}\right\} \tag{1c}$$

$$= \cos\left(\mathbf{k}_0^\mathsf{T}\mathbf{x} - \omega_0 t\right) \quad = \mathrm{Re}\left\{e^{\mathrm{j}\mathbf{k}_0^\mathsf{T}\mathbf{x} - \mathrm{j}\omega_0 t}\right\}, \tag{1d}$$

where $\omega_0 = 2\pi f_0$ is the radian frequency, $\lambda_0 = \frac{c}{f_0}$ is the wavelength of the plane wave with propagation speed c, $\mathbf{v}_0 = \frac{1}{\lambda_0}\hat{\mathbf{u}}_0$ is the spatial frequency, and $\mathbf{k}_0 = \frac{2\pi}{\lambda_0}\hat{\mathbf{u}}_0$ is the *vector wavenumber*. As seen in Eq. (1d), since the cosine function is even symmetric, the arguments can all be negated without effect. While real fields describe our physical reality, the complex fields inside the braces on the right are far more convenient to operate on mathematically, and as such are almost always used in analysis with the outer real-part operator merely implied. Of these conventions, Eqs. (1a) and (1b) are more common among electrical engineers, while Eqs. (1c) and (1d) are used more often in physics and mathematics as well as by engineers focusing on electromagnetics and antennas. These generally mirror corresponding conventions regarding the Fourier transform, with engineers preferring

$$H(f) = \int h(t)e^{-\mathrm{j}2\pi f t}\mathrm{d}t$$

$$h(t) = \int H(f)e^{\mathrm{j}2\pi f t}\mathrm{d}f$$

and math and physics preferring radian frequency with no clear preference as to sign convention:

$$H(\omega) = \int h(t)e^{\pm\mathrm{j}\omega t}\mathrm{d}t$$

$$h(t) = \frac{1}{2\pi}\int H(\omega)e^{\mp\mathrm{j}\omega t}\mathrm{d}\omega$$

Extending the Fourier transform to space-time offers another layer of notational headache, as one must decide how to handle the sign difference between the temporal and spatial variables in the plane-wave definition.

There are at least three different aproaches at large. For narrowband analysis, the temporal dependence is often factored out and largely ignored; here only a spatial transform of any convention is performed and the sign mismatch can be hidden in the temporal factor. A second approach is the straightforward multidimensional extension of the engineering Fourier convention:

$$H(\mathbf{v},f) = \iint h(\mathbf{x},t)\mathrm{e}^{-\mathrm{j}2\pi\left(ft+\mathbf{v}^\mathsf{T}\mathbf{x}\right)}\,\mathrm{d}\mathbf{x}\,\mathrm{d}t$$

$$h(\mathbf{x},t) = \iint H(\mathbf{v},f)\mathrm{e}^{\mathrm{j}2\pi\left(ft+\mathbf{v}^\mathsf{T}\mathbf{x}\right)}\,\mathrm{d}\mathbf{v}\,\mathrm{d}f,$$

which maintains the usual description of temporal frequency but requires defining spatial frequency as $\mathbf{v} = -\frac{1}{\lambda}\hat{\mathbf{u}}$ to be consistent with propagation. The author has previously made use of this convention [13, 34, 35]. A third, related approach is simply to move the negation into the definition of the transform to explicitly make the Fourier basis functions match the form of a plane wave:

$$H(\mathbf{v},f) = \iint h(\mathbf{x},t)\mathrm{e}^{-\mathrm{j}2\pi\left(ft-\mathbf{v}^\mathsf{T}\mathbf{x}\right)}\,\mathrm{d}\mathbf{x}\,\mathrm{d}t$$

$$h(\mathbf{x},t) = \iint H(\mathbf{v},f)\mathrm{e}^{\mathrm{j}2\pi\left(ft-\mathbf{v}^\mathsf{T}\mathbf{x}\right)}\,\mathrm{d}\mathbf{v}\,\mathrm{d}f.$$

This is the convention we will use here, as it slightly simplifies notation. Hereafter we will simply write $h \leftrightarrow H$ to indicate a transform pair. Under this convention, we have $\mathrm{e}^{\mathrm{j}2\pi\left(f_0 t - \mathbf{v}_0^\mathsf{T}\mathbf{x}\right)} \leftrightarrow \delta(\mathbf{x} - \mathbf{x}_0, f - f_0)$, an impulse at $(\mathbf{x}_0, f_0)$, as we might intuitively expect. For the most part, other Fourier transform properties are independent of the convention in use. For example:

$$(\mathbf{a} \circledast \mathbf{b})(\mathbf{x},t) \longleftrightarrow \mathbf{A}(\mathbf{v},f)\mathbf{B}(\mathbf{v},f) \qquad \text{convolution} \qquad (2a)$$

$$\mathbf{a}(\mathbf{0},t) \longleftrightarrow \int \mathbf{A}(\mathbf{v},f)\,\mathrm{d}\mathbf{v} \qquad \text{zero-sampling} \qquad (2b)$$

$$\mathbf{a}(-\mathbf{x},t) \longleftrightarrow \mathbf{A}(-\mathbf{v},f) \qquad \text{space/time/frequency reversal} \qquad (2c)$$

$$\mathbf{a}(\mathbf{Tx},t) \longleftrightarrow |\mathbf{T}|^{-1}\mathbf{A}(\mathbf{T}^{-\mathsf{T}}\mathbf{v},f) \qquad \text{linear transformation.} \qquad (2d)$$

We will use $\circ$ and $*$ to indicate convolution in only the spatial or temporal dimension when needed. The only Fourier property of interest here that does depend on the sign convention is space-time shifts:

$$\mathbf{a}(\mathbf{x} - \mathbf{x}_0, t - t_0) \longleftrightarrow A(\mathbf{v},f)\mathrm{e}^{\mathrm{j}2\pi(\mathbf{v}^\mathsf{T}\mathbf{x}_0 - f t_0)} \qquad \text{space-time shift,} \qquad (2e)$$

where the signs are mismatched in space and time corresponding to the Fourier basis convention.

2.2   Geometry

Figure 1 shows the various Cartesian and spherical coordinate systems commonly used to describe antenna geometries and patterns. Following radar conventions, far-field azimuth angle ϕ is measured clockwise from

the *y* axis (north), while elevation angle θ is measured up from the *x-y* plane. We will use Cartesian unit vectors $\hat{\mathbf{u}}$ and az/el pairs (ϕ, θ) interchangeably to describe directions in 3D, via the mappings

$$\hat{\mathbf{u}} = \begin{bmatrix} \hat{u}_x \\ \hat{u}_y \\ \hat{u}_z \end{bmatrix} = \begin{bmatrix} \cos(\theta)\sin(\phi) \\ \cos(\theta)\cos(\phi) \\ \sin(\theta) \end{bmatrix} \qquad \longleftrightarrow \qquad \begin{pmatrix} \phi = \tan^{-1}(\hat{u}_x, \hat{u}_y) \\ \theta = \sin^{-1}(\hat{u}_z) \end{pmatrix}.$$

Local Cartesian unit vectors $\hat{\boldsymbol{\phi}}(\hat{\mathbf{u}})$ and $\hat{\boldsymbol{\theta}}(\hat{\mathbf{u}})$ indicate the directions of increasing azimuth and elevation, and provide a basis for the plane normal to $\hat{\mathbf{u}}$. These are frequently used to describe orthogonal polarization components, with $\hat{\boldsymbol{\phi}}$ representing horizontal polarization and $\hat{\boldsymbol{\theta}}$ representing vertical polarization. The unit vectors are given by

$$\hat{\boldsymbol{\phi}} = \begin{bmatrix} \cos(\phi) \\ -\sin(\phi) \\ 0 \end{bmatrix} = \frac{1}{\sqrt{\hat{u}_x^2+\hat{u}_y^2}} \begin{bmatrix} \hat{u}_y \\ -\hat{u}_x \\ 0 \end{bmatrix} \qquad \hat{\boldsymbol{\theta}} = \hat{\boldsymbol{\phi}} \times \hat{\mathbf{u}} = \begin{bmatrix} -\sin(\theta)\sin(\phi) \\ -\sin(\theta)\cos(\phi) \\ \cos(\theta) \end{bmatrix} = \frac{1}{\sqrt{\hat{u}_x^2+\hat{u}_y^2}} \begin{bmatrix} -\hat{u}_x\hat{u}_z \\ -\hat{u}_y\hat{u}_z \\ \hat{u}_x^2 + \hat{u}_y^2 \end{bmatrix},$$

with the symmetry relationships

$$\hat{\mathbf{u}}(\phi + 180°, -\theta) = -\hat{\mathbf{u}}(\phi, \theta) \tag{3a}$$

$$\hat{\boldsymbol{\phi}}(-\hat{\mathbf{u}}) = -\hat{\boldsymbol{\phi}}(\hat{\mathbf{u}}) \tag{3b}$$

$$\hat{\boldsymbol{\theta}}(-\hat{\mathbf{u}}) = \hat{\boldsymbol{\theta}}(\hat{\mathbf{u}}). \tag{3c}$$

It will be convenient to define a projection matrix into the plane normal to $\hat{\mathbf{u}}$ as

$$\boldsymbol{\Gamma}_{\hat{\mathbf{u}}} = \begin{bmatrix} \hat{\boldsymbol{\phi}} & \hat{\boldsymbol{\theta}} \end{bmatrix} \begin{bmatrix} \hat{\boldsymbol{\phi}}^{\mathsf{T}} \\ \hat{\boldsymbol{\theta}}^{\mathsf{T}} \end{bmatrix}$$

such that $\boldsymbol{\Gamma}_{\hat{\mathbf{u}}}\vec{\mathbf{A}}(\hat{\mathbf{u}})$ has only transverse components.
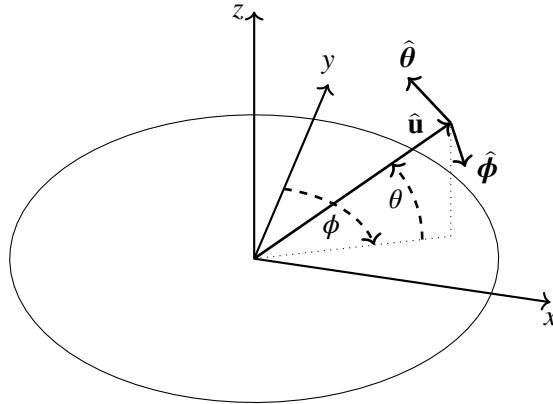
Fig. 1—Coordinate systems used for describing the array geometry and its far-field pattern

Given some far-field vector function of direction $\vec{\mathbf{A}}$, we can define the horizontal and vertical polarization components as

$$
\begin{bmatrix} A_\phi(\hat{\mathbf{u}}) \\ A_\theta(\hat{\mathbf{u}}) \end{bmatrix} \triangleq \begin{bmatrix} \hat{\boldsymbol{\phi}}^\mathsf{T}(\hat{\mathbf{u}}) \\ \hat{\boldsymbol{\theta}}^\mathsf{T}(\hat{\mathbf{u}}) \end{bmatrix} \vec{\mathbf{A}}(\hat{\mathbf{u}}).
$$

It is customary to define polarization states as linear combinations of these components, generally in orthogonal pairs such as

$$
\begin{bmatrix} A_\mathrm{co} \\ A_\mathrm{xp} \end{bmatrix} = \begin{bmatrix} \boldsymbol{\psi}_\mathrm{co}^\mathsf{H} \\ \boldsymbol{\psi}_\mathrm{xp}^\mathsf{H} \end{bmatrix} \begin{bmatrix} \hat{\boldsymbol{\phi}}^\mathsf{T}(\hat{\mathbf{u}}) \\ \hat{\boldsymbol{\theta}}^\mathsf{T}(\hat{\mathbf{u}}) \end{bmatrix} \vec{\mathbf{A}}(\hat{\mathbf{u}}) \qquad \longleftrightarrow \qquad \vec{\mathbf{A}}(\hat{\mathbf{u}}) = \begin{bmatrix} \hat{\boldsymbol{\phi}}(\hat{\mathbf{u}}) & \hat{\theta}(\hat{\mathbf{u}}) \end{bmatrix} \begin{bmatrix} \boldsymbol{\psi}_\mathrm{co} & \boldsymbol{\psi}_\mathrm{xp} \end{bmatrix} \begin{bmatrix} A_\mathrm{co} \\ A_\mathrm{xp} \end{bmatrix},
$$

where 2×1 complex vectors $\boldsymbol{\psi}_\mathrm{co}$ and $\boldsymbol{\psi}_\mathrm{xp}$ are known as a *Jones vectors* [36]. Some common values of Jones vectors are

Name	linear (H)	linear (V)	linear (SR)	linear (SL)	circular (RH)	circular(LH)
Jones vector (TX Ref.)	$\begin{bmatrix} 1 \\ 0 \end{bmatrix}$	$\begin{bmatrix} 0 \\ 1 \end{bmatrix}$	$\frac{1}{\sqrt{2}}\begin{bmatrix} 1 \\ 1 \end{bmatrix}$	$\frac{1}{\sqrt{2}}\begin{bmatrix} 1 \\ -1 \end{bmatrix}$	$\frac{1}{\sqrt{2}}\begin{bmatrix} 1 \\ -\mathrm{j} \end{bmatrix}$	$\frac{1}{\sqrt{2}}\begin{bmatrix} 1 \\ \mathrm{j} \end{bmatrix}$

Jones vectors can be specified from the point of view of either the transmitter or receiver, which inverts the definition of $\hat{\mathbf{u}}$. As a consequence of Eqs. (3b) and (3c), we have

$$
\boldsymbol{\psi}_\mathrm{RX} = \begin{bmatrix} -1 & 0 \\ 0 & 1 \end{bmatrix} \boldsymbol{\psi}_\mathrm{TX},
$$

which has no effect on vertical or horizontal polarization individually but flips all other polarizations with a left-right orientation.

2.3   Wideband Antenna Patterns

In this section, we introduce the wideband array pattern, which will be our principal means of characterizing arrays in the sequel. We first derive the wideband pattern for a general single-feed antenna element operating in transmit mode, and then show that reciprocity yields the same characterization on receive.

2.3.1   *Transmit*

The wideband antenna pattern $\vec{\mathbf{A}}(\hat{\mathbf{u}}, f)$ is a space-time transfer function between the antenna drive signal and the resulting propagating fields in the Fraunhofer (far-field) region. In this section, we will derive the pattern from a transmit perspective; thus, the input is a temporal drive signal $s(t)$ with transform $S(f)$ while the output is the far-field electric field. We will assume deterministic signals for simplicity, but a parallel derivation for random processes yields the same pattern definition [34]. Assuming that the antenna is linear and time-invariant, the current density that results from s can be written as

$$
\vec{\mathbf{j}}(\mathbf{x}, t) = (\mathbf{h} * s)(\mathbf{x}, t)
$$
$$
\vec{\mathbf{J}}(\mathbf{v}, f) = \mathbf{H}(\mathbf{v}, f) S(f),
$$

where $\mathbf{h}(\mathbf{x},t)$ is the current density impulse response of the antenna. The current density induces the *vector potential*

$$\vec{a}(\mathbf{x},t) = \frac{\mu_0}{4\pi}(\rho \circledast \vec{\mathbf{j}})(\mathbf{x},t) \tag{4}$$
$$= \frac{\mu_0}{4\pi}(\rho \circledast \mathbf{h} * s)(\mathbf{x},t)$$

where μ_0 is the permeability of free space and

$$\rho(\mathbf{x},t) = \frac{\delta(t - \|\mathbf{x}\|/c)}{\|\mathbf{x}\|}$$

is the Green's function for free space propagation. The vector potential represents a superposition of spherical waves centered at each point on the current density. We are specifically interested in evaluating the vector potential at an arbitrary position $\mathbf{x} = r\hat{\mathbf{u}}$ in the far field (i.e. r large). Taking the temporal Fourier transform of Eq. (4) and making the far-field approximation $\|\mathbf{x} - \mathbf{y}\| \approx r - \mathbf{y}^\mathsf{T}\hat{\mathbf{u}}$ yields

$$\mathscr{A}(r\hat{\mathbf{u}},f) \approx \frac{\mu_0}{4\pi}\frac{e^{-j2\pi rf/c}}{r}\vec{\mathbf{J}}(\hat{\mathbf{u}}f/c,f)$$
$$\approx \frac{\mu_0}{4\pi}\frac{e^{-j2\pi rf/c}}{r}\mathbf{H}(\hat{\mathbf{u}}f/c,f)S(f), \tag{5}$$

where the spatial convolution with the Green's function has yielded a spatial Fourier transform on the current density. Finally, we can relate the far-field electric field to the vector potential in both time and frequency via

$$\vec{\mathbf{e}}(r\hat{\mathbf{u}},t) \approx -\frac{\partial}{\partial t}\mathbf{\Gamma}_{\hat{\mathbf{u}}}\vec{a}(r\hat{\mathbf{u}},t)$$
$$\vec{\mathbf{E}}(r\hat{\mathbf{u}},f) \approx -j2\pi f\mathbf{\Gamma}_{\hat{\mathbf{u}}}\mathscr{A}(r\hat{\mathbf{u}},f), \tag{6}$$

where $\mathbf{\Gamma}_{\hat{\mathbf{u}}}$ is the 3×3 projection matrix into the plane normal to $\hat{\mathbf{u}}$. Substituting Eq. (5) into Eq. (6) yields

$$\vec{\mathbf{E}}(r\hat{\mathbf{u}},f) \approx -\frac{\mu_0}{4\pi}\frac{e^{-j2\pi rf/c}}{r}j2\pi f\mathbf{\Gamma}_{\hat{\mathbf{u}}}\mathbf{H}(\hat{\mathbf{u}}f/c,f)S(f)$$
$$\approx -\mu_0\frac{e^{-j2\pi rf/c}}{4\pi r}S(f)\vec{\mathbf{A}}(\hat{\mathbf{u}},f), \tag{7}$$

where the *wideband array pattern* is defined as

$$\vec{\mathbf{A}}(\hat{\mathbf{u}},f) \triangleq j2\pi f\mathbf{\Gamma}_{\hat{\mathbf{u}}}\mathbf{H}(\hat{\mathbf{u}}f/c,f). \tag{8}$$

In Eq. (7) we see that the wideband array pattern contains all of the direction dependence of the electric field, with the range-dependent phase and amplitude factored out. The apportionment of constant scale factors here is somewhat arbitrary; in practice, the array pattern is usually scaled relative to that of an ideal isotropic radiator with the same input power. Here again we see the mapping $\mathbf{v} = \hat{\mathbf{u}}f/c$ between propagation direction and spatial frequency; this is a statement of the Helmholtz equation, itself a form of the wave equation. It restricts propagating spatial frequencies to the surface $\|\mathbf{v}\| = |f|/c$, sometimes called the *visible* spatial

frequencies, or the *Helmoholtz cone*. The advantage of this spatial frequency relationship is that we can use basic Fourier properties to determine the effect of physical transformations of an antenna, such as translations and rotations, on the array pattern. These operations can then be used to construct arbitrary array geometries.

2.3.2 Receive

On receive, our input signal is now the space-time vector field $\vec{\mathbf{e}}(\mathbf{x}, t)$ at the array, while the output is the temporal signal $s(t)$ induced at the antenna feed. If we assume that our antenna is reciprocal [37], and that all received radiation originates in the far field, then we can write the output as

$$s(t) = \beta \frac{\partial}{\partial t} \int \vec{\mathbf{e}}^{\mathsf{T}}(\mathbf{x}, \tau) \mathbf{h}(\mathbf{x}, t - \tau) \, d\mathbf{x} \, d\tau = \beta \frac{\partial}{\partial t} (\vec{\mathbf{e}}' \circledast \mathbf{h})(\mathbf{0}, t) \tag{9}$$

$$S(f) = \beta \mathrm{j} 2\pi f \int \vec{\mathbf{E}}^{\mathsf{T}}(-\mathbf{v}, f) \mathbf{H}(\mathbf{v}, f) \, d\mathbf{v}, \tag{10}$$

where β represents uninteresting scale factors and $\vec{\mathbf{e}}'(\mathbf{x}, t) \triangleq \vec{\mathbf{e}}^{\mathsf{T}}(-\mathbf{x}, t)$. This can be viewed as a spatial correlation and temporal convolution between the field and the array, or equivalently as a space-time convolution sampled at the spatial origin. Reciprocity does not imply complex conjugation, so the correlation here does not either. Now let us assume that $\vec{\mathbf{e}}$ is a polychromatic plane wave with polarization vector $\boldsymbol{\Gamma}_{\hat{\mathbf{u}}} \vec{\boldsymbol{\psi}}$ traveling in the direction $-\hat{\mathbf{u}}$, where $\hat{\mathbf{u}}$ is now the *look direction* rather than the transmit direction:

$$\vec{\mathbf{e}}(\mathbf{x}, t) = \boldsymbol{\Gamma}_{\hat{\mathbf{u}}} \vec{\boldsymbol{\psi}} \varepsilon(t) e^{\mathrm{j} \frac{2\pi}{\lambda} \hat{\mathbf{u}}^{\mathsf{T}} \mathbf{x}} \longleftrightarrow \vec{\mathbf{E}}(\mathbf{v}, f) = \boldsymbol{\Gamma}_{\hat{\mathbf{u}}} \vec{\boldsymbol{\psi}} \mathcal{E}(f) \delta\left(\mathbf{v} + \frac{1}{\lambda} \hat{\mathbf{u}}\right). \tag{11}$$

Subsituting Eq. (11) into Eq. (10) yields

$$S(f) = \beta \mathrm{j} 2\pi f \mathcal{E}(f) \vec{\boldsymbol{\psi}}^{\mathsf{T}} \boldsymbol{\Gamma}_{\hat{\mathbf{u}}} \mathbf{H}(\hat{\mathbf{u}} f / c, f)$$
$$= \beta \mathcal{E}(f) \vec{\boldsymbol{\psi}}^{\mathsf{T}} \vec{\mathbf{A}}(\hat{\mathbf{u}}, f).$$

Here we see that the same antenna pattern we derived from using the element to transmit also describes the response of the element to incoming plane waves.

2.4   Element Transformations

Here we define some basic spatial transformations and their corresponding effects on the element pattern, which can be used to construct the full wideband array pattern. Let $\mathbf{h}_0 \leftrightarrow \mathbf{H}_0$ be the prototype current-density impulse response and transfer function of the untransformed element, with element pattern $\vec{\mathbf{A}}_0$. We first consider translation of the antenna (and thus its impulse response) by some offset $\mathbf{x}_1$, according to Eq. (2e):

$$\mathbf{h}_1(\mathbf{x}, t) = \mathbf{h}_0(\mathbf{x} - \mathbf{x}_1, t) \longleftrightarrow \mathbf{H}_1(\mathbf{v}, f) = \mathbf{H}_0(\mathbf{v}, f) e^{\mathrm{j} 2\pi \mathbf{v}^{\mathsf{T}} \mathbf{x}_1}$$

from which the translated antenna pattern can be computed as

$$\vec{\mathbf{A}}_1(\hat{\mathbf{u}}, f) = \vec{\mathbf{A}}_0(\hat{\mathbf{u}}, f) e^{\mathrm{j} 2\pi \frac{f}{c} \hat{\mathbf{u}}^{\mathsf{T}} \mathbf{x}_1}.$$

Thus, the effect of the translation is a linear phase term that corresponds to a direction-dependent time delay. Next we consider rotation of the antenna by some arbitrary 3×3 rotation matrix $\mathbf{R}$, affecting both the vector orientation (polarization) of the current density as well as the spatial orientation:

$$\mathbf{h}_1(\mathbf{x}, t) = \mathbf{R}\,\mathbf{h}_0(\mathbf{R}^{-1}\mathbf{x}, t) \longleftrightarrow \mathbf{H}_1(\mathbf{v}, f) = \mathbf{R}\,\mathbf{H}_0(\mathbf{R}^{-1}\mathbf{v}, f),$$

where we use Eq. (2d) and the fact that $\mathbf{R}^{-\mathsf{T}} = \mathbf{R}$ for a rotation matrix. This yields a rotated element pattern of

$$\vec{\mathbf{A}}_1(\hat{\mathbf{u}}, f) = \mathbf{R}\,\vec{\mathbf{A}}_0(\mathbf{R}^{-1}\hat{\mathbf{u}}, f).$$

If we let $\mathbf{R} = \mathbf{R}_\varphi$ be a rotation about the z-axis by some angle φ, then we can further simplify this expression in terms of the horizontal and vertical polarization components:

$$\begin{bmatrix} A_{1,\phi}(\phi, \theta, f) \\ A_{1,\theta}(\phi, \theta, f) \end{bmatrix} \triangleq \begin{bmatrix} \hat{\boldsymbol{\phi}}^{\mathsf{T}}(\phi, \theta) \\ \hat{\boldsymbol{\theta}}^{\mathsf{T}}(\phi, \theta) \end{bmatrix} \mathbf{R}_\varphi \vec{\mathbf{A}}(\mathbf{R}_\varphi^{-1}\hat{\mathbf{u}}(\phi, \theta), f)$$

$$= \begin{bmatrix} \hat{\boldsymbol{\phi}}^{\mathsf{T}}(\phi - \varphi, \theta) \\ \hat{\boldsymbol{\theta}}^{\mathsf{T}}(\phi - \varphi, \theta) \end{bmatrix} \vec{\mathbf{A}}(\hat{\mathbf{u}}(\phi - \varphi, \theta), f)$$

$$= \begin{bmatrix} A_{0,\phi}(\phi - \varphi, \theta, f) \\ A_{0,\theta}(\phi - \varphi, \theta, f) \end{bmatrix}.$$

In the second line, we rely on the construction of the local Cartesian basis, which yields the identities

$$\mathbf{R}_\varphi \hat{\mathbf{u}}(\phi, \theta) = \hat{\mathbf{u}}(\phi + \varphi, \theta)$$

$$\mathbf{R}_\varphi \hat{\boldsymbol{\phi}}(\phi, \theta) = \hat{\boldsymbol{\phi}}(\phi + \varphi, \theta)$$

$$\mathbf{R}_\varphi \hat{\boldsymbol{\theta}}(\phi, \theta) = \hat{\boldsymbol{\theta}}(\phi + \varphi, \theta),$$

and the identity $\mathbf{R}_\varphi^{\mathsf{T}} = \mathbf{R}_\varphi^{-1} = \mathbf{R}_{-\varphi}$. Thus, we can indicate rotation in azimuth of any arbitrary polarization component via translation in ϕ.

3. UNIFORM CIRCULAR ARRAYS

In this chapter, we will construct a uniform circular array and derive its wideband array pattern. Using Fourier series analysis, we then derive the *phase-mode* patterns, which are the eigenfunctions (eigenbeams) of a UCA. We then show how the phase-mode decomposition can be used for pattern synthesis using a phase-mode beamformer (a wideband Butler matrix).

3.1 UCA Geometry and Array Pattern

Our desired UCA geometry is shown in Fig. 2, consisting of N elements spaced about a circle of radius r at azimuth angles $\varphi_0, \dots, \varphi_{N-1}$ with $\varphi_n = \varphi_0 + \frac{2\pi n}{N}$. Without any significant loss of generality, we will assume that $\varphi_0 = 0$. To construct the UCA, we first define a prototype element pattern $\vec{\mathbf{A}}_{\mathrm{el}}(\phi, \theta, f)$ with its phase-center at the origin and oriented in the direction $(\phi, \theta) = (0, 0)$, and let $A_{\mathrm{el}}(\phi, \theta, f)$ be any scalar polarization component of interest as defined in Section 2.2. To generate the zeroth scalar element pattern, we shift this prototype to position $r\hat{\mathbf{u}}(0, 0)$:

$$
\begin{aligned}
A_0(\phi, \theta, f) &= A_{\mathrm{el}}(\phi, \theta, f)e^{\mathrm{j}2\pi\frac{f}{c}r\hat{\mathbf{u}}^{\mathsf{T}}(\phi, \theta)\hat{\mathbf{u}}(0,0)} \\
&= A_{\mathrm{el}}(\phi, \theta, f)e^{\mathrm{j}2\pi\frac{f}{c}r\cos(\theta)\cos(\phi)}.
\end{aligned}
\tag{12}
$$

The remaining elements are then formed by rotating this pattern in azimuth:

$$
\begin{aligned}
A_n(\phi, \theta, f) &= A_0(\phi - \varphi_n, \theta, f) \\
&= A_{\mathrm{el}}(\phi - \varphi_n, \theta, f)e^{\mathrm{j}2\pi\frac{f}{c}r\cos(\theta)\cos(\phi-\varphi_n)}.
\end{aligned}
\tag{13}
$$

To form the array pattern, we sum these element patterns after weighting them with frequency responses $\{g_n(f)\}$:

$$
\begin{aligned}
A(\phi, \theta, f) &= \sum_{n=0}^{N-1} g_n(f)A_n(\phi, \theta, f) \\
&= \sum_{n=0}^{N-1} g_n(f)A_0(\phi - \varphi_n, \theta, f).
\end{aligned}
\tag{14}
$$

Unlike for linear and planar arrays, the element pattern cannot be factored out of the array-pattern sum due to the rotation on each element. Instead, we recognize that Eq. (14) has the form of a mixed discrete-continuous circular convolution in azimuth, and turn to phase-mode analysis to gain further insight.

3.2 Phase-Mode Analysis

Because of the natural periodic structure of the circular geometry, a Fourier-series decomposition of the element pattern and drive signals is a natural operation. *Phase modes*, then, refer to the complex-exponential Fourier basis functions for the series. Such analysis dates back to at least the 1930s [4], and was originally applied to continuous circular apertures. Phase-mode theory found more widespread use in the 1950s and 60s, while being extended to circular arrays [27, 38–42]. The theory was extended to include directional array elements in [43, 44], which showed significant improvements in bandwidth of the modes by reducing cancellation from the backlobes of elements on the other side of the circle. Overviews of circular arrays and phase-mode analysis can be found in [3, 4], and the review below largely follows these sources.
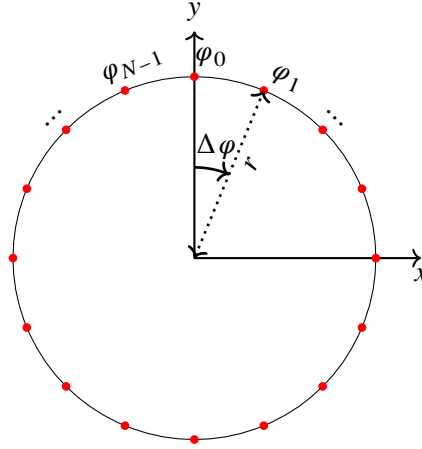
Fig. 2—The geometry of a uniform circular array in the *x*-*y* plane. *N* elements (indicated by
the red dots) are uniformly rotated about a circle of radius *r*.

3.2.1   *Phase-Mode Array Pattern*

Since the element pattern is periodic in azimuth angle ϕ, we can write it as a Fourier series:

$$A_0(\phi, \theta, f) = \sum_m a_0(m, \theta, f) e^{jm\phi}. \tag{15}$$

Here we represent coefficient index m as an argument to a_0 rather than a subscript to reinforce that it is a transform variable related to ϕ. Substituting Eq. (15) into Eq. (14) yields

$$
\begin{aligned}
A(\phi, \theta, f) &= \sum_{n=0}^{N-1} g_n(f) \sum_m a_0(m, \theta, f) e^{jm\left(\phi - \frac{2\pi n}{N}\right)} \\
&= \sum_m \left(\frac{1}{\sqrt{N}} \sum_{n=0}^{N-1} g_n(f) e^{-j\frac{2\pi mn}{N}} \right) \sqrt{N} a_0(m, \theta, f) e^{jm\phi} \\
&= \sum_m G_m(f) a_N(m, \theta, f) e^{jm\phi},
\end{aligned}
\tag{16}
$$

a Fourier series whose coeficients are the product of the the element-pattern coeficients and the periodic DFT of the element weights. Thus, we see the usual effect of the Fourier transform converting a convolution into a product. In the second line, we introduce reciprocal scale factors of $N^{\mp\frac{1}{2}}$; the first normalizes the DFT such that one period of G has the same energy as g, while the second accounts for the presence of N elements in the array via $a_N = \sqrt{N} a_0$. The factor $e^{jm\phi}$ is the mth *phase mode*, while $a_N(m, \theta, f) e^{jm\phi}$ is the corresponding phase-mode pattern of the array. Phase modes are eigenfunctions of a continuous circular aperture, much as plane waves are eigenfunctions of a continuous planar aperture, and they play a similar role in circular-array analysis as plane waves do for planar arrays. For an array of finite elements, however, we have the complication that G_m is periodic with period N, and thus we do not have full control over the terms in Eq. (16). Following [28], we can perform a coset decomposition of index m as $m = kN + l$, where $l \in [\mathbb{Z}/N\mathbb{Z}]$ is an index into the N unique values of G_m. The set of coset representatives $[\mathbb{Z}/N\mathbb{Z}]$ is not unique, but usually the sensible

choice is symmetric about 0: $\{-\underline{N}, -\underline{N}+1, \ldots, \bar{N}\}$, where $\underline{N} \triangleq \lfloor \frac{N}{2} \rfloor$ and $\bar{N} \triangleq \lceil \frac{N}{2} \rceil - 1$. Now we can rewrite the infinite sum of Eq. (16) variously as

$$
\begin{aligned}
A(\phi, \theta, f) &= \sum_{l \in [\mathbb{Z}/N\mathbb{Z}]} G_l(f) \sum_k a_N(kN + l, \theta, f) e^{j(kN+l)\phi} \\
&= \sum_{l \in [\mathbb{Z}/N\mathbb{Z}]} G_l(f) \left(a_N(l, \theta, f) + \sum_{k \neq 0} a_N(kN + l, \theta, f) e^{jkN\phi} \right) e^{jl\phi}.
\end{aligned}
\tag{17}
$$

In Eq. (17), we have a finite sum over the unique array weight coefficients, with the element-pattern contribution within parentheses split into the desired phase-mode pattern and the sum of higher-order *distortion mode* terms. These modes are so named because they lead to azimuth ripple in what would otherwise be an omnidirectional pattern. Defining the *m*th distortion mode pattern as

$$
a_{\mathrm{D}}(m, \phi, \theta, f) \triangleq \sum_{k \neq 0} a_N(kN + m, \theta, f) e^{jkN\phi},
\tag{18}
$$

we can see that the pattern is a periodic function of ϕ with a period of $2\pi/N$, as might be expected due to the geometry. We thus can simplify the full array pattern as

$$
\begin{aligned}
A(\phi, \theta, f) &= \sum_{l \in [\mathbb{Z}/N\mathbb{Z}]} G_l(f) \left(a_N(l, \theta, f) + a_{\mathrm{D}}(l, \phi, \theta, f) \right) e^{jl\phi} \\
&= A_{\mathrm{N}}(\phi, \theta, f) + A_{\mathrm{D}}(\phi, \theta, f)
\end{aligned}
\tag{19}
$$

as the sum of a desired, ideal response and residual distortion modes. Part of designing a circular array, then, is choosing an element such that the distortion mode patterns are small, or equivalently choosing N large enough to cover all of the significant phase modes for a given element. Conceptually, this is very similar to matching the element beamwidth and spacing in a planar array, albeit with different consequences for the array pattern.

We note in passing that if we choose element weights as the unit-energy complex exponential $g_n = N^{-\frac{1}{2}} e^{j\frac{m_0 n}{N}}$, then we find that their DFT is the shifted impulse train

$$
G_m = \sum_k \delta_{m - m_0 - kN}.
$$

Substituting this into Eq. (17) results in the array pattern

$$
A_{m_0}(\phi, \theta, f) = \left(a_N(m_0, \theta, f) + a_{\mathrm{D}}(m_0, \phi, \theta, f) \right) e^{jm_0\phi},
$$

which is just the m_0th phase mode pattern and associated error modes. Since the complex exponential drive weights match the columns of a standard unitary IDFT matrix, we can use the IFFT operation to efficiently compute all of the mode patterns from the vector of rotated element patterns as an alternative to directly computing the Fourier series of Eq. (15) in the case where we do not need to separate out the distortion modes.

3.2.2 Element Pattern Phase-Mode Spectrum

In the previous section, we saw that we want to properly match the number of elements N to the element phase-mode pattern in order to avoid distortion modes. In this section, we analyze the effects of the choice of the element and the array radius on the phase-mode pattern. In so doing, we will show that a circular aperture has a spatial bandwidth imposed by physics much as a planar one does. Nominally, the analysis in this section applies to a single element and is independent of the number of elements spaced around the circle. However, we are implicitly defining A_0 to be the embedded element pattern, which includes interactions with surrounding elements, and thus cannot be completely independent of N.

We start by inverting Eq. (15) to express the element phase-mode spectrum a_0 in terms of the shifted prototype element pattern:

$$a_0(m, \theta, f) = \frac{1}{2\pi} \int_0^{2\pi} A_0(\phi, \theta, f) \mathrm{e}^{-\mathrm{j}m\phi} \, \mathrm{d}\phi. \tag{20}$$

Substituting the unshifted prototype element pattern Eq. (12) into Eq. (20) yields

$$a_0(m, \theta, f) = \frac{1}{2\pi} \int_0^{2\pi} A_{\mathrm{el}}(\phi, \theta, f) \mathrm{e}^{\mathrm{j}2\pi\frac{f}{c}r\cos(\theta)\cos(\phi)} \mathrm{e}^{-\mathrm{j}m\phi} \, \mathrm{d}\phi,$$

while substituting the Fourier series for A_{el} and rearranging yields

$$a_0(m, \theta, f) = \frac{1}{2\pi} \int_0^{2\pi} \sum_k a_{\mathrm{el}}(k, \theta, f) \mathrm{e}^{\mathrm{j}k\phi} \mathrm{e}^{\mathrm{j}2\pi\frac{f}{c}r\cos(\theta)\cos(\phi)} \mathrm{e}^{-\mathrm{j}m\phi} \, \mathrm{d}\phi$$

$$= \sum_k a_{\mathrm{el}}(k, \theta, f) \frac{1}{2\pi} \int_0^{2\pi} \mathrm{e}^{\mathrm{j}(k-m)\phi} \mathrm{e}^{\mathrm{j}2\pi\frac{f}{c}r\cos(\theta)\cos(\phi)} \, \mathrm{d}\phi. \tag{21}$$

Recalling the integral expression for the Bessel function of the first kind,

$$\mathrm{J}_n(z) = \frac{1}{\mathrm{j}^n 2\pi} \int_0^{2\pi} \mathrm{e}^{\mathrm{j}n\phi} \mathrm{e}^{\mathrm{j}z\cos(\phi)} \, \mathrm{d}\phi,$$

Eq. (21) reduces to

$$a_0(m, \theta, f) = \sum_k a_{\mathrm{el}}(k, \theta, f) \mathrm{j}^{k-m} \mathrm{J}_{k-m}\left(2\pi\frac{f}{c}r\cos(\theta)\right)$$

$$= \sum_k a_{\mathrm{el}}(k, \theta, f) \mathrm{j}^{m-k} \mathrm{J}_{m-k}\left(2\pi\frac{f}{c}r\cos(\theta)\right), \tag{22}$$

with the second line a result of the symmetry relation $\mathrm{J}_{-n}(z) = (-1)^n \mathrm{J}_n(z)$. This is a discrete convolution between the Fourier series of the prototype-element and that of a continuous circular aperture under a phase-mode excitation. The properties of the phase-mode pattern thus flow from these two series. The series for typical elements is lowpass with a small number of significant coefficients; some examples are shown in [4,

Fig. 2.14]. Thus, their effect is to smooth out the Bessel response, which otherwise dominates. Figure 3 plots a_0 with $\theta = 0$ vs. phase-mode index m and the Bessel-fuction argument $2\pi rf/c$. The plot on the left shows the case of an omnidirectional element, with $a_{\mathrm{el}}(k,0,f) = \delta_k$, while the plot on the right results from an element with the azimuth pattern $A_{\mathrm{el}}(\phi,0,f) = 1 + \cos(\phi)$, which yields $a_{\mathrm{el}}(k,0,f) = 0.5\delta_{k+1} + \delta_k + 0.5\delta_{k-1}$. We can see that the phase-mode spectrum for the omnidirectional case fades in and out quickly as a function of mode, wavelength, and radius. This is due to constructive and destructive interference between elements on both sides of the circle. The phase-mode spectrum for the directional pattern is much more uniform, as the element pattern suppresses radiation from the opposite side of the array. In both cases, there is a sharp cutoff at $m = \pm 2\pi rf/c$, such that essentially no radiation occurs at higher-magnitude phase modes. This corresponds to linear spatial frequencies of $\pm f/c = \pm 1/\lambda$ around the perimeter of the array, and thus is consistent with the Helmholtz equation and the analysis of Section 2. Driving modes above this cutoff is equivalent to steering a linear or planar array past 90° into invisible space.

We can now return to the array-pattern expression of Eq. (17), and the question of choosing the number of elements in the array to match the element phase-mode pattern. We have seen that the significant values of $a_0(m,\theta,f)$ are restricted to $|m| \le 2\pi rf/c$, and thus in order to ensure that all of the distortion modes are above this limit, we should choose $N \ge 4\pi rf_{\max}/c = 4\pi r/\lambda_{\min}$, where $f_{\max}$ is the maximum frequency of operation and $\lambda_{\min}$ the corresponding minimum wavelength. This translates to an element spacing of $d \le \lambda_{\min}/2$, a thoroughly unsurprising result that parallels the usual development of grating-lobe-free linear arrays.
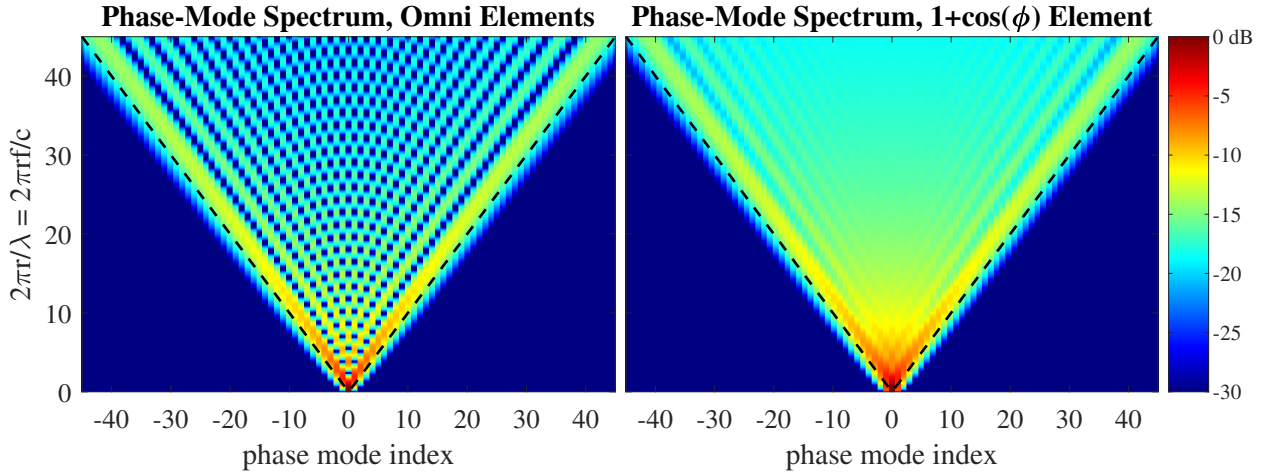
Fig. 3—The phase mode spectrum of Eq. (22) at $\theta = 0$ for two ideal elements. On the left is an isotropic element, on the right an element with a directive azimuth pattern of $1 + \cos(\phi)$. The extra nonzero coefficients of the directive pattern spectrum smooth out the phase-mode spectrum. The diagonal, dashed lines indicate $m = \pm 2\pi r/\lambda$, which is the approximate boundary between radiating and nonradiating phase modes.

3.2.3   Virtual Linear Array

One of the oft-cited advantages of phase-mode analysis is that it transforms the UCA beamforming problem into a virtual linear-array beamforming problem. Let us compare Eq. (17) (ignoring the distortion modes) with the corresponding expression for a wideband uniform linear array (ULA) with spacing d along

the x-axis:

$$A_{\text{UCA}}(\phi, \theta, f) = \sum_{m=-\underline{N}}^{\overline{N}} G_m(f) a_N(m, \theta, f) e^{jm\phi} \tag{23a}$$

$$A_{\text{ULA}}(\phi, \theta, f) = \sum_{m=-\underline{N}}^{\overline{N}} W_m(f) B_{\text{el}}(\phi, \theta, f) e^{jm\left(2\pi \frac{f}{c} d \cos(\theta) \sin(\phi)\right)}. \tag{23b}$$

Here W_m is the mth frequency-dependent linear-array weight, B_{el} is the common linear-array element pattern, and we have chosen the same indexing for both arrays (somewhat arbitrarily in the case of the linear array). Both patterns are the sum of products of complex weights, "element" patterns, and a Fourier exponential that is a function of azimuth. These parallels are often invoked to say that the phase-mode decomposition produces a virtual linear array, with the phase modes representing element-position index and the phase-mode patterns playing the role of the element pattern. With certain caveats to be discussed momentarily, this similarity allows ULA algorithms to be applied to design the UCA phase-mode weights.

There are a few important differences between Eqs. (23a) and (23b). First, the electrical angle in Eq. (23a) is simply the physical azimuth angle, while in Eq. (23b), it is a normalized spatial frequency that depends on frequency (wavelength) as well as having a nonlinear dependence on azimuth and elevation. In particular, the dependence on frequency can be a problem for wideband linear arrays, as their beamwidth will naturally narrow at higher frequencies without appropriate design of the element-weighting responses, and they require time delays to maintain the steering direction across frequency. Exploiting the relative frequency invariance of the UCA is one of the key drivers for the phase-mode beamformer considered in the next section. Both UCA and ULA have a dependence on elevation, the UCA through the index-dependent phase-mode patterns and the ULA through the complex exponent. For this reason, the correspondence between the two are usually limited to $\theta = 0$. Another difference is that the phase-mode patterns are functions of mode index m, while the linear-array element pattern can be factored out of the sum. In practice, the circular array will include equalization between the modes, although such equalization is again specific to a given elevation angle θ. We discuss this equalization more in the next section.

3.3 Phase-Mode Synthesis
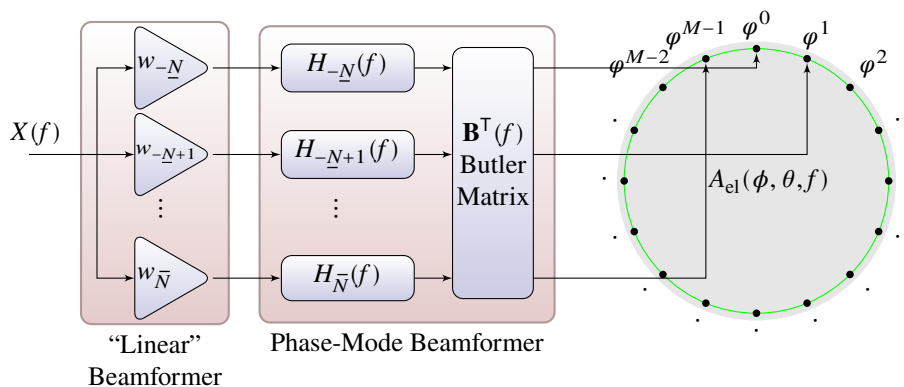
Fig. 4—Block diagram of circular array with wideband phase-mode transmit beamformer

In the preceding sections, we showed how phase modes naturally emerge from the analysis of uniform circular arrays. Phase modes are also frequently used for array synthesis [28, 39, 40, 45, 46], most commonly
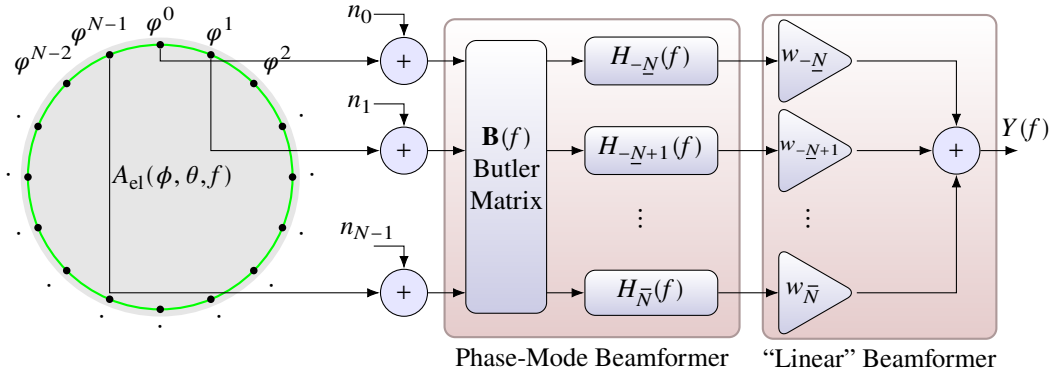
Fig. 5—Block diagram of circular array with wideband phase-mode receive beamformer. An active-array architecture is assumed with noise sources indicated at the LNA positions.

as a way to achieve a frequency-invariant pattern without requiring custom design of FIR filters as in [13]. In phase-mode synthesis, the modal weighting functions $\{G_m\}$ are designed directly, with an explicit *phase-mode beamformer* converting between modal and elemental signals. On transmit, the beamformer takes modal signals in and outputs element drive signals, as shown in Fig. 4. On receive, the beamformer accepts signals from the elements and outputs the phase modes, as shown in Fig. 5. In both cases, a "linear" beamformer is applied to the resulting virtual array to combine the phase modes and generate the pattern, and, with the exception of receiver noise sources in the RX model, the two models are reciprocal. The phase-mode beamformer itself consists of a $N \times N$ transformation matrix $\mathbf{B}(f)$, and a set of N equalization filters $\{h_m(f)\}$ that correct for differences between the phase-mode patterns $\{a_N(m, \theta, f)\}$ at some reference value of $\theta = \theta_0$. The matrix transformation can be implemented in either digital [45, 46] (as a DFT) or analog [27, 41] (Butler matrix) forms, although [46] found that a digital implementation of a modal beamformer was more computationally complex than a conventional beamformer. Here we are primarily interested in the implementation of an analog beamformer, with its digital counterpart used as an ideal reference. The equalization filters can likewise be implemented as either digital finite-impulse-response (FIR) filters or analog tapped-delay-line (TDL) filters, and we will consider both cases.

Now let us derive the array pattern in terms of the structures in Figs. 4 and 5. We start by rewriting Eq. (23a) using vector notation as

$$
\begin{aligned}
A(\phi, \theta, f) &= \mathbf{G}^{\mathsf{T}}(f)\mathbf{a}(\phi, \theta, f) \\
&= \mathbf{g}^{\mathsf{T}}(f)\mathbf{D}\mathbf{a}(\phi, \theta, f),
\end{aligned}
\tag{24}
$$

where $\mathbf{a}$ is the vector of phase-mode patterns

$$
[\mathbf{a}(\phi, \theta, f)]_k = (a_N(m_k, \theta, f) + a_D(m_k, \phi, \theta, f))\mathrm{e}^{\mathrm{j}m_k\phi},
\tag{25}
$$

where m_k is the mode of the kth Butler-matrix port, $\mathbf{G}(f)$ is the vector of phase-mode weighting functions, and $\mathbf{g}(f)$ is the vector of element weighting functions. The vectors $\mathbf{g}$ and $\mathbf{G} = \mathbf{D}\mathbf{g}$ are related through unitary DFT matrix $\mathbf{D}$, with $D_{m,n} = N^{-\frac{1}{2}}\mathrm{e}^{-\mathrm{j}2\pi\frac{mn}{N}}$. It will be convenient to continue indexing the elements as $n = 0, \ldots, N - 1$ and the fundamental phase modes as $m = -\underline{N}, \ldots, \bar{N}$; as these both form a complete

set of coset representatives $[\mathbb{Z}/N\mathbb{Z}]$, this simply represents a permutation of the rows of D relative to the "traditional" DFT matrix. Now we substitute the equivalent element-response vector from Figs. 4 and 5,

$$\mathbf{g}(f) = \mathbf{B}^{\mathsf{T}}(f) \, \text{diag}\{\mathbf{H}(f)\}\mathbf{w},$$

into Eq. (24), which yields

$$A(\phi, \theta, f) = \mathbf{w}^{\mathsf{T}}\text{diag}\{\mathbf{H}(f)\}\mathbf{B}(f)\mathbf{Da}(\phi, \theta, f). \tag{26}$$

In an ideal world, with no nonzero distortion modes, we would design $\mathbf{B} = \mathbf{D}^{-1}$ and $h_m(f) = a_N^{-1}(m, \theta_0, f)$, such that Eq. (26) reduces to

$$
\begin{aligned}
A(\phi, \theta, f) &= \sum_m w_m \frac{a_N(m, \theta, f)}{a_N(m, \theta_0, f)} e^{\mathrm{j}m\phi} \\
&\triangleq \mathbf{w}^{\mathsf{T}}\mathbf{a}_{\text{EQ}}(\phi, \theta, f)
\end{aligned} \tag{27}
$$

and

$$A(\phi, \theta_0, f) = \sum_m w_m e^{\mathrm{j}m\phi}, \tag{28}$$

the virtual linear array of Eq. (23a) with the phase modes perfectly equalized at $\theta = \theta_0$. Real hardware is never ideal, of course, and so we consider in the next section how to model the sources of error in the array pattern.

3.4   Error Analysis

In this section, we consider the various sources of error that can occur in hardware implementations of the circular-array architectures of Figs. 4 and 5, and show which can be compensated by the equalization filters. We assume here that the equalization filters are designed offline and fixed during operation, rather than being customized for each array pattern. Although recomputing them for each beam would improve performance, it would also largely defeat the purpose of using the phase-mode beamformer in the first place, which is the simplicity of using scalar weights at each mode to effect wideband frequency-invariant patterns.

There are three primary sources of error to be considered. The first is the distortion modes in the array itself, which have already been discussed in the phase-mode derivation. The second is errors in the Butler matrix, which both distorts individual modes and cross-contaminates the modes, causing further "distortion modes" even with a distortion-free array. The final errors are in the equalization filters, which are tasked with compensating the mode-specific frequency responses. Here we have both hardware errors (in an analog TDL implementation) as well as Fourier approximation errors, which result from using a finite impulse response (FIR or TDL) implementation.

3.4.1 Distortion Modes

Distortion modes, as derived in Section 3.2.1, are higher-order circular modes that cause ripple in azimuth with a period of $2\pi/N$. Expanding $\mathbf{a} = \mathbf{a}_N + \mathbf{a}_D$ into fundamental and distortion mode vectors in Eq. (26) yields

$$A(\phi, \theta, f) = \mathbf{w}^\mathsf{T}\text{diag}\{\mathbf{H}(f)\}\mathbf{B}(f)\mathbf{D}(\mathbf{a}_N(\phi, \theta, f) + \mathbf{a}_D(\phi, \theta, f)).$$

The distortion modes are orthogonal to their respective fundamental mode, and cause unwanted amplitude and phase ripple across azimuth. They do not usefully contribute to the desired pattern and generally represent a pure error response.

3.4.2 Butler Matrix Errors

When implemented digitally, a DFT or IDFT can be computed to any precision desired and the error is negligible for the present purposes. The primary drawback of a digital implementation is the high computational burden for wideband operation, as it needs to be computed for each time sample. An analog Butler matrix offers a tremendous amount of parallel processing; however, there are inevitable errors due to component and fabrication tolerances which (unlike the DFT) can vary in frequency. Here we will model the frequency response of the Butler matrix as

$$\mathbf{B}(f) = \mathbf{\Sigma}(f)(\mathbf{I} + \mathbf{E}^\mathsf{T}(f))\mathbf{D}^{-1} \tag{29}$$

such that

$$\mathbf{B}(f)\mathbf{D} = \mathbf{\Sigma}(f)(\mathbf{I} + \mathbf{E}(f)),$$

where $\mathbf{\Sigma}$ is a diagonal matrix frequency response and $\mathbf{E}$ has zeros down the central diagonal. The first factor represents the frequency-varying distortion applied by the Butler matrix to each mode; this response can be compensated by the following equalization filtering. The second factor, $\mathbf{E}$, represents cross terms which couple one mode into another. Like the distortion modes, this results in responses that have ripple across azimuth, but with no particular periodicity. Expanding Eq. (26) with this error model yields

$$A(\phi, \theta, f) = \mathbf{w}^\mathsf{T}\text{diag}\{\mathbf{H}(f)\}\mathbf{\Sigma}(f)\Big(\mathbf{a}_N(\phi, \theta, f) + \mathbf{a}_D(\phi, \theta, f) + \mathbf{E}(f)\mathbf{a}(\phi, \theta, f)\Big). \tag{30}$$

Here, in the parenthesis on the right, we have the desired fundamental mode term, the distortion mode term, and the Butler-matrix error term which potentially depends on all of the modes generated by the array. Expanding the error terms using Eqs. (25) and (17) yields

$$[\mathbf{a}_D(\phi, \theta, f)]_k = \sum_{n \neq 0} a_N(nN + m_k, \theta, f)e^{j(nN + m_k)\phi} \tag{31}$$

$$[\mathbf{E}(f)\mathbf{a}(\phi, \theta, f)]_k = \sum_{l \neq k} E_{k,l}(f) \sum_n a_N(nN + m_l, \theta, f)e^{j(nN + m_l)\phi} \tag{32}$$

for the distortion mode and Butler-matrix error terms, respectively. Both Eqs. (31) and (32) have the form of a Fourier series, and by construction have no series terms in common. This suggests an alternative way to derive these errors, considered next.

3.4.3   Combined Beamformer/Array Errors

Considering the errors due to distortion modes or Butler-matrix errors separately is valuable, as it allows the designer to modularize the design process and improve each component in isolation. In many cases it will also be convenient to consider the cascade of the Butler matrix and the circular array as a single unit. When modeling or building physical hardware, the cascade response does not depend only on the frequency responses of the components, but also on reflections due to impedance mismatch at the connection points. So simulating or measuring the cascade is generally going to be more accurate than measuring each independently. In addition, the errors generated by each stage are similar in their effects on the array pattern, and the combined error is ultimately the metric of interest. Finally, considering the cascade as simply a phase-mode driven array simplifies the analysis, as the underlying element pattern can be largely ignored in favor of the patterns produced by each Butler-matrix input (on TX) or output (RX).

For notational convenience, define the vector of Butler matrix-induced array patterns

$$\mathbf{A}_B(\phi,\theta,f) \triangleq \mathbf{B}(f)\mathbf{D}\mathbf{a}(\phi,\theta,f)$$

such that substituting into Eq. (26) yields

$$A(\phi,\theta,f) = \mathbf{w}^\mathsf{T}\mathrm{diag}\{\mathbf{H}(f)\}\mathbf{A}_B(\phi,\theta,f).$$

As we did before with the element pattern, we can write $\mathbf{A}_B$ as a Fourier series in the azimuth variable:

$$\mathbf{A}_B(\phi,\theta,f) = \sum_m \mathbf{a}_B(m,\theta,f)e^{jm\phi}. \qquad (33)$$

With an array with no distortion modes and an ideal Butler matrix, each vector entry k would have only one nonzero Fourier series coefficient, corresponding to the mode index m_k of that Butler-matrix port:

$$[\mathbf{a}_B^{\mathrm{ideal}}(m,\theta,f)]_k = 0, \quad m \neq m_k.$$

However, due to inevitable distortion modes in the array and nonideal behavior in the Butler matrix, there will be nonzero series coefficients for many indices around the desired one. We can again compute the Fourier series coefficients (modes) contained within each pattern via

$$\mathbf{a}_B(m,\theta,f) = \frac{1}{2\pi}\int_0^{2\pi} \mathbf{A}_B(\phi,\theta,f)e^{-jm\phi}\,\mathrm{d}\phi.$$

The relative size of the mode coefficients for $m \neq m_k$ then provides a metric for the total error contained in the Butler matrix patterns. These series terms map one-to-one to those of Eqs. (31) and (32); comparing with Eq. (30) yields

$$[\mathbf{a}_B(m,\theta,f)]_k = \begin{cases} \sigma_k(f)a_N(m,\theta,f), & m = m_k \pmod{N} \\ \sigma_k(f)E_{k,l}(f)a_N(m,\theta,f), & m \neq m_k \pmod{N} \end{cases}$$

where $m_l = m \pmod{N}$ and σ_k is the kth diagonal element of $\boldsymbol{\Sigma}$. As such, this is merely a restatement of the separate error analysis of the array and Butler matrix.

3.4.4 Equalization Errors

Like the Butler matrix, the equalization filters can be implemented either digitally in the form of FIR filters or in analog in the form of tapped-delay-line (TDL) filters. Digital implementations allow for high precision, but again need to be computed at every time sample and thus require a great amount of computation for wide bandwidths. Analog TDL filters again have the advantage of high inherent parallelism at the cost of less precision. Both implementations have approximation errors due to their finite temporal support, but analog filters have further errors due to quantization of the magnitude and phase and due to imperfections in the attenuators and phase shifters.

The frequency response of a digital FIR filter has the form of a discrete-time Fourier transform:

$$H(f) = \sum_{n=0}^{N_h-1} h_n e^{-\mathrm{j}2\pi nfT_s} \tag{34}$$

where $\{h_0, \dots, h_{N_h-1}\}$ are the complex weights at sample delays $\{0, T_s, \dots, (N_h - 1)T_s\}$ and T_s is the sample interval. The frequency response is periodic with period $f_s = 1/T_s$, and thus provides design control at most over one period. An ideal analog TDL filter with the structure shown in Fig. 6 has a similar frequency response:

$$H(f) = \sum_{n=0}^{N_h-1} \xi_n e^{\mathrm{j}\vartheta_n} e^{-\mathrm{j}2\pi nf\tau},$$

where $\{\xi_0, \dots, \xi_{N_h-1}\}$ are the amplitude weights, $\{\vartheta_0, \dots, \vartheta_{N_h-1}\}$ are the phase weights, and τ is the delay-line spacing. Here again, the frequency response is periodic with period $1/\tau$, but τ is independent of any subsequent sampling rate. In actual hardware, the attenuators, the phase-shifters, and the delay line and combiner all can have complex frequency responses of their own:

$$H(f) = \sum_{n=0}^{N_h-1} A_n(f)\Theta_n(f)\mathcal{T}_n(f),$$

where A_n, Θ_n, and $\mathcal{T}_n$ are the corresponding responses for the nth delay channel.

The goal of equalization is to make the modal patterns weighted by vector $\mathbf{w}$ in Eq. (30) match some reference frequency response $R(f)$; thus, for the kth mode, we can define the error as

$$\mathcal{E}_k(f) = \frac{H_k(f)\sigma_k(f)a_N(m_k, \theta_0, f) - R(f)}{R(f)} = \frac{H_k(f)\sigma_k(f)a_N(m_k, \theta_0, f)}{R(f)} - 1, \tag{35}$$

the difference between the cascade of the EQ filter with the Butler matrix and array responses and the reference, normalized by the reference. (Often the reference is chosen as a pure delay.) For notational convenience, we can define the diagonal matrix of equalization errors as

$$\mathscr{E}(f) = \frac{\mathrm{diag}\{\mathbf{H}\}\mathbf{\Sigma}(f)\,\mathrm{diag}\{\mathbf{a}_0(f)\}}{R(f)} - \mathbf{I}, \tag{36}$$

where $[\mathbf{a}_0(f)]_k = a_N(m_k, \theta_0, f)$. Substituting Eq. (35) into Eq. (30), recalling the definition of $\mathbf{a}_{\mathrm{EQ}}$ from Eq. (27) and rearranging provides the overall error model for the equalized system:

$$A(\phi, \theta, f) = \mathbf{w}^\mathsf{T} \big\{ R(f)\mathbf{a}_{\mathrm{EQ}}(\phi, \theta, f) + R(f)\boldsymbol{\mathscr{E}}(f)\mathbf{a}_{\mathrm{EQ}}(\phi, \theta, f) + \mathrm{diag}\{\mathbf{H}(f)\}\boldsymbol{\Sigma}(f)\big(\mathbf{a}_{\mathrm{D}}(\phi, \theta, f) + \mathbf{E}(f)\mathbf{a}(\phi, \theta, f)\big)\big\}$$
$$= R(f)\mathbf{w}^\mathsf{T}\big\{\mathbf{a}_{\mathrm{EQ}}(\phi, \theta, f) + \boldsymbol{\mathscr{E}}(f)\mathbf{a}_{\mathrm{EQ}}(\phi, \theta, f) + (1 + \boldsymbol{\mathscr{E}}(f))\big(\hat{\mathbf{a}}_{\mathrm{D}}(\phi, \theta, f) + \hat{\mathbf{E}}(f)\mathbf{a}(\phi, \theta, f)\big)\big\}.$$

(37)

The first term in the braces is the desired virtual linear array response, the second models errors due to imperfect equalization, and the remainder models antenna (distortion-mode) and Butler-matrix errors. (As written, this final term also incorporates second-order combinations of the equalization error with the antenna and Butler-matrix errors, but these will usually be negligible.) If the equalization is done digitally with sufficient degrees of freedom, then the EQ errors can be made arbitrarily small as the EQ responses approach the ideal response:

$$H_{k,\mathrm{ideal}}(f) = \frac{R(f)}{\sigma_k(f)a_N(m_k, \theta_0, f)}.$$

(38)

Substituting this into Eq. (37) yields

$$A(\phi, \theta, f) = R(f)\mathbf{w}^\mathsf{T}\big(\mathbf{a}_{\mathrm{EQ}}(\phi, \theta, f) + \hat{\mathbf{a}}_{\mathrm{D}}(\phi, \theta, f) + \hat{\mathbf{E}}(f)\mathbf{a}(\phi, \theta, f)\big)$$

(39)

where

$$[\hat{\mathbf{a}}_{\mathrm{D}}(\phi, \theta, f)]_k = \frac{[\mathbf{a}_{\mathrm{D}}(\phi, \theta, f)]_k}{a_N(m_k, \theta_0, f)}$$
$$[\hat{\mathbf{E}}(f)]_{k,n} = \frac{[\mathbf{E}(f)]_{k,n}}{a_N(m_k, \theta_0, f)}$$

are the normalized distortion mode pattern and normalized Butler-matrix errors, respectively. We can use Eq. (39) as a simplified, normalized error model to examine the error contributions due to the array and Butler matrix assuming ideal equalization, and then expand to Eq. (37) when considering nonideal EQ.

3.5   Noise Response and Power Gain

Having derived the array pattern and its corresponding error model for the modal beamformer, it remains to determine the response to receiver noise. We assume in Fig. 5 that the array has an LNA at each element output that is the dominant source of noise in the system. The noise component of the output is thus

$$Y_n(f) = \mathbf{w}^\mathsf{T}\,\mathrm{diag}\{\mathbf{H}(f)\}\mathbf{B}(f)\mathbf{n}(f)$$

or, substituting Eqs. (29) and (36),

$$Y_n(f) = R(f)\mathbf{w}^\mathsf{T}\,\mathrm{diag}\{\mathbf{a}_0(f)\}^{-1}(\mathbf{I} + \boldsymbol{\mathscr{E}})(\mathbf{I} + \mathbf{E}(f))\mathbf{D}^{-1}\mathbf{n}(f),$$
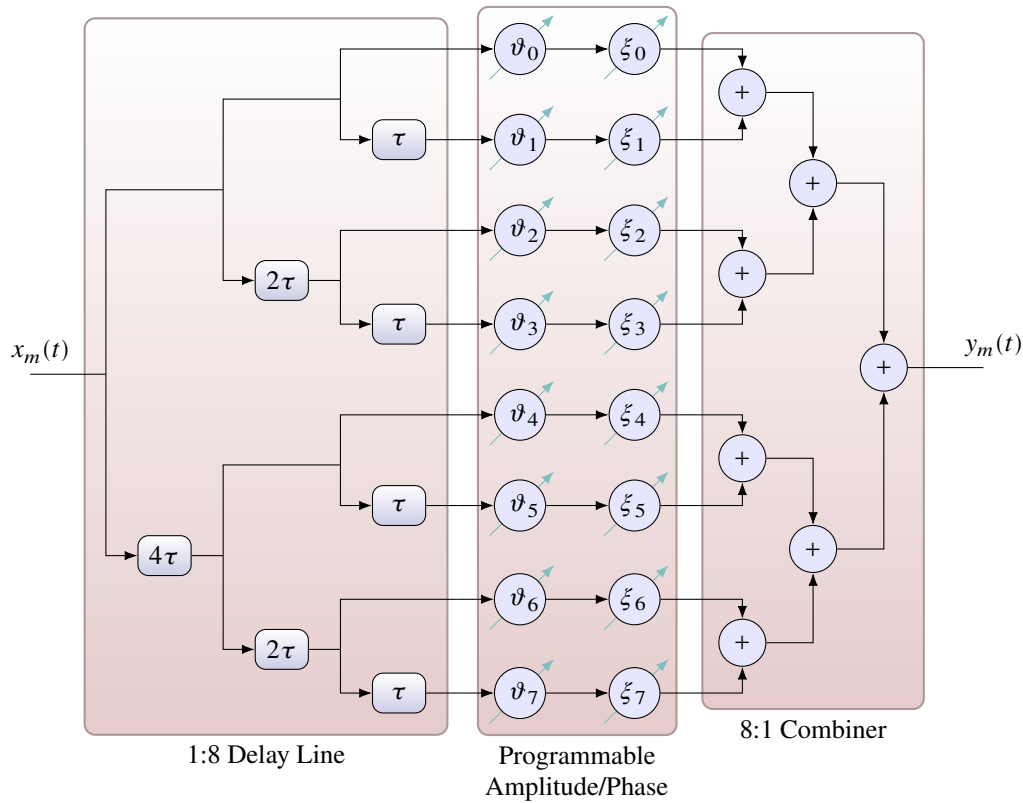
Fig. 6—Block diagram of TDL filter implementation using programmable attenuators and phase shifters

where $\mathbf{n}$ is the vector of element noise sources. We will assume the noise is wide-sense stationary,[4] with power spectral density

$$\mathbf{S_n}(f) = N_0\mathbf{I}$$

indicating that the noise components are all white and uncorrelated with each other. The corresponding spectral density of the noise at the output is then

$$S_{Y_n}(f) = N_0\big\|\mathbf{B}^\mathsf{T}(f)\,\mathrm{diag}\{\mathbf{H}(f)\}\mathbf{w}\big\|^2,$$

or, substituting in the error models of the Butler matrix and equalizer,

$$S_{Y_n}(f) = N_0|R(f)|^2\big\|(\mathbf{I} + \mathbf{E}^\mathsf{T}(f))(\mathbf{I} + \mathscr{E}(f))\,\mathrm{diag}\{\mathbf{a}_0(f)\}^{-1}\mathbf{w}\big\|^2.$$

---

[4]This assumption conflicts with the representation of the noise as the Fourier transform $\mathbf{n}(f)$, which, in this case, would not exist in the usual sense. This notational abuse serves as a shortcut to derive the effective noise transfer function without first invoking the time-domain equivalent.

If we assume that the Butler matrix and equalization errors will be small, then we can reduce this to the approximate spectral density

$$S_{Y_n}(f) \approx N_0 |R(f)|^2 \|\mathrm{diag}\{\mathbf{a}_0(f)\}^{-1}\mathbf{w}\|^2$$
$$= N_0 |R(f)|^2 \sum_k \left| \frac{w_k}{a_N(m_k, \theta_0, f)} \right|^2.$$

Here we see that neither the individual terms nor the combined noise will necessarily be white, but instead will be determined by the array phase-mode frequency responses.

In a narrowband receive array, if the element patterns are given as complex gain with respect to an isotropic radiator, then the gain for the full array is obtained by scaling the pattern such that the overall noise gain is unity. (That is, the beamformer output noise power is equal to that at each element.) For a wideband array, we can perform the same normalization pointwise to ensure that the output noise density at each frequency is the same as at the input. We can thus define the narrowband power/SNR gain of the array as

$$G_{\mathrm{nb}}(\phi, \theta, f) = \frac{|A(\phi, \theta, f)|^2}{\frac{1}{N_0} S_{Y_n}(f)}. \tag{40}$$

If the various sources of error are small, then the narrowband gain simplifies to

$$G_{\mathrm{nb}}(\phi, \theta, f) \approx \frac{\left| \mathbf{w}^\mathsf{T} \mathbf{a}_{\mathrm{EQ}}(\phi, \theta, f)]\right|^2}{\left\| \mathrm{diag}\{\mathbf{a}_0(f)\}^{-1}\mathbf{w} \right\|^2}.$$

In particular, the gain is independent of N_0, the overall scaling of the array weights $\mathbf{w}$, and the choice of equalization reference $R(f)$, and depends only on the weights and the modal patterns of the array. This follows from the assumption that the receiver noise is dominated by the LNA at each element, and thus the gain depends on scaling before the LNA (modal pattern) and how the channels are combined (the weights). The Butler matrix and EQ filters can affect the frequency response applied to received signals after the LNAs, but this can always be compensated without SNR penalty and thus does not affect gain. Because of the favorable properties of the narrowband gain in showing how the array behaves across frequency, we will plot all of our array patterns in terms of gain, and indicate this by using units of dBi to indicate gain with respect to isotropic.

Narrowband gain shows how well a wideband array works at each frequency, but it distorts the frequency response of the array pattern. For wideband operation, one might also be interested in a measure of SNR improvement without this distortion. While there are various application-specific ways to approach this (such as incorporating a specific waveform), the most straightforward way is to normalize the pattern such that the total noise power within a specified band is the same at the output as at the input:

$$G_{\mathrm{wb}}(\phi, \theta, f) = \frac{|A(\phi, \theta, f)|^2}{\frac{1}{N_0(f_2 - f_1)} \int_{f_1}^{f_2} S_{Y_n}(f)\, \mathrm{d}f} \approx \frac{|R(f)|^2 \left| \mathbf{w}^\mathsf{T} \mathbf{a}_{\mathrm{EQ}}(\phi, \theta, f)] \right|^2}{\frac{1}{f_2 - f_1} \int_{f_1}^{f_2} |R(f)|^2 \left\| \mathrm{diag}\{\mathbf{a}_0(f)\}^{-1}\mathbf{w} \right\|^2 \mathrm{d}f}. \tag{41}$$

This represents the receive-side equivalent of the wideband transmit gain defined in [13]. Wideband gain is no longer independent of $R(f)$, which represents the effective frequency response of the array in the mainbeam direction and could incorporate actual system filter responses such as pulse compression. Effectively, wideband gain is just narrowband gain with the actual noise replaced by the average noise over the band, and thus the difference between the two is minimal when the noise density is not strongly frequency dependent. We will generally normalize our plots to show narrowband gain, as this conveys more general information about how the array behaves across frequency.

4.   EQUALIZATION FILTER DESIGN

The derivation of the error model for the phase-mode beamforming system in the previous section revealed that the mode equalization filters are key to the frequency-invariant performance of the system. In this section, we will develop an optimization-based approach to designing the equalization filters. Various implementations are possible, depending on where in the system the signal is digitized. We will first consider the design of digital FIR filters, for architectures that sample prior to the EQ filters. We will then consider the design of analog tapped-delay-line (TDL) filters, gradually incorporating increasing levels of hardware modeling such as quantization and nonideal amplitude and phase weights.

To perform the various optimizations, we will use second-order cone programming (SOCP) [47], a structured form of convex optimization that optimizes a linear objective subject to linear and convex-quadratic constraints. SOCP has long been used for the design of FIR filters and antenna patterns [29, 48, 49] and has numerous solvers available [50–53]. Various higher-level tools also exist to help formulate SOCP (and other) problems in a more natural way [54–56]. One of these, the "Opt" toolbox [54], is developed in-house at NRL by the author and will be used for the designs in this report.

4.1   FIR Optimization

The simplest structure for equalization of those looked at here is a digital FIR filter, since the delays are ideal and the coefficients can be made arbitrarily precise. We assume the structure of Eq. (34) for each mode to be equalized, where the complex sample rate $f_s = 1/T_s$ is assumed to be greater than the EQ bandwidth. We can design each filter independently by solving the following SOCP:

$$\underset{\mathbf{h}_k, \delta}{\text{minimize}} \quad \delta \geq 0 \tag{42a}$$

$$\text{subject to} \quad \frac{1}{f_2 - f_1} \int_{f_1}^{f_2} \left| \frac{H_k(f)\sigma_k(f)a_N(m_k, \theta_0, f)}{R(f)} - 1 \right|^2 df \leq \delta^2 \tag{42b}$$

$$\|\mathbf{h}_k\|^2 \leq e_{\max}. \tag{42c}$$

The vector of optimization variables $\mathbf{h}_k$ is just the complex weights of the kth FIR filter, while δ is an auxiliary variable which provides the required linear objective in Eq. (42a). The constraint in Eq. (42b) combined with the objective then effectively minimizes the mean-square equalization error of Eq. (35) for frequencies between f_1 and f_2. Constraint Eq. (42c) limits the total energy of the filter weights, which is equivalent to constraining the white-noise gain of the filter. This provides regularization to prevent the filter from taking on extreme values outside of the interval $f \in [f_1, f_2]$. The value of $e_{\max}$ is set empirically to limit large peaks without significantly reducing equalization performance.

4.2   TDL Optimization

Optimizing an ideal TDL equalizer filter would look identical to Eq. (42), with a final step of extracting the attenuation and phase from the complex weight vector $\mathbf{h}_k$. In practice, however, the delay network and the combining network have nonideal responses that can be at least partly compensated by including them in the optimization. We can write the TDL response as a more general sum of weighted frequency responses

$$H(f) = \sum_{n=0}^{N_h - 1} h_n \mathcal{T}_n(f) \tag{43}$$

and then optimize per Eq. (42). Any nonideal frequency response common to all delay legs can also be factored out and included in the reference response $R(f)$, which can improve equalization performance when R is difficult to approximate. While R does not affect the beamforming sum, it does affect the spectrum of the transmitted or received signals and thus may need to be corrected separately.

4.3   Managing Quantization

For FIR filters, we will generally assume that any quantization effects are minimal and that we can simply round the ideal filter weights to the nearest valid values without any significant error. This assumption is not going to be true in general for an analog TDL; the phase shifters might have as few as 4 bits of precision (16 phase values around the circle), while the attenuators have a fixed dynamic range. Unfortunately, directly optimizing weights that are restricted to discrete values requires combinatorial optimization, which is generally impractical due to the vast number of combinations of amplitude and phase settings across the filter. We can, however, perform a limited exploration of weight values that are "close" to those which result from solving Eq. (42) and then rounding. While such a procedure cannot guarantee global optimality, in many cases it can provide increased performance over rounding alone.

We begin by solving Eq. (42) for continuous-valued complex solutions $\mathbf{h}_k$, which are then decomposed into magnitude and phase vectors $\boldsymbol{\xi}_k$ and $\boldsymbol{\vartheta}_k$ such that $h_{k,n} = \xi_{k,n}e^{j\vartheta_{k,n}}$. We will assume that the magnitudes available from the variable attenuator are bounded as $\xi_{\min} \leq \xi_k \leq 1$, and we need to ensure that our design's dynamic range matches this as closely as possible. To this end, define

$$\alpha = \max\{\|\boldsymbol{\xi}_k\|_\infty\}, \quad k = 1, \ldots, K$$

as the largest optimized coefficient magnitude. Now define the elements of the vectors $\underline{\boldsymbol{\vartheta}}_k$ and $\overline{\boldsymbol{\vartheta}}_k$ as the closest two quantized phase values to the ideal values, such that $\underline{\vartheta}_{k,n} \leq \vartheta_{k,n} \leq \overline{\vartheta}_{k,n} \pmod{2\pi}$. Since there are two values per each of N_h phase values, there are 2^{N_h} permutations total, which we can enumerate as the set of vectors $\{\hat{\boldsymbol{\vartheta}}_{k,i}\}$ for $i = 1, \ldots, 2^{N_h}$. For a reasonable value of N_h, it is feasible to evaluate each of these. Now that the phases have been quantized, we reoptimize just the attenuation values for each permutation:

$$\underset{\xi_k, \delta}{\text{minimize}} \quad \delta \geq 0 \tag{44a}$$

$$\text{subject to} \quad \frac{1}{f_2 - f_1} \int_{f_1}^{f_2} \left| \frac{\alpha H_{k,i}(f)\sigma_k(f)a_N(m_k, \theta_0, f)}{R(f)} - 1 \right|^2 df \leq \delta^2 \tag{44b}$$

$$\|\boldsymbol{\xi}_k\|^2 \leq e_{\max} \tag{44c}$$

$$\xi_{\min} \leq \xi_{k,n} \leq 1, \quad n = 1, \ldots, N_h, \tag{44d}$$

where now

$$H_{k,i}(f) = \sum_{n=0}^{N_h - 1} \xi_{k,n}e^{\hat{\vartheta}_{k,i,n}}\mathcal{T}_{k,n}(f)$$

is the TDL response for the kth mode and ith permutation of quantized phases. The scaling in Eq. (44b) combined with the augmented set of linear constraints Eq. (44d) ensures that the dynamic range of the attenuators is not exceeded. The resulting amplitude solutions can then be quantized and the solution with the

smallest residual error (optimal value of δ^2) is selected. Typically variable attenuators have finer resolution than phase shifters, and thus traditional rounding usually suffices for the amplitude quantization. It is straightforward to extend this procedure by including the third, fourth, etc., nearest phase values, at the cost of increasing the number of test designs to 3^{N_h}, 4^{N_h}, etc.

4.4   Incorporating Attenuator and Phase-Shifter Responses

Up to this point, the responses of the variable attenuator and phase-shifters have been considered ideal apart from quantization. In practice they are not, of course, and unlike the delay line and combiner responses, which are fixed, their frequency responses vary with their respective settings. This poses a challenge for incorporating these responses into a continuous optimization, because in general, these components exhibit nonideal responses that are not linearly related to the attenuation and phase settings. Indeed, there may be no simple relationship between the attenuation/phase settings and the frequency response errors, but rather just a table lookup. This means that incorporating the parameterized responses directly into the optimization would require combinatorial optimization, which is generally impractical for the same reason as optimizing the quantization of otherwise ideal components.

In this section, we outline an approach to incorporating discrete attenuator and phase-shifter responses into the optization of TDL equalizer filters that relies primarily on the assumption that the nonideal component responses can be locally modelled as linear in the nominal TDL weight value. To make this more concrete, let us enumerate the set of valid attenuation values as $\{\xi_1, \ldots, \xi_{N_{att}}\}$ and the set of valid phase-shift values as $\{\vartheta_1, \ldots, \vartheta_{N_{ph}}\}$, where N_{att} and N_{ph} are the number of discrete attenuation and phase-shift values, respectively. For each attenuation value ξ_i there is an associated frequency response $\Xi_i(f)$ and for each phase-shift value ϑ_i there is an associated frequency response $\Theta_i(f)$. We will assume here that all physical instances of the attenuator and phase shifter are identical, although this condition is easily relaxed as long as the responses for all instances are known. Now let us define the normalized frequency responses

$$\hat{\Xi}_i(f) \triangleq \frac{\Xi_i(f)}{\xi_i}$$

$$\hat{\Theta}_i(f) \triangleq \frac{\Theta_i(f)}{e^{j\vartheta_i}}$$

such that $\Xi_i(f) = \xi_i \hat{\Xi}_i(f)$ and $\Theta_i(f) = e^{j\vartheta_i}\hat{\Theta}_i(f)$ can be viewed as local linear models for the individual components. Cascading both responses yields a model that is linear in the nominal complex coefficient represented by the cascade of the phase and amplitude:

$$\Xi_i(f)\Theta_j(f) = \xi_i e^{j\vartheta_j} \hat{\Xi}_i(f)\hat{\Theta}_j(f)$$
$$\triangleq c_{i,j}\hat{\Xi}_i(f)\hat{\Theta}_j(f).$$

These are merely definitions that are perfectly valid for any components, but here we will further assume that the normalized frequency responses change slowly as a function of index (or, equivalently, the values represented by the indices):

$$\hat{\Xi}_i(f) \approx \hat{\Xi}_{i'}(f), \quad |\xi_i - \xi_{i'}| \text{ "small"}$$
$$\hat{\Theta}_i(f) \approx \hat{\Theta}_{i'}(f), \quad |e^{j\vartheta_i} - e^{j\vartheta_{i'}}| \text{ "small".}$$

This then lets us define a frequency response that is linear in either a continuous amplitude ξ or a continuous complex weight c in the neighborhood of a previous quantized solution, in order to use continuous optimization to refine the solution rather than resort to brute-force searching. A four-step algorithm to exploit this structure is outlined below.

Step 1

The first step is to solve for the continuous-valued complex TDL weight vectors $\mathbf{h}_k$:

$$\underset{\mathbf{h}_k,\delta}{\text{minimize}} \quad \delta \geq 0 \tag{45a}$$

$$\text{subject to} \quad \frac{1}{f_2-f_1} \int_{f_1}^{f_2} \left| \frac{H_k(f)\sigma_k(f)a_N(m_k,\theta_0,f)}{R(f)} - 1 \right|^2 df \leq \delta^2 \tag{45b}$$

$$\|\mathbf{h}_k\|^2 \leq e_{\max}, \tag{45c}$$

where

$$H_k(f) = \sum_{n=0}^{N_h-1} h_{k,n}\hat{\Xi}_1(f)\hat{\Theta}_1(f)\mathcal{T}_{k,n}(f)$$

is the linearized and continuously extended estimate of the TDL filter frequency response centered (somewhat arbitrarily) at the first attenuation and phase index. We will assume these represent the minimum attenuation setting $\xi_1 = 1$ and zero phase shift $\vartheta_1 = e^{j0} = 1$.

Step 2

The solution from Step 1 needs to be scaled so that the amplitudes fall within the variable attenuator's range without clipping. To ensure none of the EQ filters clip, we can again define the scale factor $\alpha = \max\{\|\mathbf{h}_k\|\}$ as the magnitude of the largest individual coefficient. However, in some cases the EQ filters for the higher modes can grow quite large at low frequencies, leading to very large coefficients and a large value of α. Applying this scale factor globally can significantly reduce the dynamic range available to the coefficients of the filters for the lower modes. There are a couple of ways to mitigate this. If the modes are to be sampled prior to beamforming, then we can apply different scale factors to each filter, and compensate after digitization. Alternatively, α can be determined using only some number of lower modes, in which case some of the EQ filter coefficients for the higher modes will still clip. Here we can repeat Eq. (45) with a couple of modifications:

$$\underset{\mathbf{h}_k,\delta}{\text{minimize}} \quad \delta \geq 0 \tag{46a}$$

$$\text{subject to} \quad \frac{1}{f_2-f_1} \int_{f_1}^{f_2} \left| \frac{\alpha H_k(f)\sigma_k(f)a_N(m_k,\theta_0,f)}{R(f)} - 1 \right|^2 df \leq \delta^2 \tag{46b}$$

$$\|\mathbf{h}_k\|^2 \leq e_{\max} \tag{46c}$$

$$|h_{k,n}| \leq 1. \tag{46d}$$

The scale factor in Eq. (46b) brings the coefficients in the lower-mode EQ filters down below the clipping level, while the magnitude constraint Eq. (46d) incorporates the attenuator clipping directly into the optimization.

The result is typically that the higher-mode EQ filters have good performance at higher frequencies, where their gain is not too large, and have reduced gain and poor performance at lower frequencies. The approach outlined above is certainly not the only way to deal with dynamic-range issues; one might instead increase the lower bandedge f_1 for selected filters in order to avoid even trying to equalize regions where the gain exceeds a threshold.

Step 3

In the third step, we take the optimized continuous-valued solution weights $\{h'_{k,n}\}$ from Step 2 and separately quantize the magnitude and phase as $\{\xi_{p(|h'_{k,n}|)}\}$ and $\{\vartheta_{q(\angle h'_{k,n})}\}$, where p and q are quantization mappings from continuous magnitude and phase to the nearest attenuator and phase-shifter indices. Now we can update the linearized hardware models of the attenuators and phase shifters and reoptimize:

$$\underset{\mathbf{h}_k, \delta}{\text{minimize}} \quad \delta \geq 0 \tag{47a}$$

$$\text{subject to} \quad \frac{1}{f_2 - f_1} \int_{f_1}^{f_2} \left| \frac{\alpha H_k(f) \sigma_k(f) a_N(m_k, \theta_0, f)}{R(f)} - 1 \right|^2 df \leq \delta^2 \tag{47b}$$

$$\|\mathbf{h}_k\|^2 \leq e_{\max} \tag{47c}$$

$$|h_{k,n}| \leq 1, \tag{47d}$$

where

$$H_k(f) = \sum_{n=0}^{N_h - 1} h_{k,n} \hat{\Xi}_{p(|h'_{k,n}|)}(f) \hat{\Theta}_{q(\angle h'_{k,n})}(f) \mathcal{T}_{k,n}(f).$$

If we again quantize the magnitude and phase of the resulting continuous weights, we should find that changes from the previous step are small, and thus they closely match the frequency responses used in the optimization. This step can be iterated if needed, each time redefining the weights $\{h'_{k,n}\}$ as the solution to the previous iteration. If the hardware responses are well behaved, then after quantization it will converge to a single solution or a small number of neighboring solutions.

Step 4

If the phase shifters have high enough resolution, then the output of Step 3 might have near-global optimal performance. For coarse quantization, however, the response can benefit from repeating the limited search approach detailed in Section 4.3, fixing the phase-shifter values for each combination and reoptimizing and quantizing the magnitude values. The optimization proceeds exactly like Eq. (44), except that now, the kth TDL frequency response for the ith phase permutation is

$$H_{k,i}(f) = \sum_{n=0}^{N_h - 1} \xi_{k,n} \hat{\Xi}_{p(|h'_{k,n}|)}(f) \Theta_{j(k,i,n)}(f) \mathcal{T}_{k,n}(f),$$

where $j(k, i, n)$ is the index of the phase shift value for the nth tap of the kth filter under the ith permutation. The resulting attenuator weights are quantized, and the error after quantization is computed in order to select the best solution.

5. HARDWARE CHARACTERIZATION

In this chapter, we will introduce and describe the various hardware components of the phase-mode beamforming system using the analysis tools from the preceding sections. We first consider two different 16-element arrays, one a stepped-notch and one a simple dipole array. We then consider the 16×16 Butler matrix and the combination with each array. This yields the modal output to be equalized, and both FIR and TDL implementations are considered and designed.

5.1   Array

5.1.1   16-Element Stepped-Notch Array

The first array used for the example designs consists of 16 vertically polarized stepped-notch elements similar to those designed and built in [11]. The layout is shown in Fig. 7. The outer radius of the array is 3 in, and the resulting interelement separation at the outer edge is one-half wavelength at approximately 5 GHz. The array was simulated in HFSS from 2–5.3 GHz to compute both the zero-position element pattern A_0 and the scattering matrix **S**. The element pattern is shown in Fig. 8. At top left, the vertical (copol) polarization component is shown across azimuth and frequency at the horizon ($\theta = 0$), with the corresponding horizontal (crosspol) component shown at top right. As can be seen, the pattern is quite broad with a negligible cross-pol component at the horizon. The bottom plots show copol and crosspol across azimuth and elevation at a fixed frequency of 4 GHz. The pattern is quite broad in elevation as well, with a loss of polarization purity at higher elevations. Such an array would be used to generate vertical fan beams centered at the horizon; elevation control could be achieved by introducing a column-array structure at each element site.
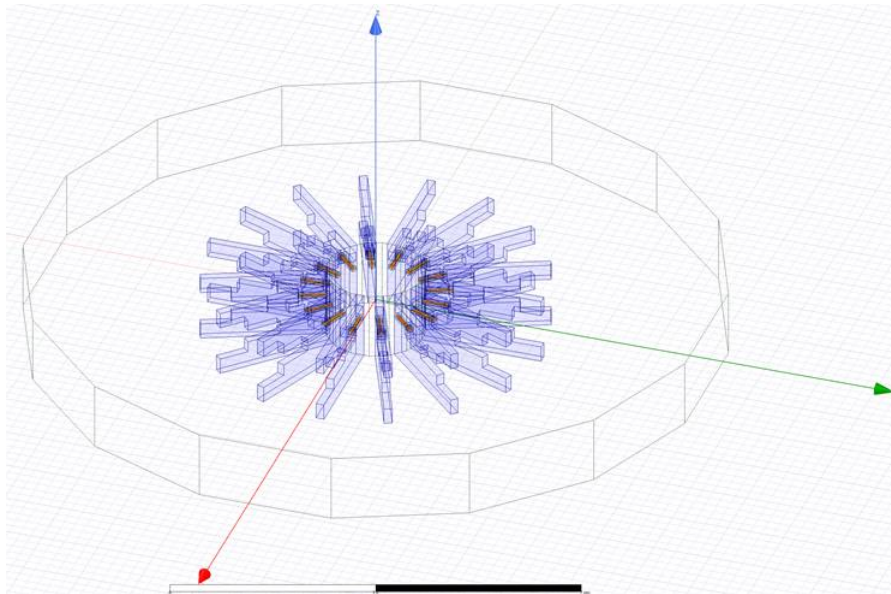

Fig. 7—The 16-element stepped-notch array used for the example design

Because this is a UCA, the scattering matrix is circulant (each row and column is a circular shift of its neighbors). As such, the scattering matrix is diagonalized by the DFT matrix:

$$\Lambda = \mathbf{D}\mathbf{S}\mathbf{D}^{-1}$$

where $\mathbf{\Lambda}$ is a diagonal matrix of modal reflection coefficients. We can equivalently write this as

$$\mathbf{SD}^{-1} = \mathbf{D}^{-1}\mathbf{\Lambda},$$

which says that for a drive signal $\mathbf{d}_m$ which corresponds to the mth column of the IDFT matrix $\mathbf{D}^{-1}$, the resulting reflection vector is simply a scaled replica:

$$\mathbf{Sd}_m = \lambda_m\mathbf{d}_m.$$

Thus modal input vectors yield reflected vectors of the same mode, and equivalently, the mode vectors are eigenvectors of the UCA scattering matrix. We can use the modal reflection coefficients to characterize how the array feed behaves when driven with an ideal Butler matrix. The left plot of Fig. 9 shows the reflection coefficients for each mode across frequency. We know from the discussion of Section 3.2.2 that a circular array cannot efficiently radiate or receive phase modes such that $|m| > 2\pi r/\lambda$, which is seen here as near-unity reflection coefficients beyond that boundary (indicated by the white lines). Driving the array with input modes above the cutoff results in near-total reflection. As a result, the total radiation power outside that boundary is negligible, as shown in the right plot of Fig. 9. We note that the radiated power at 2 GHz is a bit less than half of that at higher frequencies despite relatively low reflection coefficients for modes -1, 0, and 1; this indicates a loss of efficiency due to power dissipated in the elements rather than reflection.

The normalized element phase-mode spectrum a_N, defined in Eqs. (15) and (16) is shown in Fig. 10 for two different magnitude scales. At top, a restricted dynamic range is shown to highlight the details of the fundamental modes between $\pm N/2$, indicated by the dashed, yellow lines. The white lines indicate the propagating mode cutoff $m = \pm 2\pi rf/c$, and, as expected, we do not have significant radiation from outside of that region. We can see that the gain increases from around -4 dB at the low end to greater than 3 dB for some modes at the upper end. The apparent checkerboard pattern is a less-dramatic version of that predicted in Fig. 3, and is the result of the relatively omnidirectional element and particularly the high backlobe around 180° azimuth. The bottom plot shows a wide dynamic range in order to reveal all of the significant distortion modes, which lie outside of the dashed, yellow lines. The dashed, magenta lines bound $\pm N$, and thus the gap between yellow and magenta contains the first full set of distortion modes. The additional dotted, white lines show the propagating-mode boundary translated by $\pm N$, and indicate which propagating modes the enclosed distortion modes alias onto. Below 3 GHz, all of the propagating modes are thus "clean," but by 4.5 GHz or so, all modes have at least some distortion. This can be seen more directly in Fig. 11, which shows the modal patterns generated by driving the array with the columns of the IDFT matrix. These patterns include the distortion modes, as shown in Section 3.2.1, which manifest as ripple in azimuth with a period of $2\pi/N$. Here this ripple increases with frequency and mode index. This ripple cannot be corrected by the equalization filters, which are independent of azimuth, and thus will limit wideband nulling performance using a modal beamformer.

Up to this point we have focused on the azimuth profile of the antenna at the horizon, where the primary elevations of interest would often lie. As seen in Fig. 12, however, the array's modal patterns have significant lobes at higher elevations all the way to zenith, especially for the lower modes and higher frequencies. (Since these are the fundamental modes, their patterns are omnidirectional in azimuth.) Whether this is good or bad depends on the application; for surveillance near the horizon it represents a waste of power on transmit and increased vulnerability to interference on receive. For such applications, this array would benefit from one or more additional rows of elements in order to limit or control the elevation profile. On the other hand, these
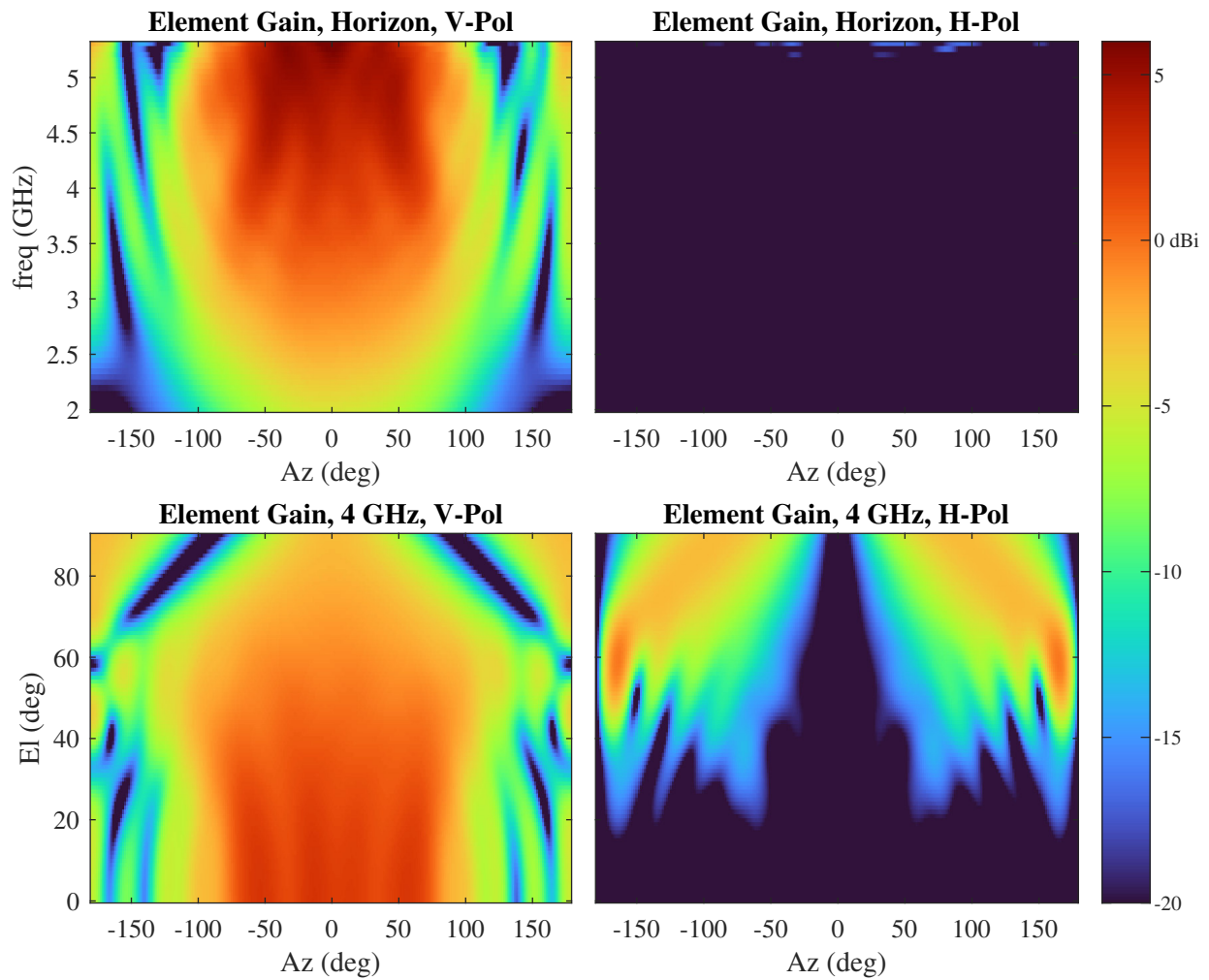
Fig. 8—Slices of the element pattern of the example 16-element vertical stepped-notch array. At top, the vertical (copol) and horizontal (crosspol) patterns are shown vs. azimuth angle and frequency at the horizon ($\theta = 0°$). At bottom, the patterns are shown vs. azimuth and elevation at a frequency of 4 GHz.
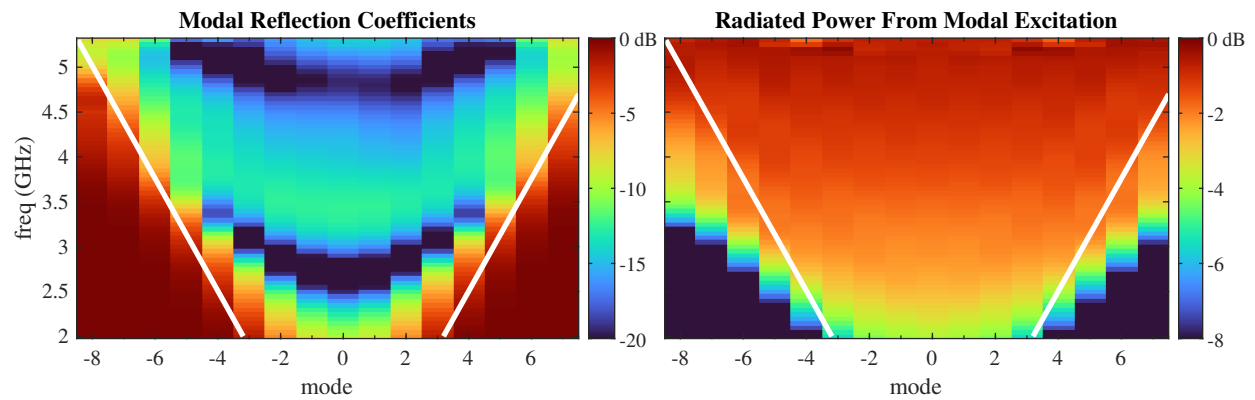
Fig. 9—The modal reflection coefficients of the example stepped-notch array, and the corresponding radiated power. The solid, white lines indicate the nominal modal cutoff of $m = \pm 2\pi r f/c$.
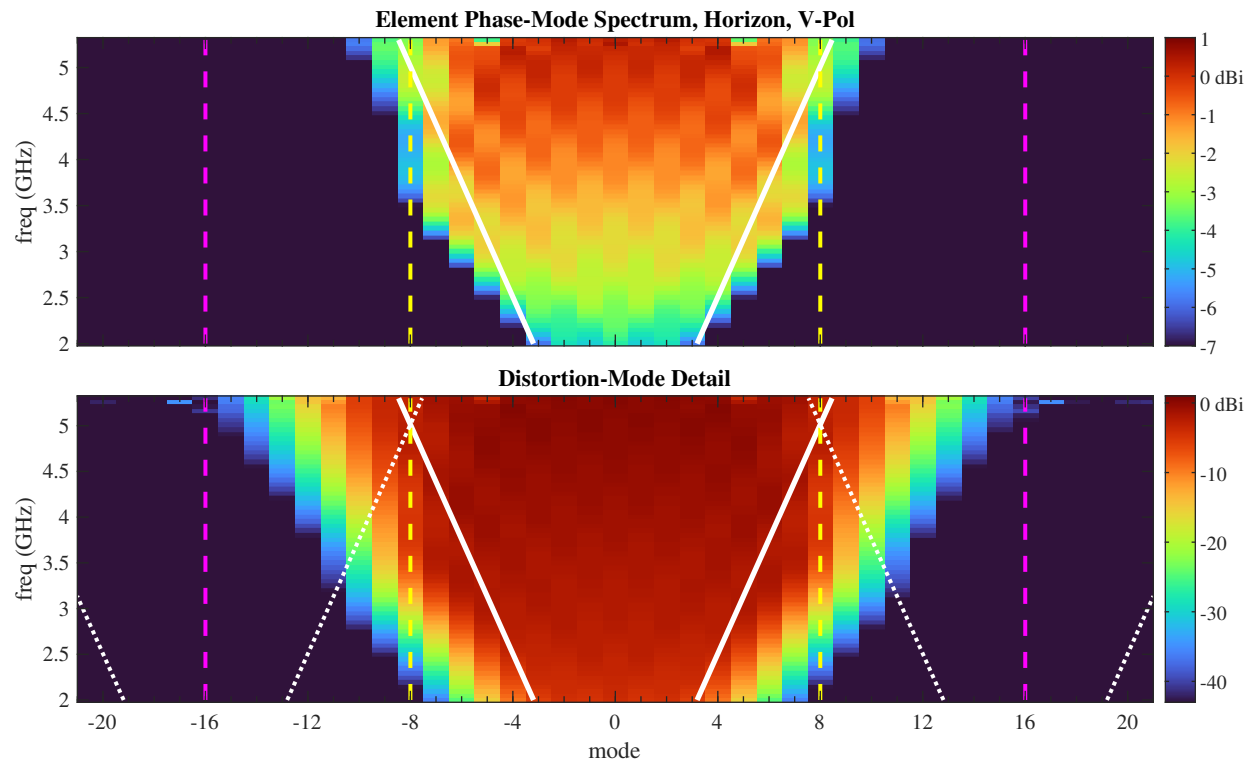
Fig. 10—The full phase-mode spectrum of an element in the example stepped-notch array, computed via Fourier series. The top plot highlights the primary radiating modes, while the bottom plot shows the distortion-mode details. The solid white lines indicate the nominal modal cutoff of $m = \pm 2\pi r f/c$, while the dotted white lines indicate the cutoff shifted by $\pm N$. The yellow dashed lines at $\pm N/2$ bound the primary modes, and the magenta dashed lines at $\pm N$ bound the first set of distortion modes.
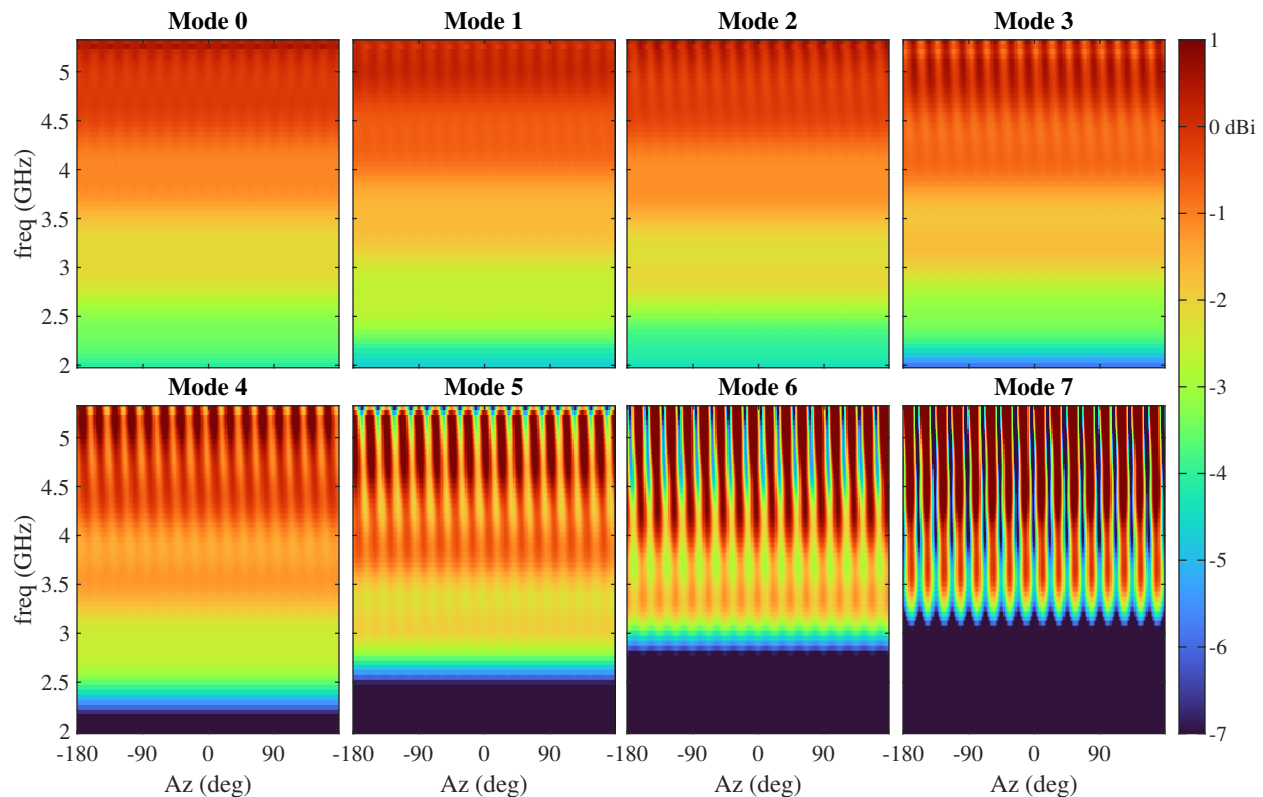
Fig. 11—The modal patterns induced in the example stepped-notch array when driven with
IDFT-matrix columns. The ripple in azimuth is caused by the distortion modes.

relatively omnidirectional patterns do enable sensing at all elevations in cases where that is desired. This will
be shown in more detail in Section 6.3.2.

5.1.2   16-Element Dipole Array

Because of some of the limitations of the stepped-notch elements (poor low-frequency response, excessive
high-elevation radiation and large backlobes), a second 16-element array was designed. The HFSS layout
is shown in Fig. 13. This array used simple vertical dipoles with a radius of approximately 4.3 in, which
corresponds to a half-wavelength element spacing at around 3.5 GHz. The larger radius was chosen to shift
the optimal operating frequency range downward, and the corresponding increase in the dipole height would
be expected to narrow the elevation beamwidth. Given the omnidirectional azimuth pattern of an isolated
dipole, however, improvement in the backlobe is not obvious. However, as will be seen, this is the result once
embedded within the array.

The embedded element pattern for the dipole array is shown in Fig. 14, with the top row showing a horizon
cut across frequency and the bottom row showing the full pattern at 3.5 GHz. Comparing to Fig. 8, we can
see the aforementioned improvements. The backlobes around 180° azimuth are significantly reduced, as is
radiation above 45° elevation or so. As a result, the forward gain at the horizon is greater for the dipole as
well over its simulated frequency range. While both elements have excellent cross-polarization suppression at
the horizon, the dipole array maintains better suppression at higher elevations.

Fig. 12—The elevation-gain profile of the stepped-notch array for the primary 16 modes vs. frequency. Both polarizations are included, although the H-pol contributions are limited to the upper elevations.

Fig. 13—The 16-element dipole array used for the example designs

The modal reflection coefficients and the total radiated power per mode are shown in Fig. 15. The reflection coefficients show that the dipole array is well matched from about 3 GHz up to 4.5 GHz, while 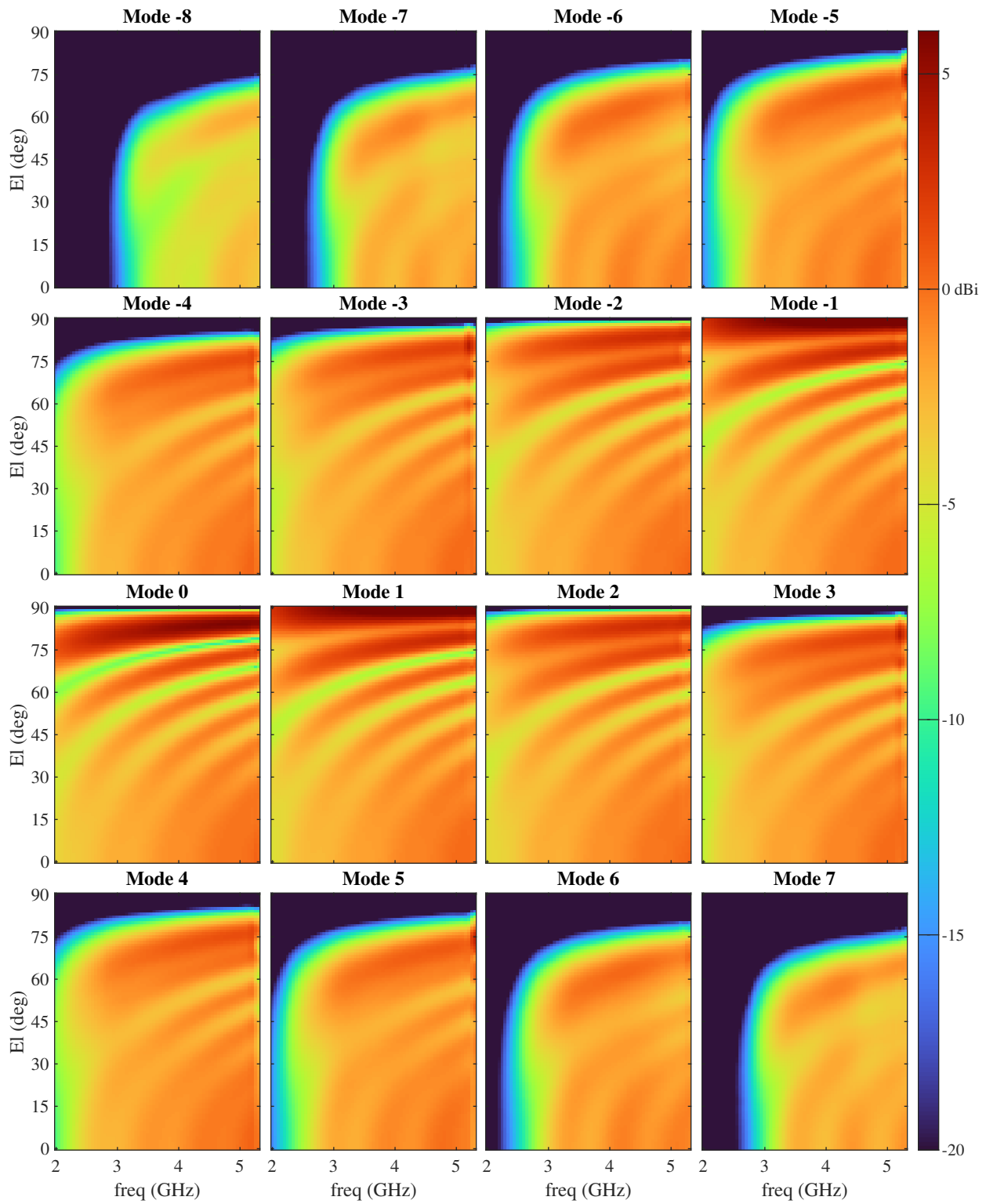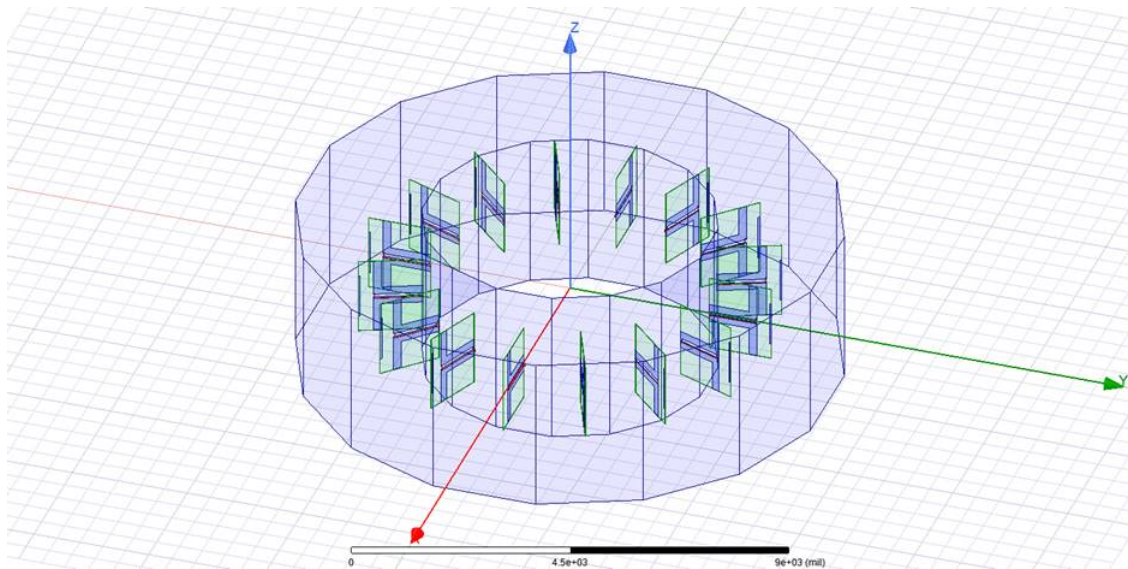the radiated power shows that it is a reasonably efficient radiator over that same range with best efficiency between 3 GHz and 3.7 GHz. Comparing to Fig. 9, we see that the stepped-notch array has (as expected) a wider matching and radiation bandwidth than the dipole array, and its optimum operating band is tuned for higher frequencies owing to its reduced geometry. Focusing specifically on the horizon, Fig. 16 shows the phase-mode spectrum at two different amplitude scales as before. This suggests that useful operation could extend up to 4.5 GHz, as the decreasing efficiency is partially compensated by the increasing gain of the embedded element. Comparing the top plot to that of Fig. 10, we see that the dipole's phase-mode spectrum is smoother across modes, with less of the striping/checkerboard pattern seen in the notch array. This is largely due to the reduced backlobe of the dipole, which leads to less cancellation in alternating modes and less energy pushed to higher elevations. We also see that the dipole array has considerably higher gain than the notch array over much of the frequency range of interest (note the different amplitude-scale offsets). Comparing the bottom plot with that of Fig. 10, we see that the dipole array also has reduced distortion modes compared to the notch array.

The effect of the distortion modes is to introduce ripple in the azimuth patterns corresponding to each mode when driven with a modal beamformer. The ripple that results from using an ideal (DFT) beamformer is shown in Fig. 17 for modes 0 through 7 at the horizon. We can see that the ripple increases both with increasing mode number and with increasing frequency. Visually, the ripple in the dipole modes is comparable to Fig. 11, and the main difference between the two is that the dipole array has about 3 dB more gain. If we instead look at the elevation profile of the mode patterns at 0° azimuth, as shown in Fig. 18, we can see that the radiated energy is largely concentrated below 30° elevation, with some higher-elevation sidelobes increasing above 3.8 GHz or so. Compared to the stepped-notch array profiles in Fig. 12, however, we see that the dipole transmits far less energy at higher elevations.
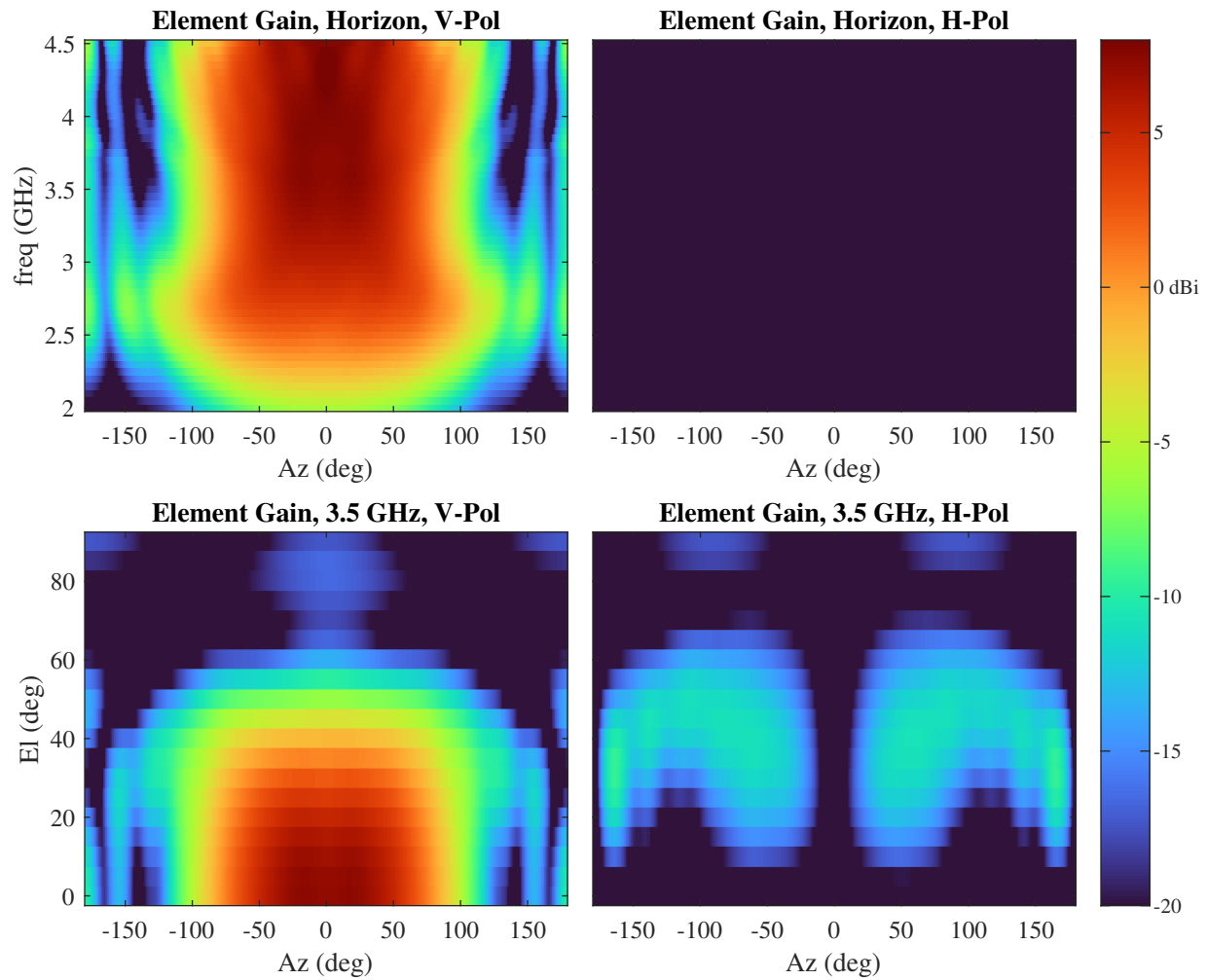
Fig. 14—Slices of the element pattern of the example 16-element vertical dipole array. At top, the vertical (copol) and horizontal (crosspol) patterns are shown vs. azimuth angle and frequency at the horizon ($\theta = 0°$). At bottom, the patterns are shown vs. azimuth and elevation at a frequency of 3.5 GHz.
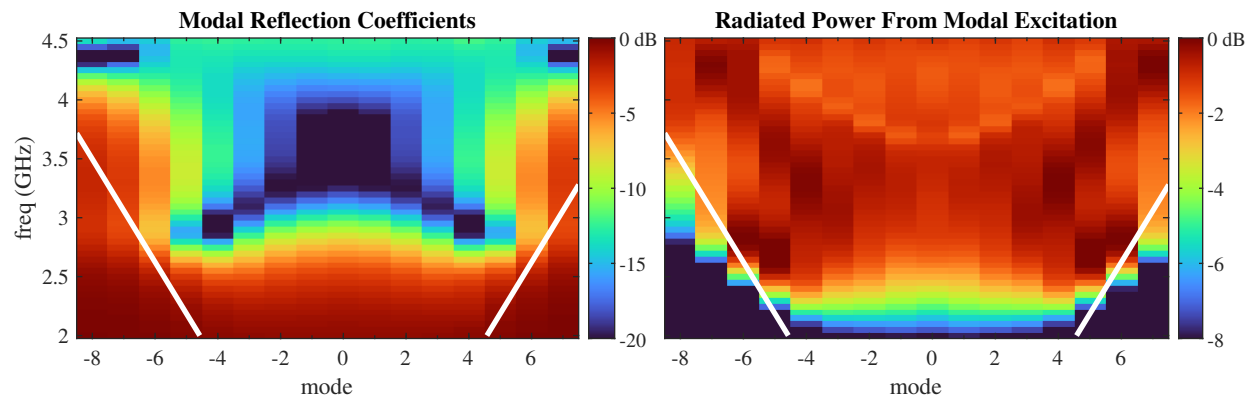
Fig. 15—The modal reflection coefficients of the dipole array, and the corresponding radiated power. The solid, white lines indicate the nominal modal cutoff of $m = \pm 2\pi r f / c$.
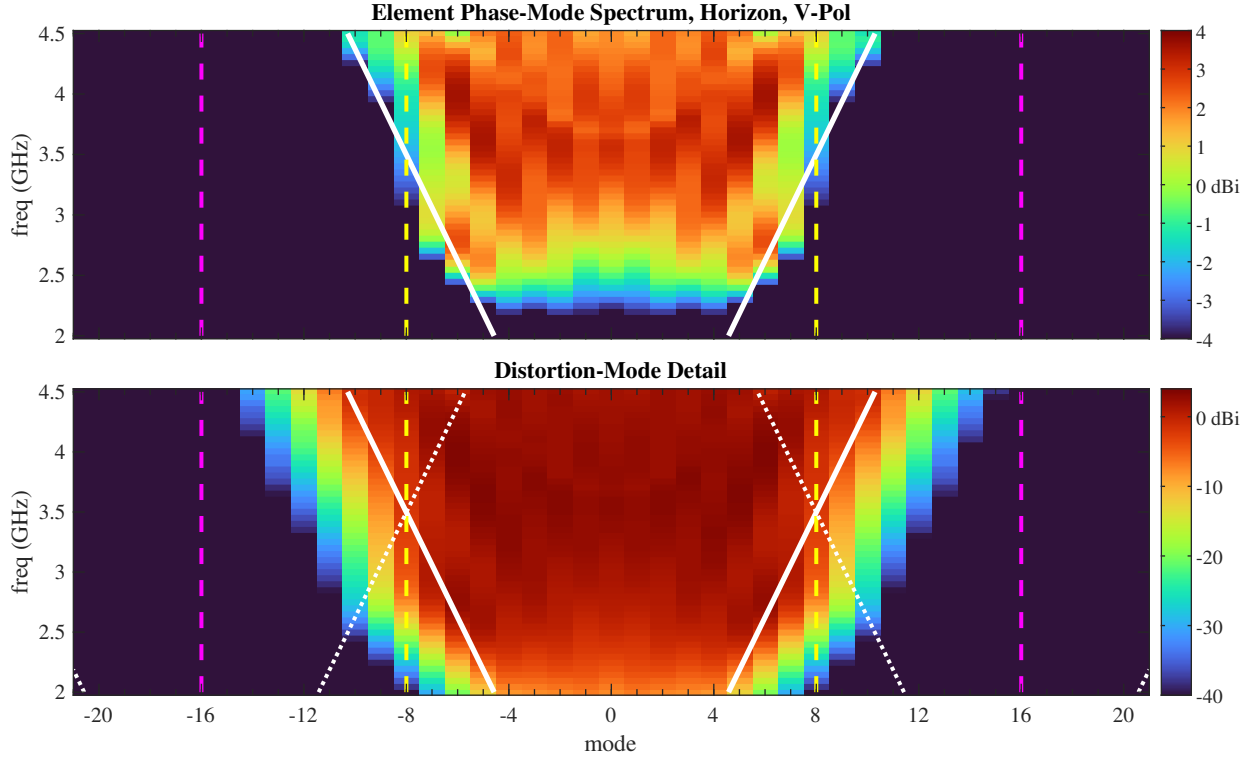
Fig. 16—The full phase-mode spectrum of an element in the example dipole array, computed via Fourier series. The top plot highlights the primary radiating modes, while the bottom plot shows the distortion-mode details. The solid, white lines indicate the nominal modal cutoff of $m = \pm 2\pi r f / c$, while the dotted, white lines indicate the cutoff shifted by $\pm N$. The yellow, dashed lines at $\pm N/2$ bound the primary modes, and the magenta, dashed lines at $\pm N$ bound the first set of distortion modes.

5.2   Butler Matrix

The phase-mode beamformer in our example circular array is implemented as a Butler matrix, which is just the analog implementation of a DFT matrix. The design of the 16×16 Butler matrix used here is discussed in detail in the three year-end reports [31–33], and so will be only briefly described here. The schematic for the Butler matrix is shown in Fig. 19, showing the classic FFT butterfly structure. It is implemented using 90° hybrids and a small set of phase-shifter values using a slight modification of the scheme presented in [57]. The modification was to account for the physical layout of the hybrids used in the design, which was different than that in [57]. The only effect on the ideal response of the matrix is that several of the output modes are 180° out of phase from their DFT values. Since each mode will have a dedicated equalizer filter, this negation is harmless and will be incorporated into the filters. The red labels at the top (input) of the matrix indicate sequential element number around the array, while the black labels enumerate the corresponding ports in the simulated scattering matrix. Similarly, the red and black labels at bottom enumerate the modes and their corresponding ports. The modes are shown here jumbled as they come out of the Genesys simulation, but we will silently assume they are remapped to their natural ascending order to yield the matrix response $\mathbf{B}(f)$.

We will analyze the Butler matrix response through the decomposition of Eq. (29). We first consider the diagonal matrix of mode transfer functions $\boldsymbol{\Sigma}(f)$, which represent the effective frequency response applied to
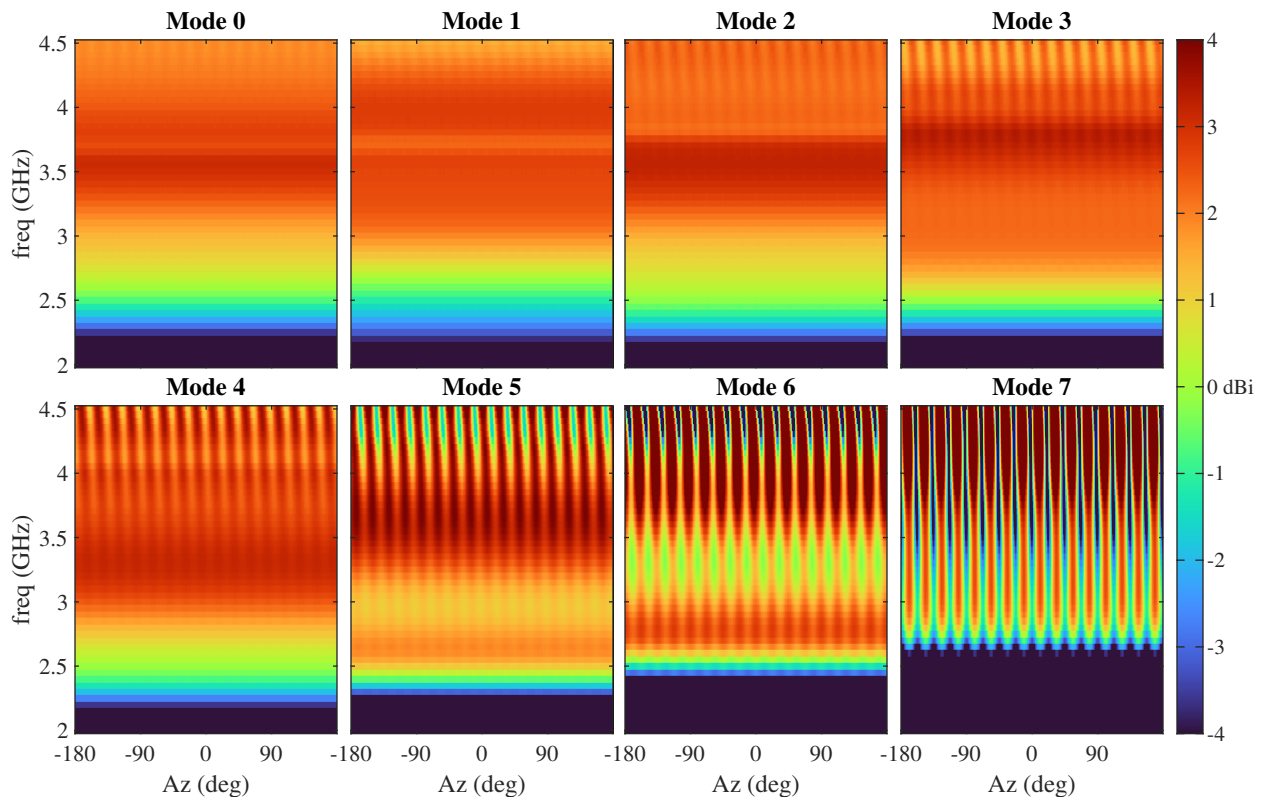
Fig. 17—The modal patterns induced in the dipole array when driven with IDFT-matrix
columns. The ripple in azimuth is caused by the distortion modes.

each mode. These responses, in cascade with the array's own modal frequency responses, will be compensated by the equalization filters and thus do not fundamentally represent errors given sufficient EQ degrees of freedom. The diagonal entries of $\mathbf{\Sigma}$ corresponding to each mode in the simulated Butler matrix are plotted in Fig. 20. At top is the magnitude response, showing a slow rolloff with increasing frequency and roughly 0.5 dB variation between the various responses for frequencies between 2.75 GHz and 4.5 GHz or so. Below and especially above this frequency range, the responses increasingly deviate from each other. The bottom plot shows the correponding group delay for each response. Again the responses are well-matched (and mostly flat) between 2.75 GHz and 4.5 GHz, with significant ripple above and below.

The errors that cannot be corrected by the EQ filters are modeled in the matrix $\mathbf{E}(f)$, which has a zero diagonal (sometimes called a *hollow* matrix). The kth row of $\mathbf{E}$ represents frequency responses that couple all of the other modes into mode m_k. As discussed in Section 3.4.2, the result is azimuth ripples in the phase-mode responses. We can visualize $\mathbf{E}$ various ways. Figure 21 shows the magnitudes of the entries of $\mathbf{E}$ at a few selected frequencies. In general, all the coupling coefficients are less than -20 dB for frequencies between 3 GHz and 4.5 GHz. We can take the norm of each row of $\mathbf{E}$ pointwise at each frequency to provide a measure of the total error coupled into each mode, which yields the plot of Fig. 22. Here we see that the error is fairly consistent between modes, rising from below -20 dB at 3 GHz to below -15 dB at 4.5 GHz. This is significantly larger than the errors due to the distortion modes in the lower modes of either array; as such, we expect overall beamforming errors to be dominated by the Butler matrix rather than the arrays themselves.
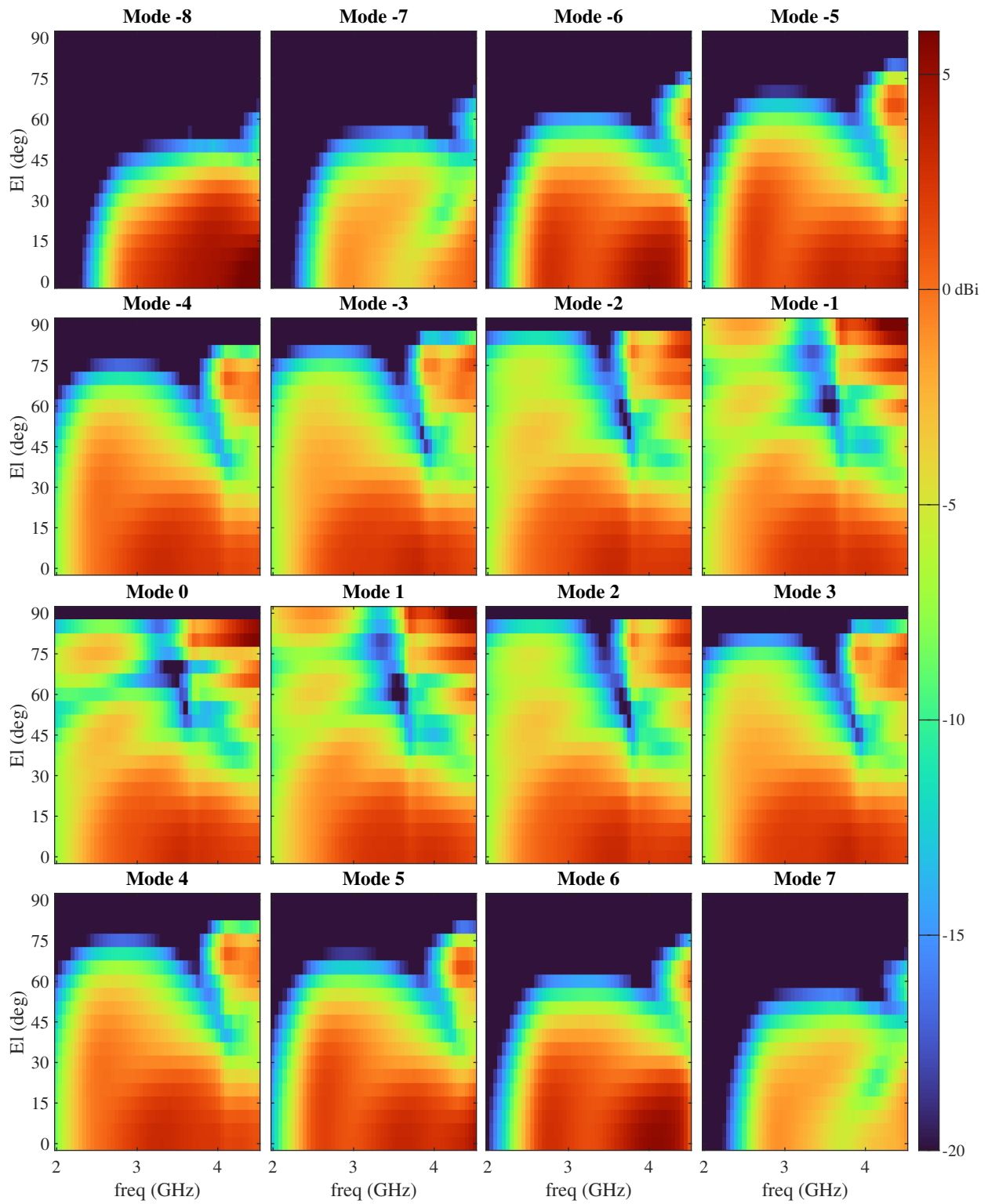
Fig. 18—The elevation-gain profile of the dipole array for the primary 16 modes vs. frequency. Both polarizations are included, although the H-pol contributions are limited to the upper elevations.
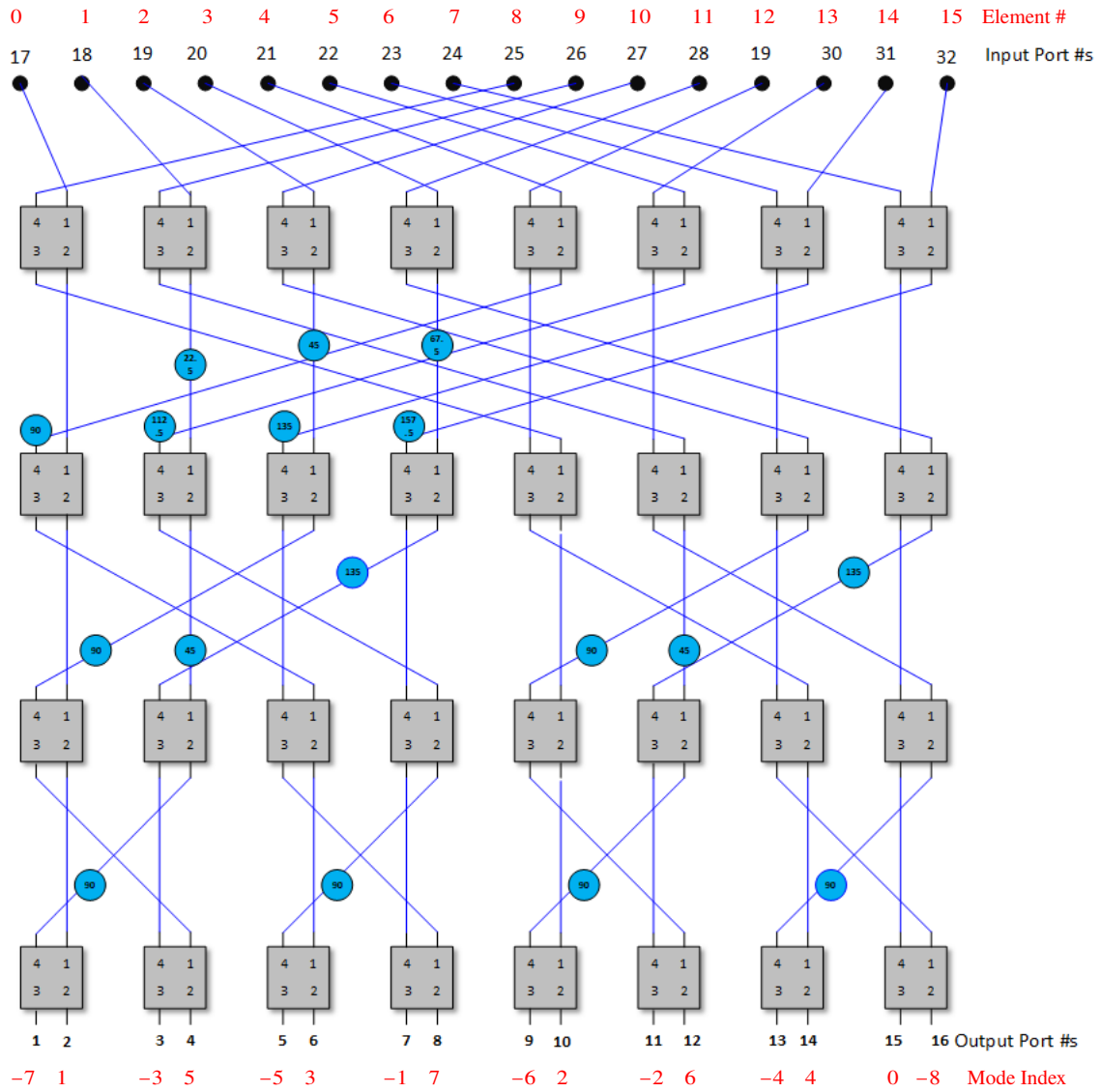
Fig. 19—16 × 16 Butler matrix layout. The boxes are 90° hybrids and the circles are phase shifters. The red labels at top and bottom give the element index and mode index, respectively, that correspond to the port numbers (in black).
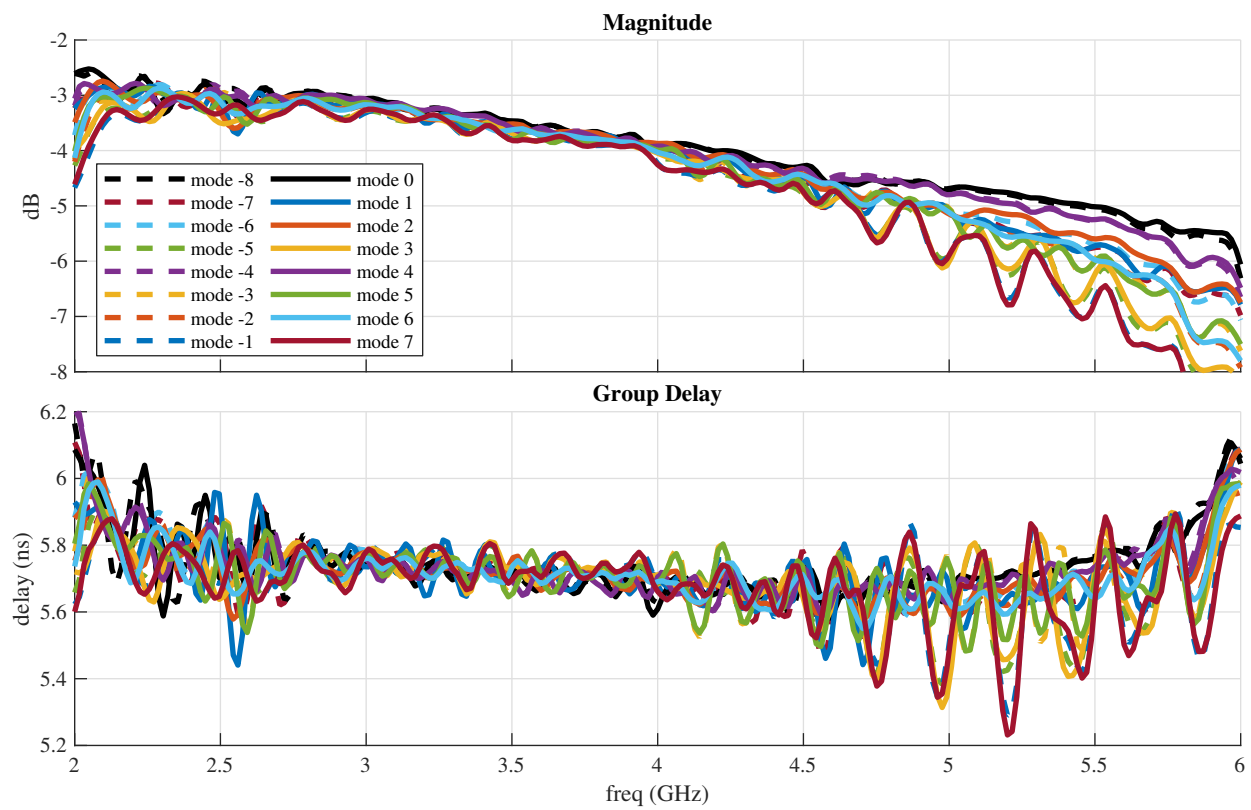
Fig. 20—The modal transfer functions of the 16 × 16 Butler matrix
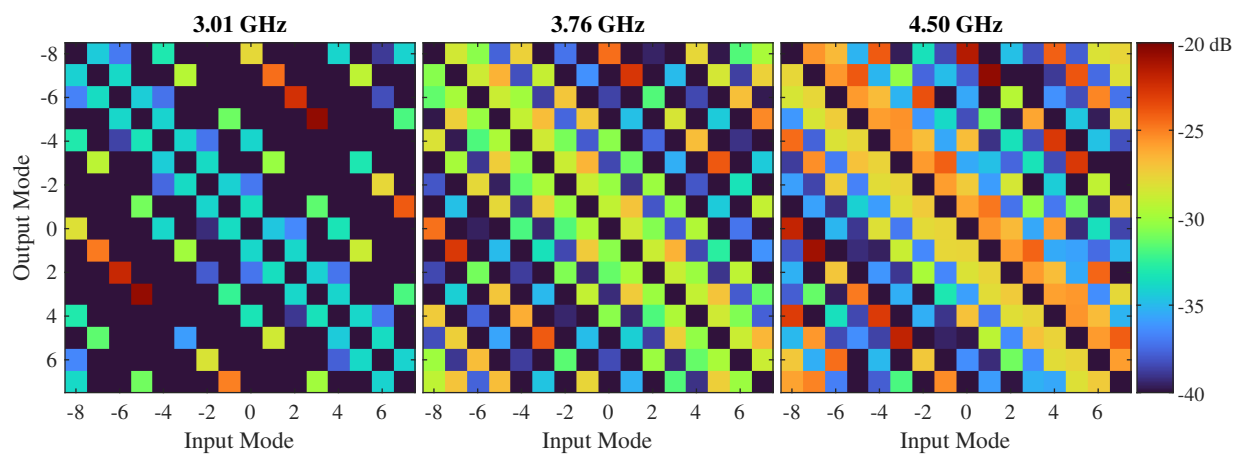
Fig. 21—Magnitude of Butler-matrix error response $\mathbf{E}(f)$ at selected frequencies

Butler-Matrix Error Row Norm
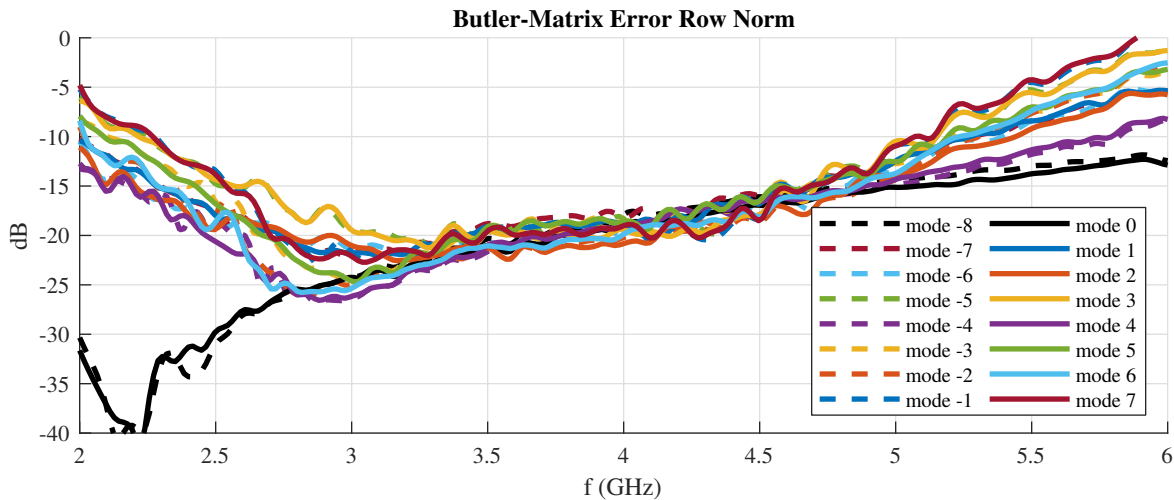
Fig. 22—Total energy in each row of the Butler-matrix error response $\mathbf{E}(f)$

5.3 Comparing Array and Butler Matrix Errors

Having separately characterized the arrays and the Butler matrix, we now compare their respective errors in the normalized form of Eq. (39). This will yield a sense of the overall magnitude of the error responses and determine which errors dominate.

Figure 23 shows the errors for the dipole array, while Fig. 24 shows the errors for the notch array. In both plots, the normalized distortion-mode errors $\hat{\mathbf{a}}_D(\phi, \theta_0, f)$ at the horizon are shown at top for modes $0, \ldots, 7$; the negative modes are similar. Here we see again that the distortion-mode error grows with increasing frequency and with increasing mode. There is not much difference between the two arrays' distortion-mode errors viewed at this scale. The distortion mode error magnitudes are largely constant across azimuth angle, indicating that a single distortion mode dominates. At the bottom of each figure, the normalized Butler matrix errors $\hat{\mathbf{E}}(f)\mathbf{a}(\phi, \theta_0, f)$ are shown at the horizon. These show considerable variation across azimuth, as they include all of the fundamental modes mixed together. The errors for the notch array are somewhat stronger than the dipole array, which is a result of the lower gain in the notch array (and thus higher-gain ideal equalization filters). The overall shape of the Butler-matrix-induced errors is largely the same between the arrays, since the same Butler matrix model was used for each.

Comparing the distortion-mode errors to the Butler-matrix errors, it is clear that for most modes and frequencies, the Butler-matrix errors dominate. The exceptions are the higher modes and frequencies where the distortion modes approach the same gain as the fundamental modes. The distortion-mode errors are highly frequency dependent but omnidirectional, while the Butler-matrix errors are highly azimuth dependent but only weakly frequency dependent between 2.5 GHz and 4.5 GHz. Above and below that range, the Butler matrix degrades significantly.

5.4 Equalization Filtering

Each mode in the beamformer requires a separate equalizer filter, either a digital FIR filter if the modes are sampled first or an analog TDL filter of the form shown in Fig. 6. For this project, an eight-tap delay line was

Normalized Dipole Distortion-Mode Errors

Normalized Dipole/Butler-Matrix Errors

Fig. 23—A comparison of the normalized pattern errors due to the dipole-array distortion modes (top) and the pattern errors from the cascade of the dipole array and the Butler matrix

Normalized Notch Distortion-Mode Errors

Normalized Notch/Butler-Matrix Errors

Fig. 24—A comparison of the normalized pattern errors due to the notch-array distortion
modes (top) and the pattern errors from the cascade of the notch array and the Butler matrix

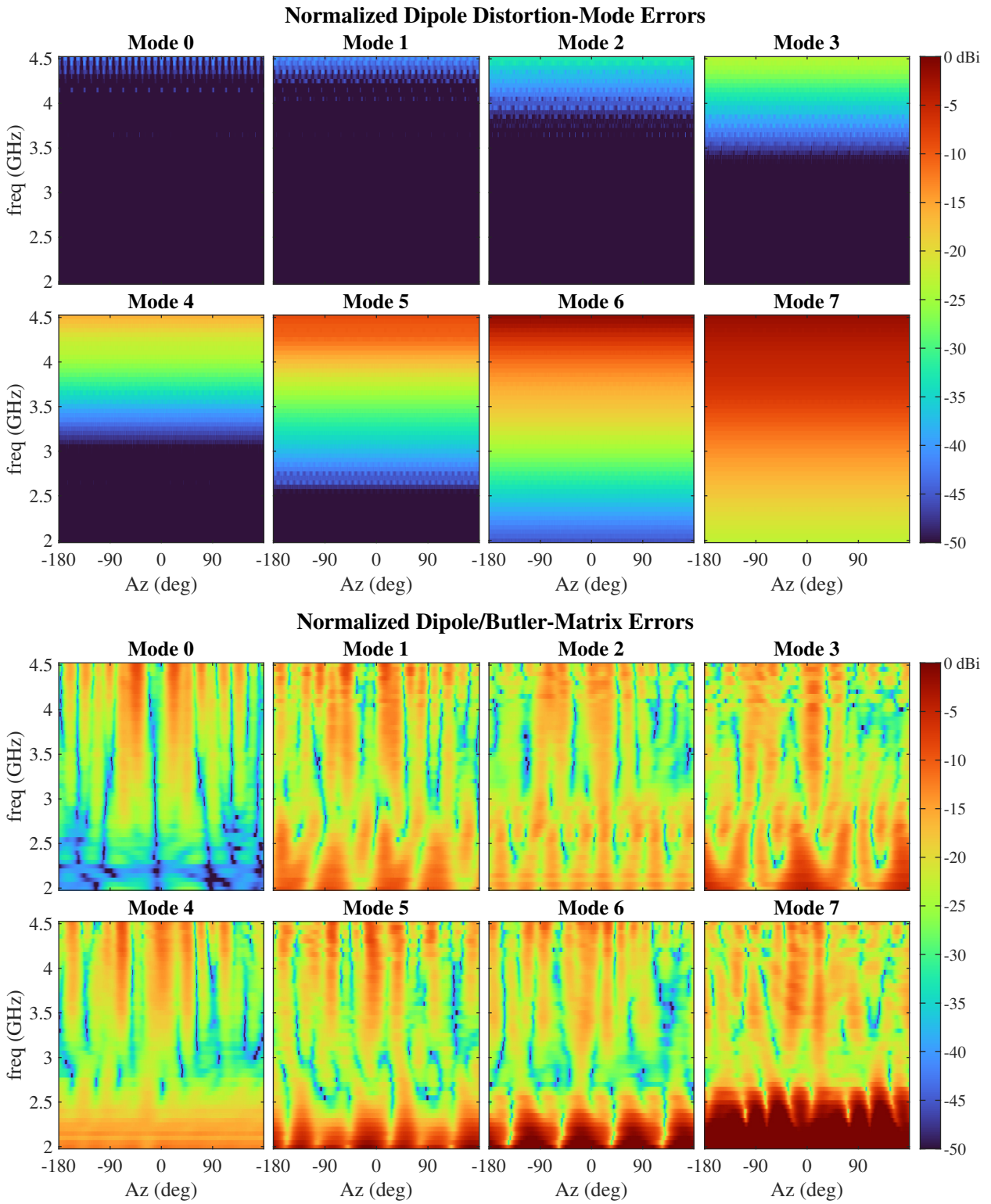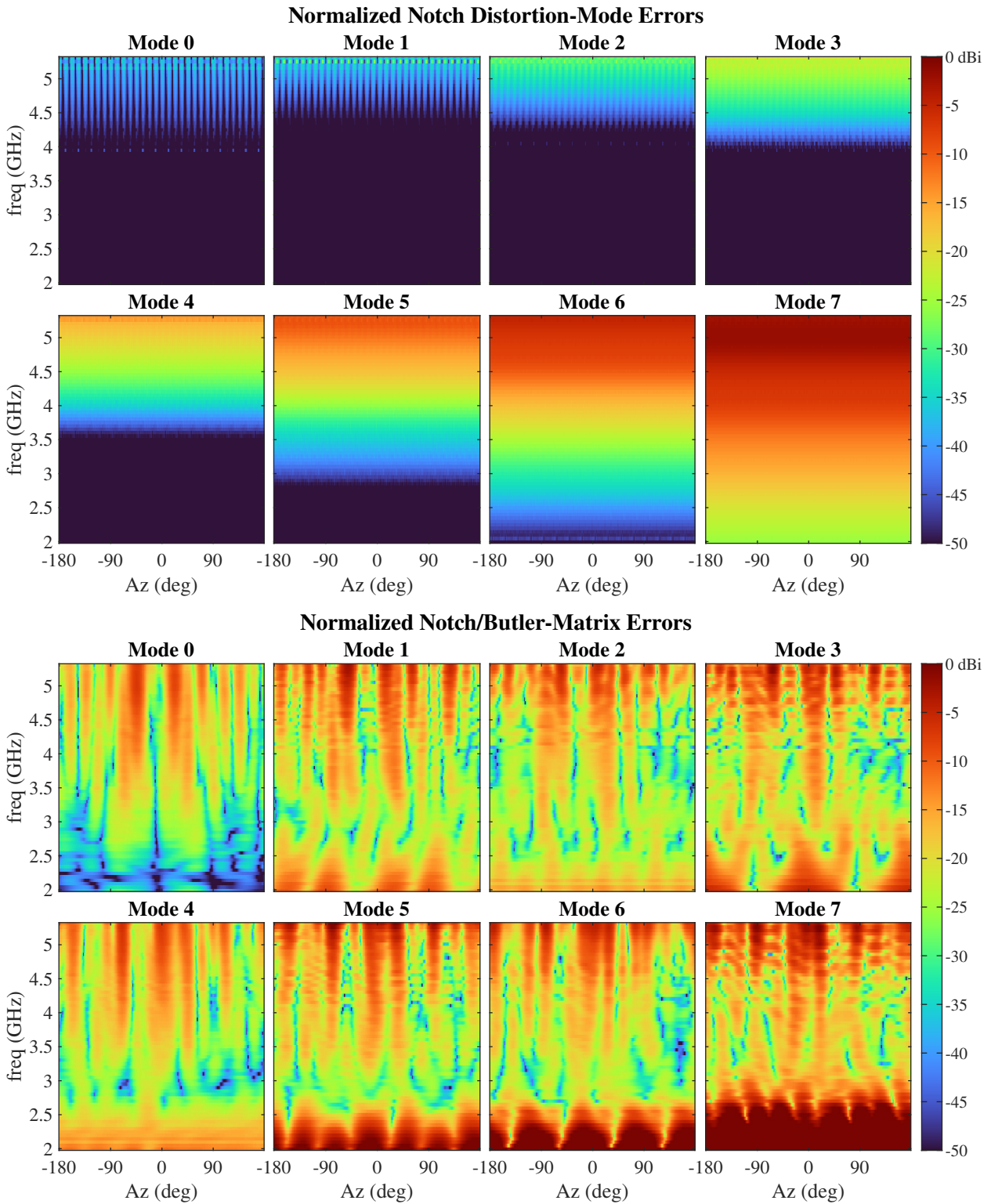designed, with the layout shown in Fig. 25. It is constructed as a three-level binary tree of Wilkinson power dividers with additional binary-valued delays on each divider's lower leg. A matching 8:1 combiner was also designed without the additional delays. The frequency responses of each output in the delay line are shown in Fig. 26. Although the full TDL filter was not constructed owing to resource limitations, a COTS programmable attenuator and several COTS phase shifters were identified and characterized via manufacturer-provided S parameters. The relevant parameters for each component are given in Table 1. The phase shifters cover overlapping frequency ranges, and the manufacturer data extends well beyond the nominal limits, allowing the simulation of TDL equalizers for several intervals of operation. By incorporating the actual frequency responses into the TDL optimization, as detailed in Section 4.4, reasonable operation can be achieved outside of the nominal ranges.

Table 1—Programmable Attenuator and Phase Shifters Identified as
Candidates for TDL Filter

Attenuator Model	Nominal Frequency Range	Bits	Step
Hittite/Analog Devices HMC1119	2–6 GHz	7	0.25 dB
Phase-Shifter Model			
Qorvo TGP2108-SM	2.5–4 GHz	6	5.625°
MA/COM MAPS-010164	2.3–3.8 GHz	6	5.625°
MA/COM MAPS-010144	2.3–3.8 GHz	4	22.5°
MA/COM MAPS-010165	3.5–6 GHz	6	5.625°
MA/COM MAPS-010145	3.5–6 GHz	4	22.5°

As defined in Eq. (35), the role of the equalization filtering is to compensate the net frequency responses of each mode due to the array and Butler matrix, $\sigma_k(f)a_N(m_k, \theta_0, f)$, such that the equalized versions match some reference response $R(f)$. The unequalized modal responses for modes $0, \ldots, 7$ are shown in Fig. 27 for both arrays. We can see that the responses are relatively flat above about 2.75 GHz for the dipole and 3.5 GHz for the notch, with the higher modes rolling off below these cutoffs. This is largely driven by the arrays themselves, as derived in Section 3 and illustrated in Section 5.1. Equalizing these regions of low gain thus requires a wide filter dynamic range as well as a large noise gain. The reference response for equalization was defined to be the zero-mode response with an additional delay equal to half the length of the EQ filter: $R(f) = \sigma_0(f)a_N(0, \theta_0, f)e^{-j2\pi f 3.5 T_s}$. This ensures that the equalization filter for mode 0 has a nominally flat response and a centered delay, and will remove any large magnitude or phase variation that is common to all of the modes. The references for each array are shown in Fig. 28; here we see that the dipole does have significant magnitude rolloff at lower frequencies while the notch is relatively flat across frequency. The group delay response is nearly identical for each save an offset, as the phase response is dominated by the (common) Butler matrix. These reference responses can in turn be equalized out with a single filter after beamforming, if desired. The ratio of the modal responses and the reference responses yields the ideal EQ responses of Eq. (38), which are shown in Fig. 29. We will approximate these responses over select frequency bands using FIR and TDL filters.

The FIR and TDL filters were designed with delay steps of 0.5 ns, matching the physical delay line. This yields a periodic frequency response with period of 2 GHz. In practice, one cannot independently control the response over a full period due to the boundary conditions with the adjacent period as well as the limited degrees of freedom (taps). Thus, we will limit ourselves to 1.75 GHz design intervals, which represent 87.5%
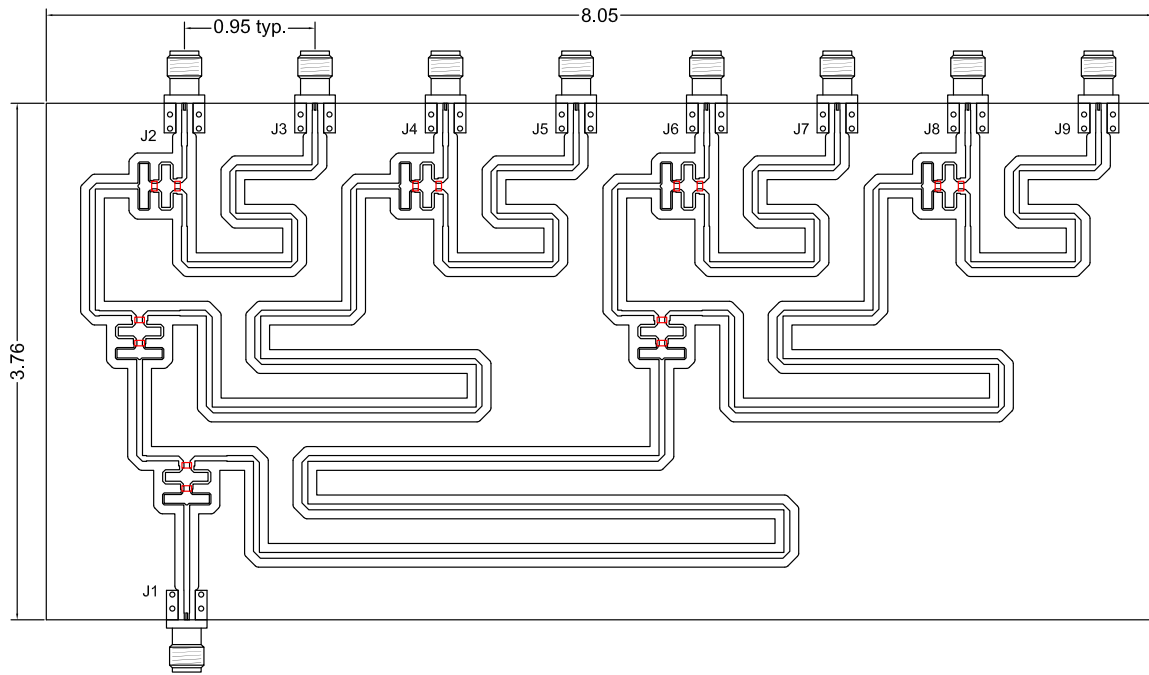
Fig. 25—Layout of the eight-tap delay line designed for the EQ filters
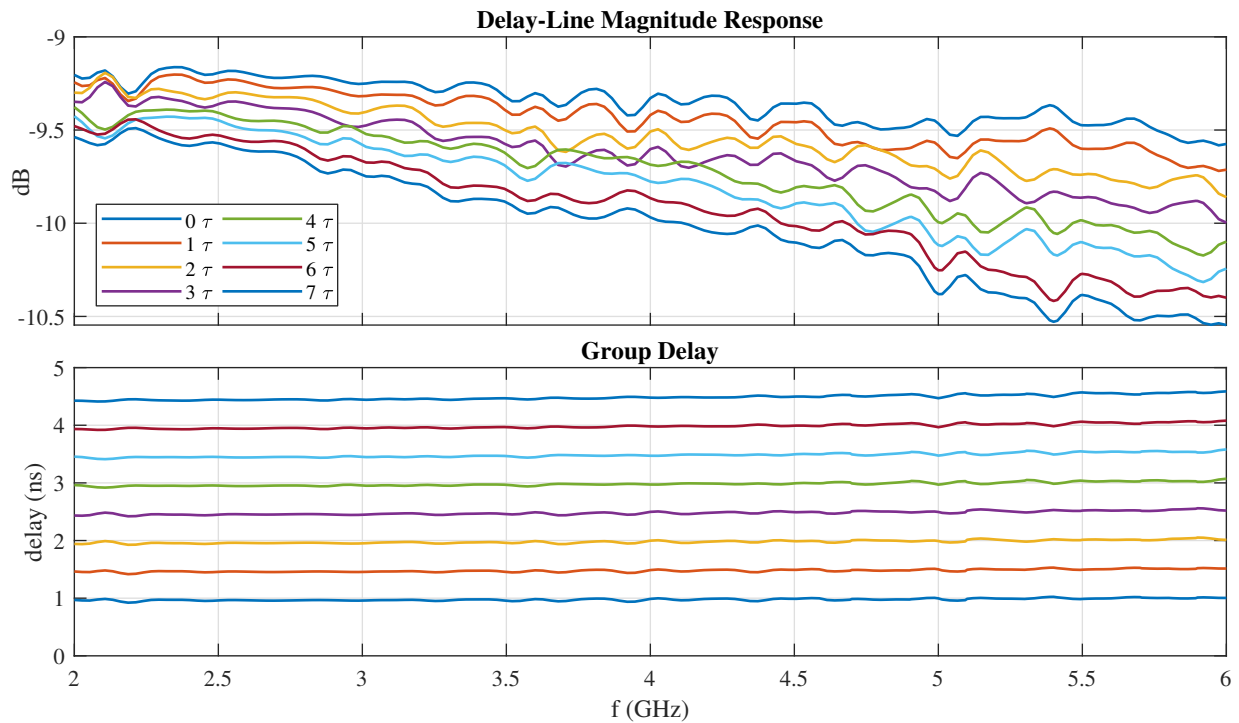

Fig. 26—Frequency response of each arm of the delay line. The unit of delay is τ = 0.5 ns.

Modal Frequency Responses, Dipole Array

Modal Frequency Responses, Notch Array
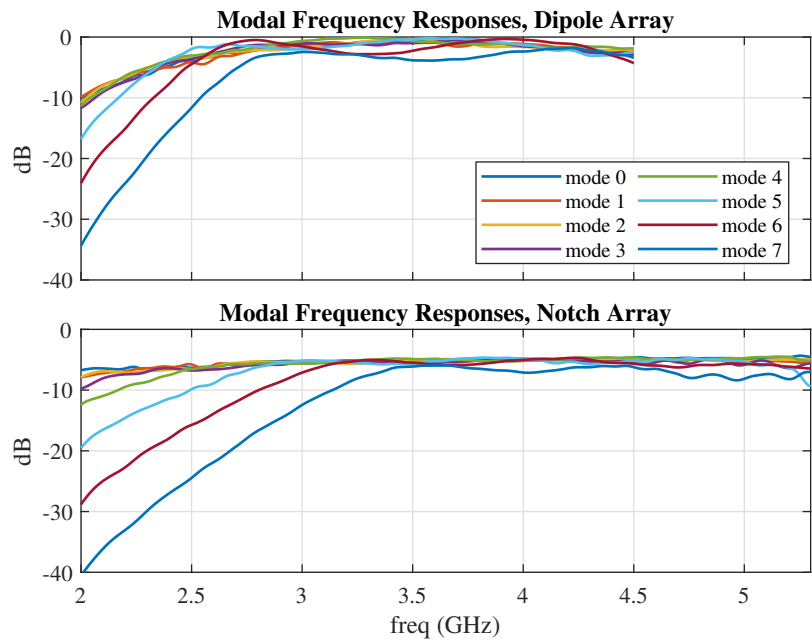
Fig. 27—The horizon modal frequency responses for the two arrays

Reference Responses, Magnitude

Group Delay
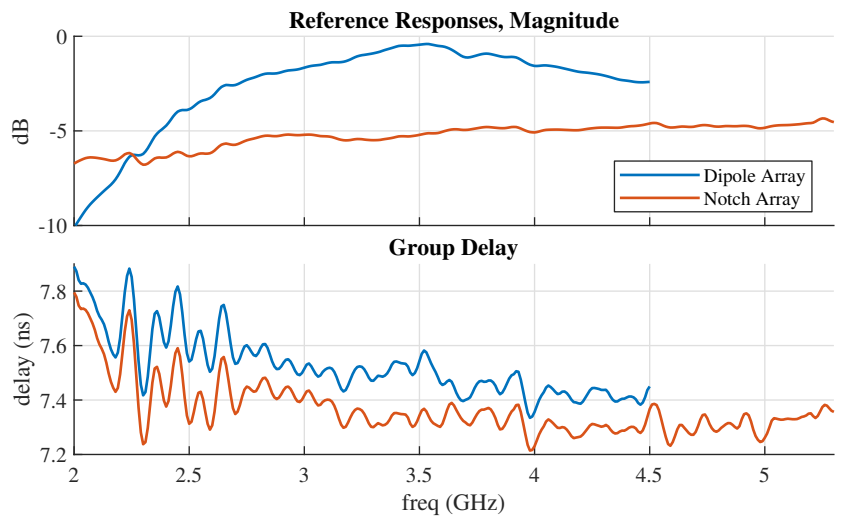
Fig. 28—The reference (mode 0) frequency responses for the two arrays
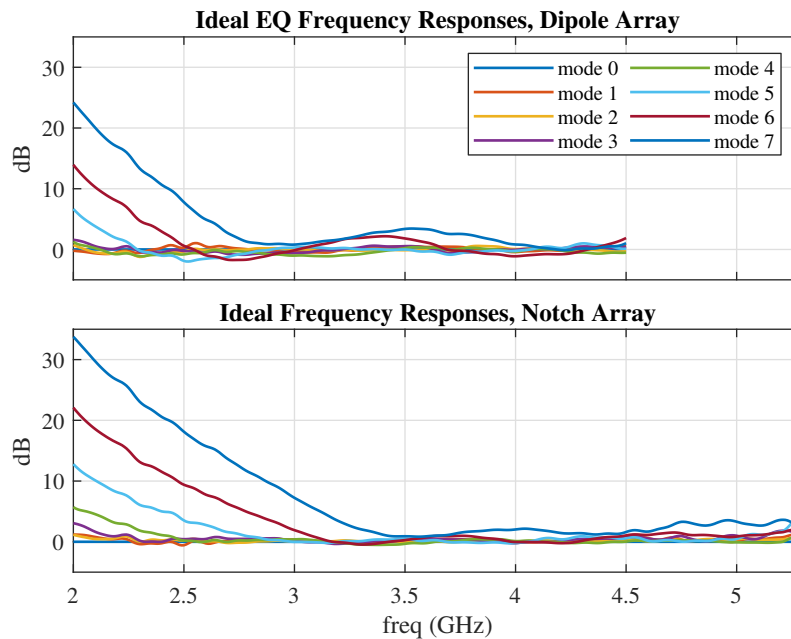
Fig. 29—The ideal equalization-filter responses for the two arrays

of the full band. Better equalization performance can be achieved by reducing this bandwidth further; however, here the equalizaton errors generally did not dominate. For the dipole array, the band [2.5 GHz, 4.25 GHz] covers most of the practical bandwidth, as the gain rolls off below and above. The notch array itself can operate over a wider band, from 2 GHz to above 5 GHz, but the overall system is limited by the Butler matrix frequency response. Here we choose to show results for the band [3 GHz, 4.75 GHz] as representative.

Both FIR and TDL equalizer filters were designed for each array, following the optimization approaches outlined in Section 4. The FIR filters assumed effectively infinite coefficient precision with no dynamic range limits, while the TDL filters were limited to 7-bit attenuators with 0.25 dB steps and either 4-bit or 6-bit phase shifters, and incorporated S-parameter models of the delay line, attenuators, phase shifters, and combiner. The resulting equalizer responses are shown in Fig. 30 for the dipole array and Fig. 31 for the notch array. The corresponding equalization error defined in Eq. (35) is shown in Fig. 32. One period of the FIR and TDL filters for modes 0–7 is shown, with the dashed, vertical lines indicating the region under design. The responses for the negative modes are very similar. We can see that the FIR and TDL responses generally match each other fairly well, and they match the ideal response with varying quality. Where the ideal response group delays oscillate rapidly, the EQ filter responses remain smooth due to the limited degrees of freedom. In mode 7 of Fig. 31, we can see the result of limiting the dynamic range of the attenuation values in the TDL; the ideal and FIR responses rise quickly below 3.25 GHz, while the TDL filter instead rolls off. If the notch array were operated at a lower frequency, this would be seen in lower modes as well.

We can compare the mean-square error (MSE) of various EQ responses in order to quantify their performance more directly. In particular, we want to compare the FIR error to various TDL implementations. This includes simply quantizing the FIR coefficients and using them in the TDL, fully optimizing the TDL, as well as intermediate results from the TDL optimization after steps 2 and 3. We also want to quantify the performance loss in using 4-bit vs. 6-bit phase shifters. We illustrate these comparisons in Fig. 33, which
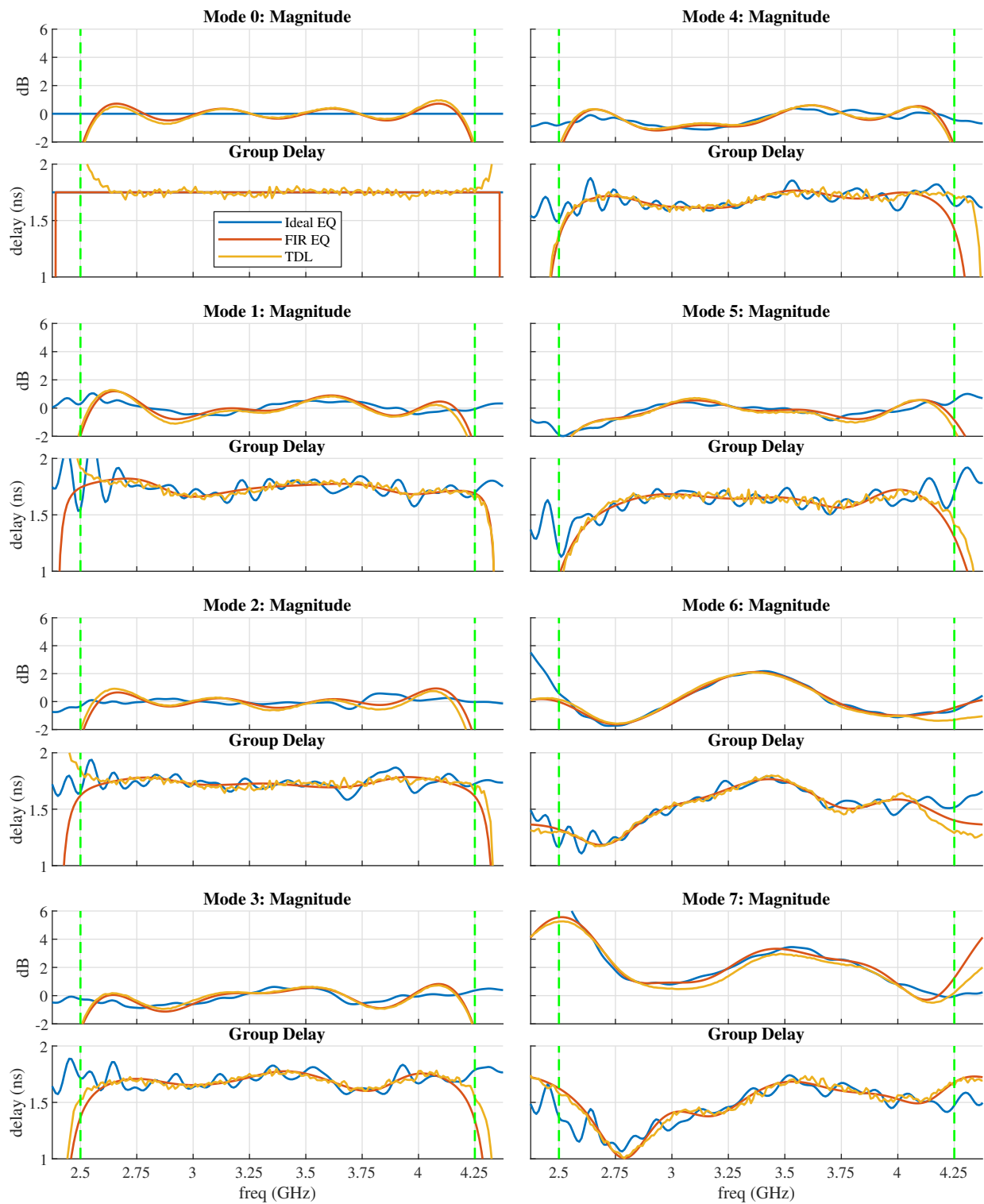
Fig. 30—A comparison of the frequency responses of different EQ filters for the dipole array. The FIR filter has 8 taps and infinite precision, while the TDL has 8 taps and uses 7-bit attenuator and 6-bit phase coefficients. The dashed, vertical lines indicate the design frequency bounds.
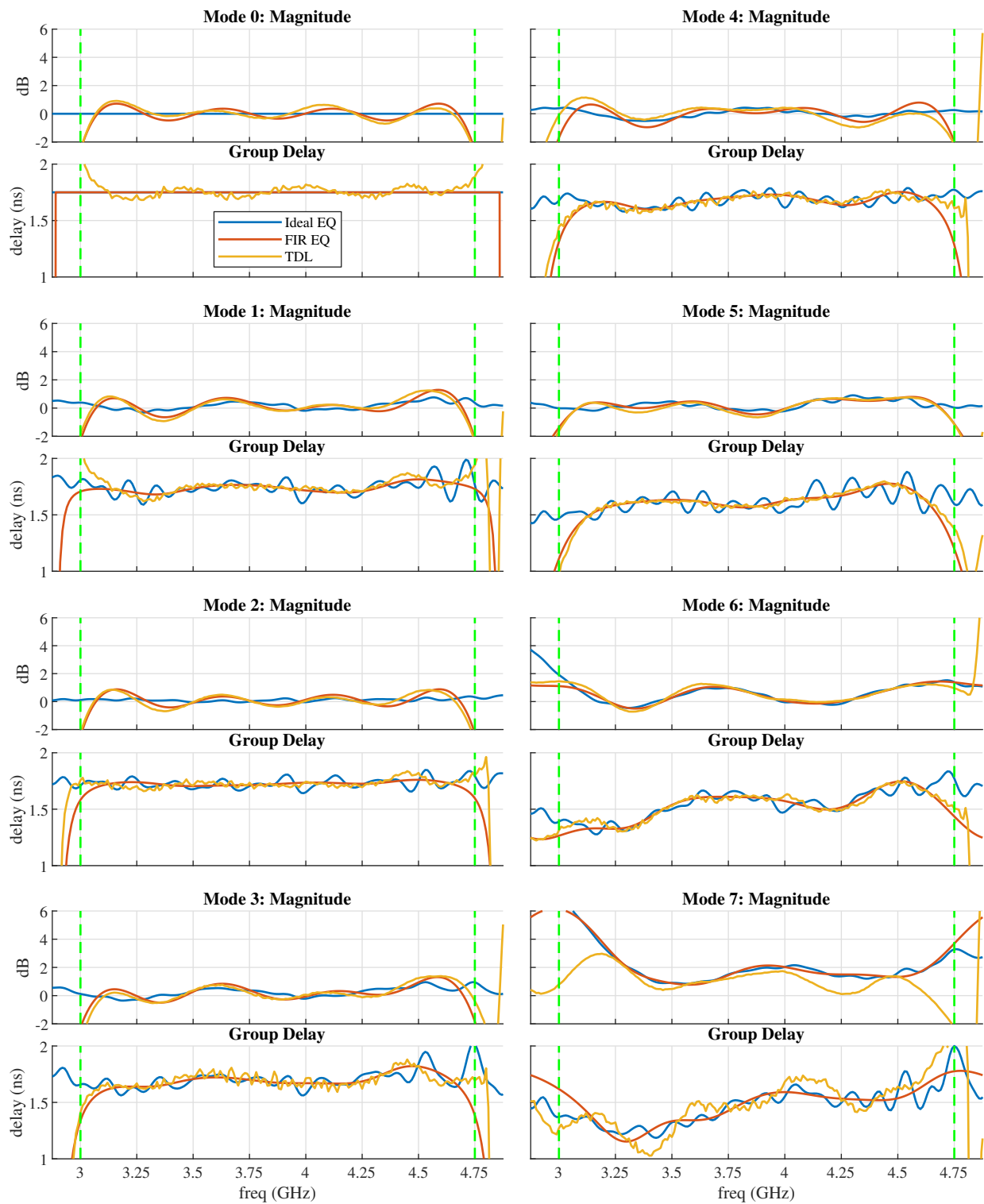
Fig. 31—A comparison of the frequency responses of different EQ filters for the notch array. The FIR filter has 8 taps and infinite precision, while the TDL has 8 taps and uses 7-bit attenuator and 6-bit phase coefficients. The dashed, vertical lines indicate the design frequency bounds.
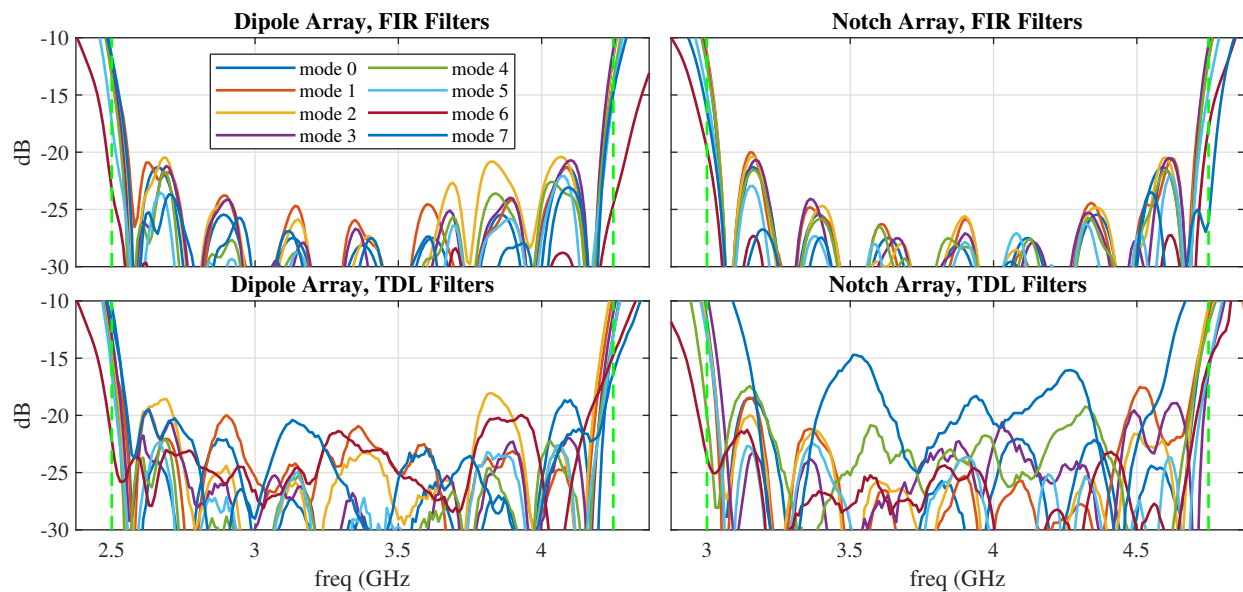
Fig. 32—A comparison of the equalization error frequency responses for FIR and TDL filters
for both arrays

shows the MSE for each mode. The left plots correspond to the dipole array, the right plots to the notch, with 6-bit phase shifters at top and 4-bit phase shifters at bottom. We can that, as expected, the optimized FIR filter has the lowest MSE for all but one case, and that the fully optimized TDL filter has the next-lowest MSE. Using the quantized FIR weights for the TDL generally has higher MSE, particularly for the notch array. And we can see that the TDL weights after the initial steps of the optimization procedure can have relatively high error as well, with as much as 10 dB reduction between steps 2 and 4. FIR equalization performance was about the same between the dipole and notch arrays, with TDL performance a bit better for the notch array. The MSE for the higher modes, primarily mode −8 for the dipole and including modes −7 and 7 for the notch, is higher for the TDL responses, largely due to the excessive dynamic range required. Finally, comparing 6-bit to 4-bit phase shifters, we see generally higher MSE and also more variation in MSE across the modes. This is presumably a result of the quantized values randomly lying closer to or further from the ideal values. The MSE for the FIR and 6-bit TDL filters is below −20 dB for all but the highest modes, which is lower than the Butler-matrix errors and thus the latter will tend to dominate. (We can see from Fig. 32 that the peak errors are generally lower than −20 dB as well, other than at the band edges.) The 4-bit TDL filters have MSE below −15 dB for most modes, which is on par with the Butler matrix and thus would be a more marginal choice.
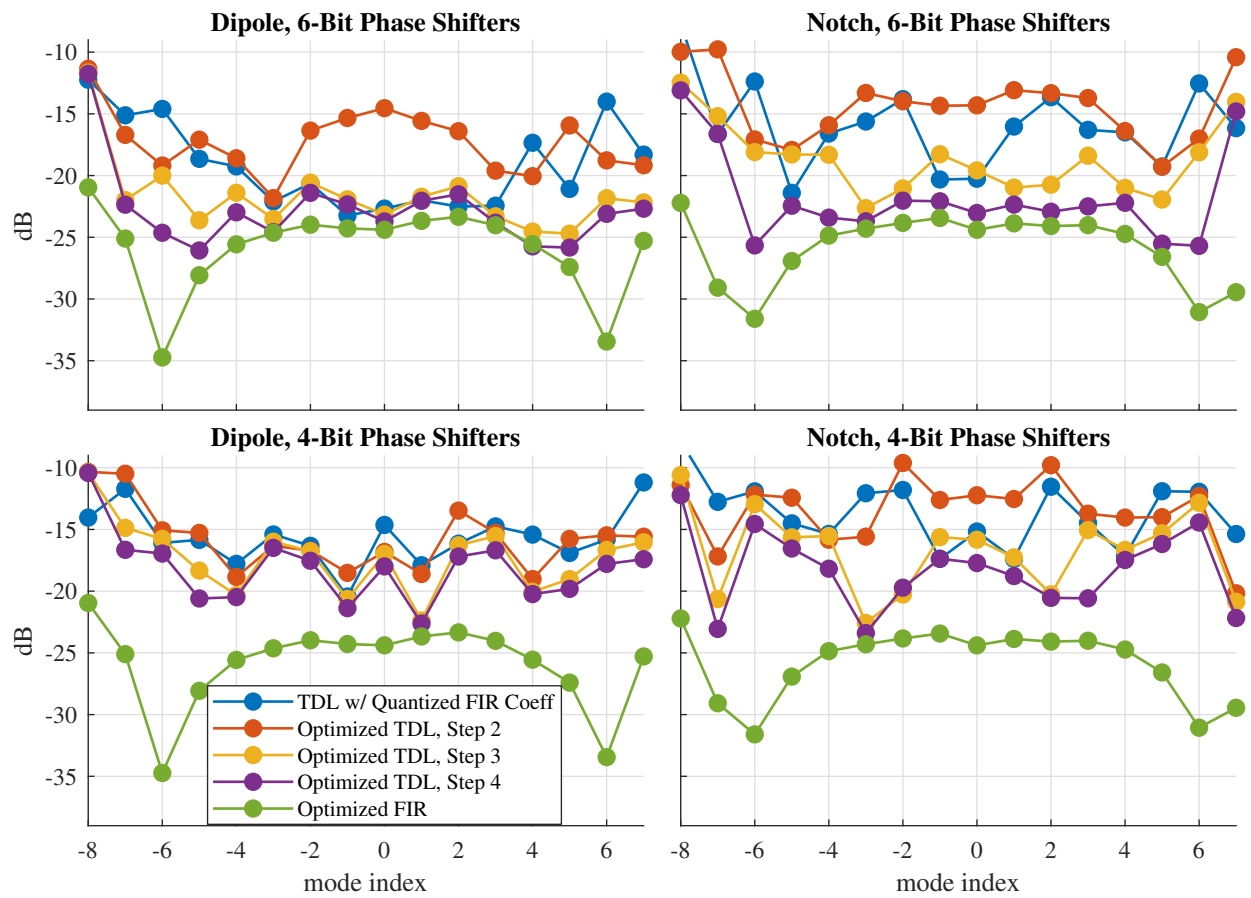
Fig. 33—A comparison of the mean-square equalization error for different filter designs

6.   BEAMFORMING

Having characterized the various hardware components in our notional phase-mode beamforming system, we now put them all together and consider how well they perform as a beamformer. We will simulate the two different arrays over several frequency ranges to see the quality of the resulting array pattern $A(\phi, \theta, f)$ as defined in Eq. (26), or equivalently with various levels of error decomposition in Eqs. (30) and (37). With the hardware responses and EQ coefficients now fixed, what remains is to design the weights $\mathbf{w}$. This will be done via three different approaches. In the first section, we will implement standard deterministic array patterns using array tapers. In the second section, we will directly optimize the narrowband weights in an attempt to improve sidelobe levels over the taper approach. Finally, in the third section, we will consider adaptive beamforming operation.

6.1   Standard Tapers

In keeping with the virtual linear array analogy of the phase-mode beamformer, we can form and steer deterministic beams from the phase-mode beamformer using standard linear-array tapers to determine the weights applied to the equalized modes. At the reference elevation, we can expect similar patterns as with a true linear array but without the distortions seen approaching endfire. Although we have the 16 modes $-8, \ldots, 7$ available for beamforming, the use of mode -8 is problematic for reasons that will be illustrated shortly. Thus, we will mostly focus on odd-length tapers using a symmetric set of modes. We will also use these familiar standard patterns to examine the effects of different equalization methods on beamforming.

We first consider applying a uniform taper on the modes $-7, \ldots, 7$ to each array. For the dipole and notch arrays, we will look at the frequency bands 2.5–4.25 GHz and 3.0–4.75 GHz, respectively. The resulting patterns are shown in Fig. 34 for the dipole array and Fig. 35 for the notch array. For each array type, four different sets of equalization filters were used. The top plot in each figure shows ideal equalization, as defined by $\mathscr{E} = 0$ in Eq. (36). This would be representative of a long FIR filter. The second plot shows an 8-tap FIR filter, with infinite-precision coefficients. The third plot shows an 8-tap TDL filter using the 7-bit attenuator and 6-bit phase shifter as designed in Section 5.4, while the fourth plot uses only a 4-bit phase shifter. For the FIR and TDL filters, the nominal design bandwidth is demarcated by the horizontal, white lines, which represents 1.75 GHz/2 GHz = 87.5% of one period of the filter response. Visually, all of the equalizers perform about the same, which reinforces that the EQ is not the dominant source of error. In all four plots, we can see the classic Dirichlet-kernel (sampled-sinc) response, with the vertical, white lines indicating the expected locations of the 14 nulls. We can see that at the low end of the band, we have very good correspondance, but at the upper end of the band, an "extra" null sneaks in. This is due to some combination of the distortion modes of the arrays and the Butler-matrix errors, both of which get worse at higher frequencies. Effectively, even though we are only intending to excite modes $-7, \ldots, 7$, at higher frequencies, we are also partially exciting modes ± 9 and higher as well as coupling between modes. Comparing the two arrays, the primary difference we see is that the dipole array has about 3.5 dB more gain, which is consistent with the array characterizations in Section 5.1.

We next consider a standard Chebyshev taper with -30 dB sidelobes, with the resulting plots shown in Fig. 36 for the dipole and Fig. 37 for the notch. While the sidelobes are somewhat lower than the uniform taper, they are well above the expected level, peaking above -20 dB. This again is due to the distortion modes and the Butler matrix errors, which have more impact on a low-sidelobe taper than a uniform one.

One way to mitigate the effects of the array distortion modes is to only use the lower-magnitude modes, effectively shortening the virtual linear array. Figure 38 compares uniform and Chebyshev patterns using

modes $-7, \dots, 7$ vs. only using modes $-4, \dots, 4$ from the notch array. We see the expected broadening and reduction in the number of nulls from the reduced array size, but also see more consistency in the sidelobe and null locations as the most-significant distortion modes are zeroed out. There is still increasing error at the highest frequencies, which is likely due to the Butler matrix in accordance with its error performance shown in Fig. 22. Another effect of limiting the modes used for beamforming is that it extends the lower usable bandwidth of the array, which can be seen by comparing the first and third plots to the second and fourth plots of Fig. 38 below 2.5 GHz. This is because the higher modes have very poor gain at lower frequencies, which, in turn, require very high equalizer gain to compensate. This increases the noise at the output much more than the signal, reducing overall array gain.

A major advantage of a circular array is the ability to steer 360° in azimuth without the beam broadening and loss of gain seen in linear arrays as they steer away from boresight. However, steering also reveals yet another effect of the distortion modes on the array pattern. Let us consider mode -8 in particular, which, per Eq. (17), receives exactly the same weight as mode 8. Because the tapers we have looked at are symmetric and have so far been applied without any phase steering such that the $\{w_m\}$ are purely real, this coupling is harmless or even advantageous in a sense, as it gives us a 17th mode for free. However, steering the beam to some azimuth angle ϕ_0 requires weights $\{w_m e^{-jm\phi_0}\}$, and now $e^{-j8\phi_0} \neq e^{j8\phi_0}$ except when $\phi_0 = 2\pi k/16$ for some integer k. At all other steering angles, we will have a phase discontinuity in mode 8. This can be seen in Fig. 39, where the top plot shows a uniform-weighted pattern using all 16 modes steered to a "good" azimuth of 45° at top compared to steering to a "bad" angle of 52° in the second plot. Considerable smearing and filling in of the nulls is evident in the second plot. The bottom two plots repeat the experiment but use only modes $-4, \dots, 4$; here the sidelobe structure is largely unchanged. Note that the overall pattern shape is invariant to the amount of steering owing to the circular symmetry of the array, whereas a linear array steered to 90° would show significant distortion and loss of gain.

Finally, let us consider the elevation profiles of uniform-weight array patterns for each array. Figure 40 shows the full pattern in azimuth and elevation for each array at two different frequencies. We can see that the pattern sidelobes are largely constant from the horizon up to about 30° elevation for the dipole array, and perhaps 30° for the notch array. The mainbeam shape and gain of the notch array are fairly consistent up to 80° or higher, while the dipole array is more concentrated at lower elevations. (This contributes to the better horizon gain of the dipole.) The differences between the elevation profiles of the two arrays will be relevant when considering adaptive beamforming in Section 6.3.

6.2 Optimized Patterns

In the previous section it was shown that conventional array tapers can be used to design the narrow-band array weights, with certain caveats and limitations. A more sophisticated approach for deterministic beamforming is to directly optimize the weight vector **w** in order to get the desired array-pattern properties. As shown in Eq. (26), the array pattern is linear in **w**, and thus the usual design metrics such as peak and mean-square sidelobes are convex quadratic functions of **w**. Several methods can be used to solve such probles, here we will again use SOCP.

Consider the following SOCP optimization problem:

$$\underset{\mathbf{w}, \delta}{\text{minimize}} \quad \delta \geq 0 \tag{48a}$$

$$\text{subject to} \quad |A(\phi_m, \theta_0, f_n)| \leq \delta, \quad \phi_m \in \Phi_{\text{SL}}, \, f_n \in \mathcal{F}_{\text{PB}} \tag{48b}$$

$$\text{Re}\{A(\phi_0, \theta_0, f_0)\} \geq 1, \tag{48c}$$
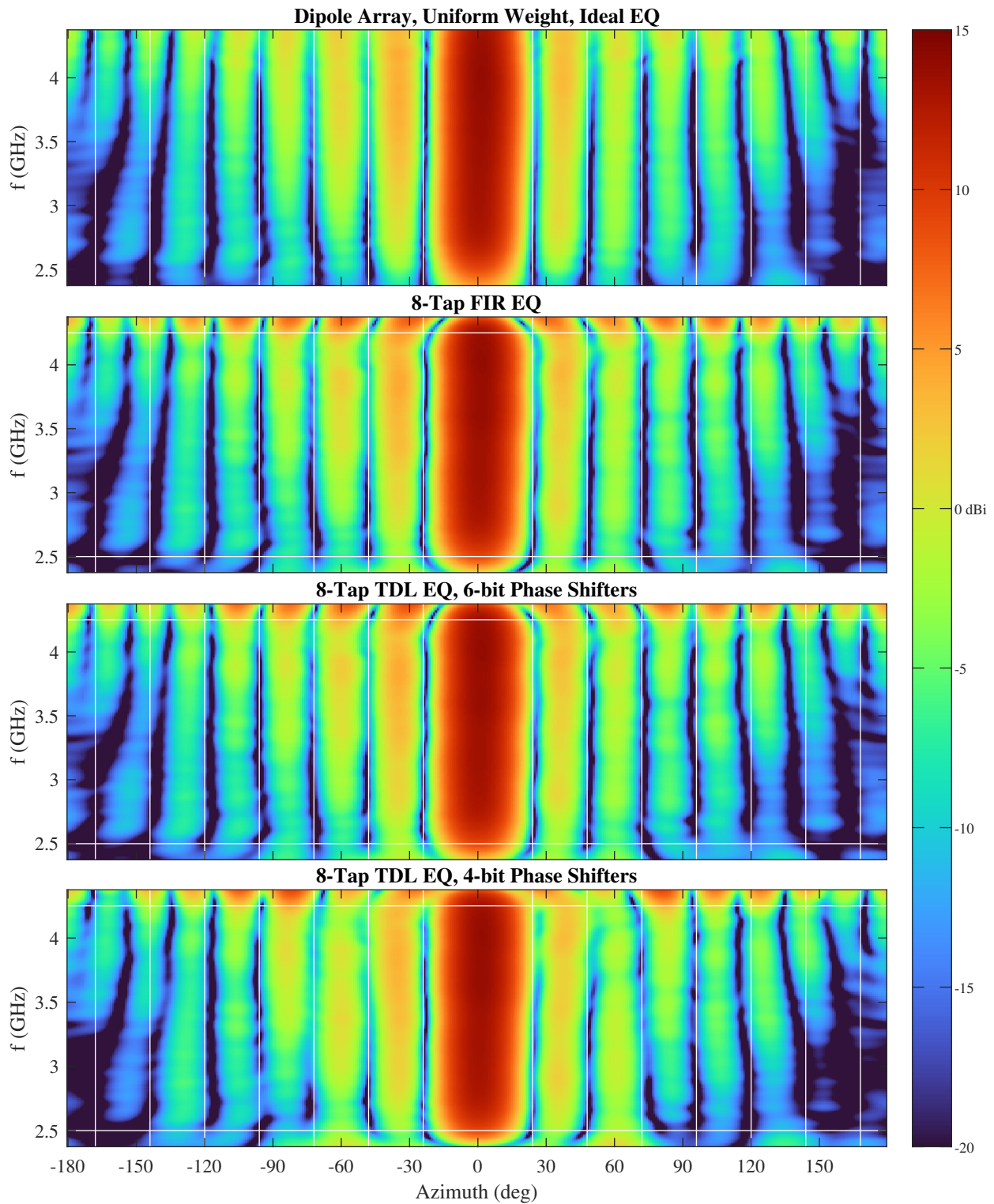
Fig. 34—A comparison of beamforming with the dipole array using a uniform taper on modes −7, … , 7 with different equalization filters. The patterns are evaluated at the horizon ($\theta = 0°$) and are normalized to show narrowband gain. The FIR and TDL equalizers were optimized between 2.5–4.25 GHz.

Notch Array, Uniform Weight, Ideal EQ

8-Tap FIR EQ

8-Tap TDL EQ, 6-bit Phase Shifters

8-Tap TDL EQ, 4-bit Phase Shifters
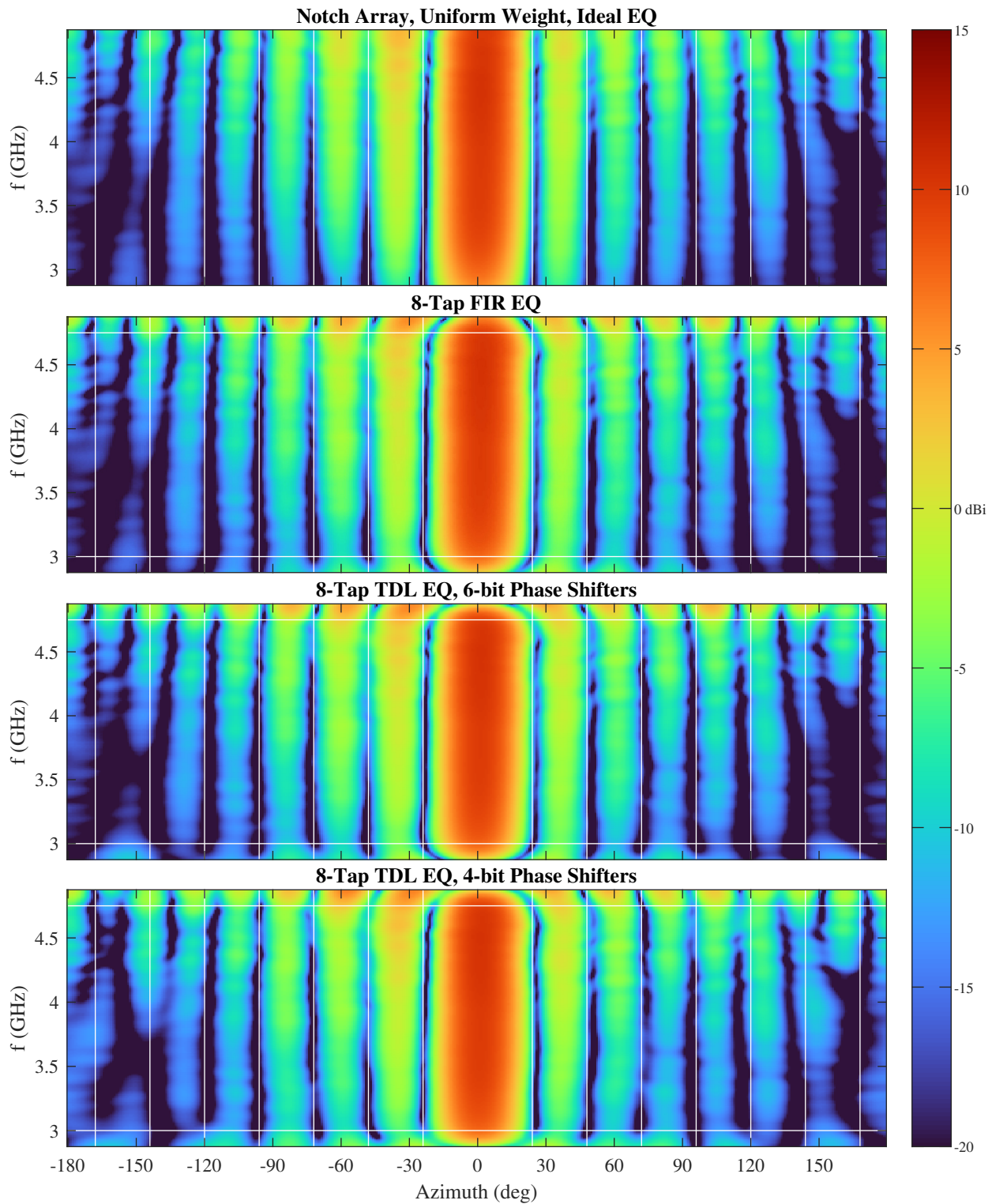
Fig. 35—A comparison of beamforming with the notch array using a uniform taper on modes $-7, \dots, 7$ with different equalization filters. The patterns are evaluated at the horizon ($\theta = 0°$) and are normalized to show narrowband gain. The FIR and TDL equalizers were optimized between 3.0–4.75 GHz.
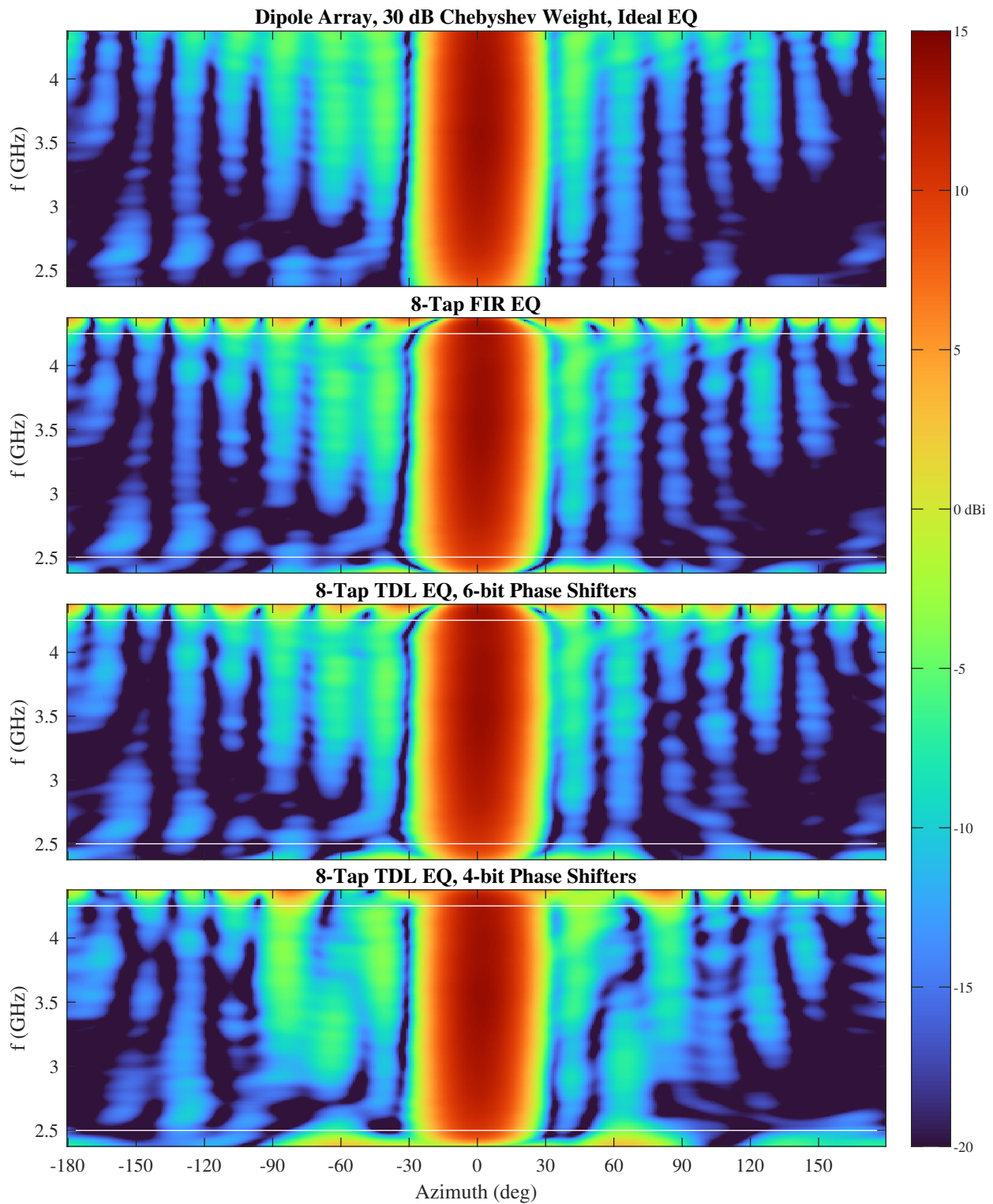
Fig. 36—A comparison of beamforming with the dipole array using a 30 dB Chebyshev taper on modes $-7, \ldots, 7$ with different equalization filters. The patterns are evaluated at the horizon ($\theta = 0°$) and are normalized to show narrowband gain. The FIR and TDL equalizers were optimized between 2.5–4.25 GHz.
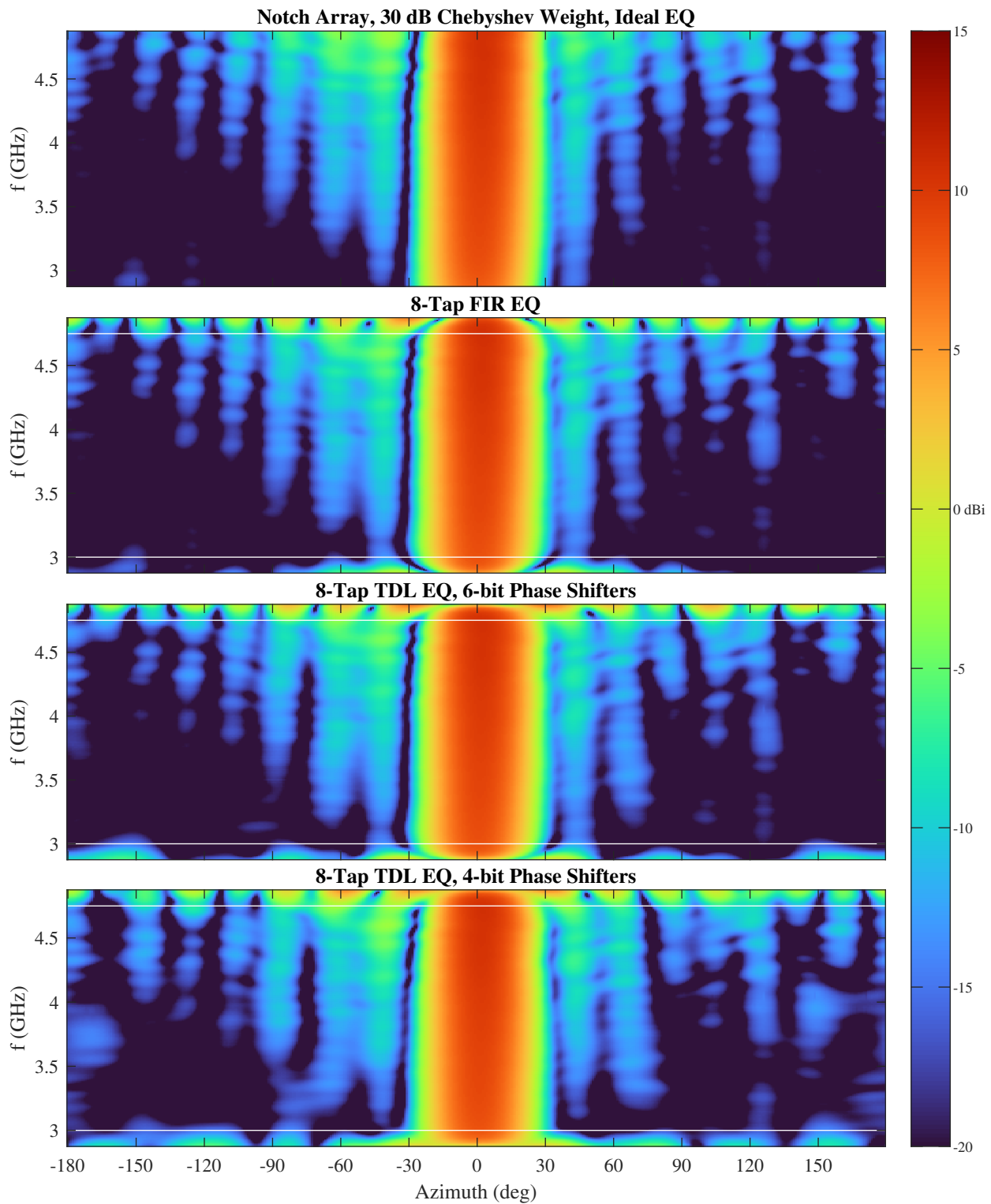
Fig. 37—A comparison of beamforming with the notch array using a 30 dB Chebyshev taper on modes −7, ... , 7 with different equalization filters. The patterns are evaluated at the horizon (θ = 0°) and are normalized to show narrowband gain. The FIR and TDL equalizers were optimized between 3.0–4.75 GHz.
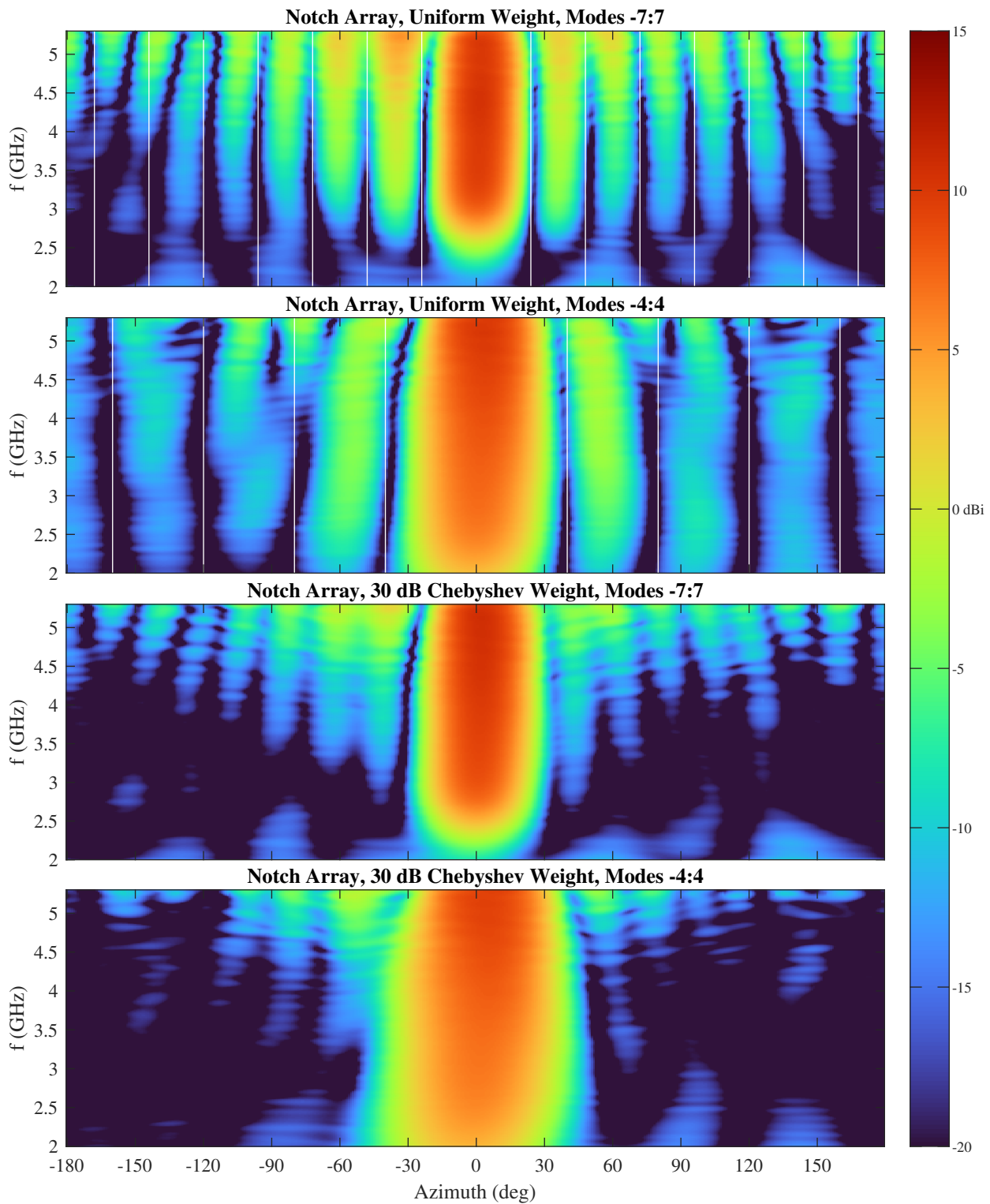
Fig. 38—A comparison of the effect that using different numbers of modes has on the azimuth and frequency response of the array pattern. At lower frequencies, the higher modes have low gain and thus the corresponding EQ filters have large noise gain. Using only lower modes improves the low-frequency gain, at the cost of increased beamwidth and reduced high-frequency gain.
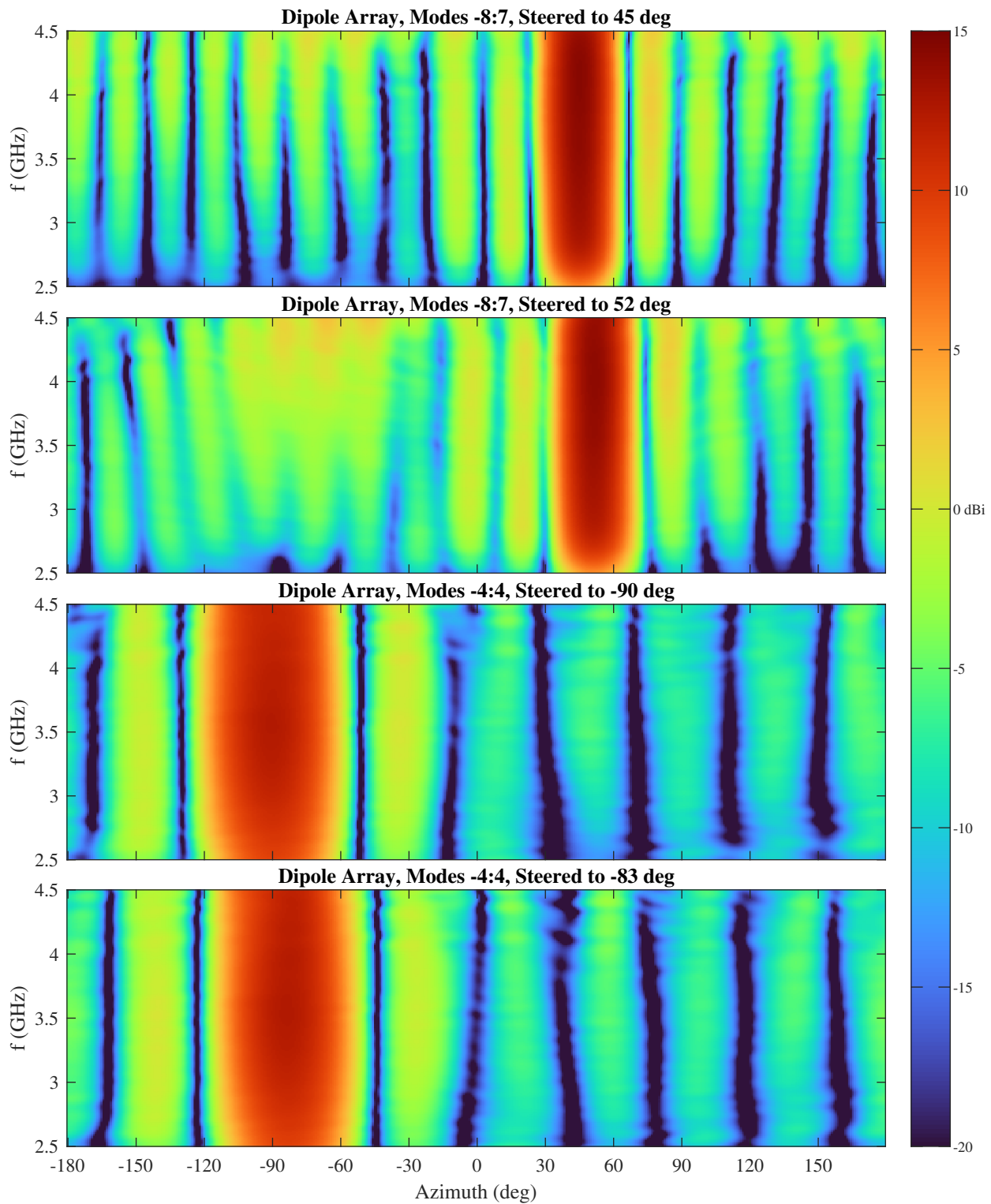
Fig. 39—The effects of phase-shift steering on the array pattern. When including all modes, as in the top two plots, steering can induce smearing in the sidelobes due to discontinuities in the distortion modes. When fewer modes are excited, as in the bottom plots, the array can be steered 360° without significant change in the pattern.
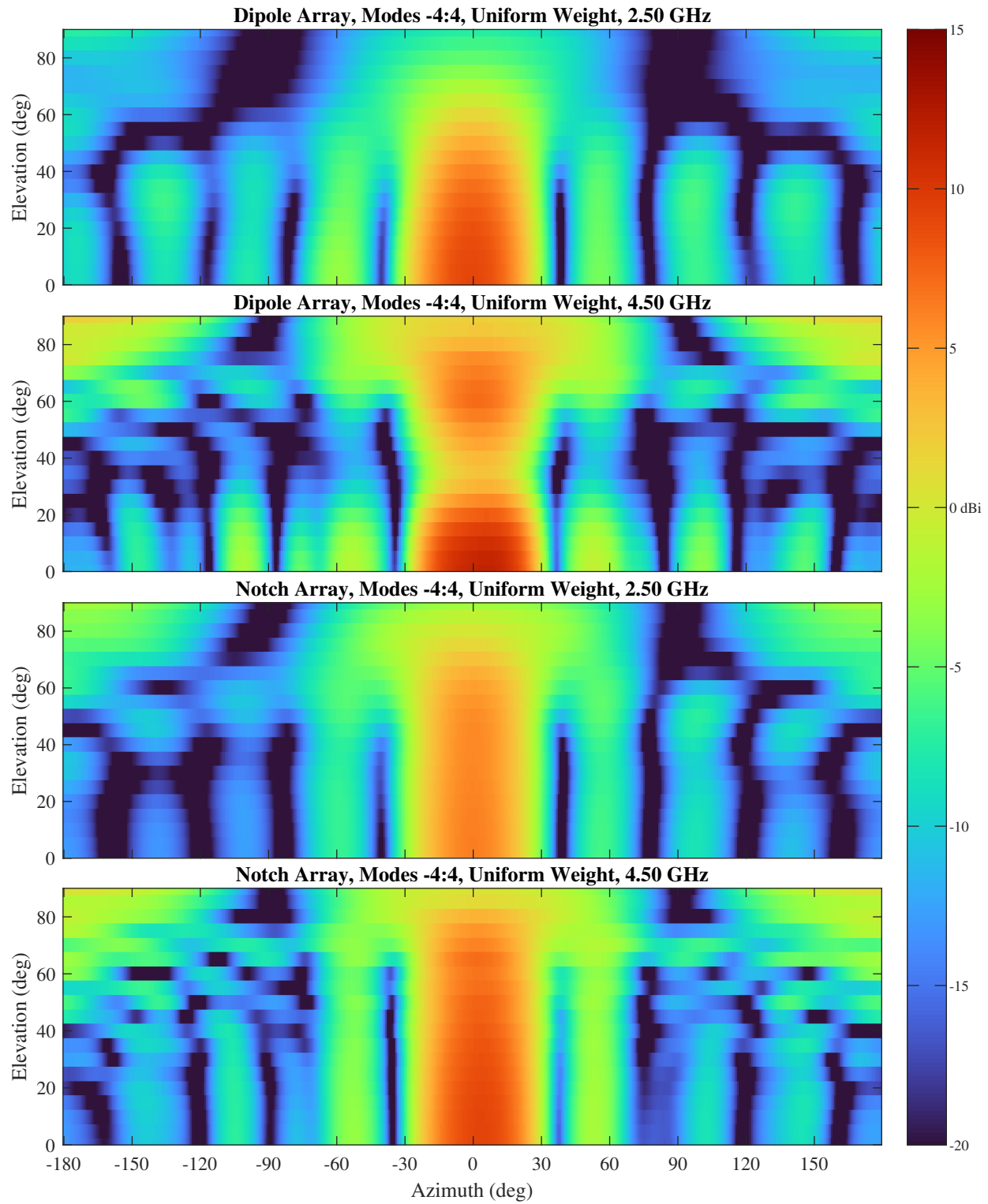
Fig. 40—A comparison of the elevation responses of the two arrays. The notch array remains approximately frequency invariant at modestly higher elevations than the dipole array, and has a somewhat broader elevation beamwidth.

where Φ_{SL} is a dense set of samples across the desired sidelobe region in azimuth and $\mathcal{F}_{\mathrm{PB}}$ is a dense set of samples across the passband region in frequency. Here δ is an auxiliary variable necessary to provide the linear objective for SOCP. The objective Eq. (48a) together with the set of SOC constraints in Eq. (48b), one per pair (ϕ_m, f_n), minimizes the peak sidelobes of the pattern. The linear constraint Eq. (48c) fixes the height of the mainlobe peak to unity at some mainbeam angle (ϕ_0, θ_0) and frequency f_0. This design is in the spirit of Chebyshev taper design, but customized to the actual patterns. Such designs tend to have equiripple sidelobes even far from the mainlobe, which can be undesireable. In order to push down the far sidelobes, we can solve the augmented problem:

$$\underset{\mathbf{w},\delta}{\text{minimize}} \quad \delta \geq 0 \tag{49a}$$

$$\text{subject to} \quad \sum_{\substack{\phi_m \in \Phi_{\mathrm{SL}} \\ f_n \in \mathcal{F}_{\mathrm{PB}}}} |A(\phi_m, \theta_0, f_n)|^2 \leq \delta^2 \tag{49b}$$

$$|A(\phi_m, \theta_0, f_n)| \leq A_{\mathrm{SLL}}, \quad \phi_m \in \Phi_{\mathrm{SL}}, f_n \in \mathcal{F}_{\mathrm{PB}} \tag{49c}$$

$$\mathrm{Re}\{A(\phi_0, \theta_0, f_0)\} \geq 1 \tag{49d}$$

where the objective Eq. (49a) together with the SOC constraint Eq. (49b) minimizes the total sidelobe energy in the array pattern at elevation θ_0. The set of SOC constraints in Eq. (49c) then constrains the peak sidelobes to some constant A_{SLL} that is somewhat higher than the minimum found by solving Eq. (48). The linear constraint Eq. (49d) again fixes the height of the pattern. This design is very much in the spirit of Taylor's line-source distribution, which has constant inner sidelobes whose level is set by a parameter with outer sidelobes that roll off further.

Applying these approaches to both arrays yields the patterns shown in Fig. 41. In both cases, the TDL equalizer responses were used, as they tend to have the largest errors and degrade the sidelobes the most. The top two plots are from the dipole array while the bottom two are from the notch array. The first of each pair was optimized according to Eq. (48), yielding a peak sidelobe level (relative to the mainlobe gain) of $-25\,$dB for the dipole array and $-23\,$dB for the notch array. The second pattern of each pair was optimized according to Eq. (49), with $A_{\mathrm{SLL}} = -20\,$dB. Visually, we can see there is a reduction in overall sidelobes between the designs, although the difference is fairly modest, as the lower sidelobes here are largely dominated by frequency-dependent hardware errors for which the narrowband coefficients are unable to fully compensate. In all designs, all modes $-8, \dots, 7$ were used, the beams were steered to $-90°$ azimuth, and the sidelobe region was defined to lie outside $\pm 35°$ from mainlobe center. The sidelobe levels represent significant improvement over the Chebyshev-weight patterns in Figs. 36 and 37, which don't come close to achieving their ideal $-30\,$dB levels.

6.3   Adaptive Beamforming

An application for which the frequency-invariant property of the phase-mode beamformer is well suited is as a wideband adaptive beamformer. Element-level adaptive beamforming for most array geometries is complicated by wide bandwidths due to how the an array pattern formed with narrowband weights scales with frequency. The mainlobe and sidelobe nulls are formed at constant electrical angles, whose relationship to physical angle is frequency-dependent. This gives rise to beam "squint," where the null moves in frequency, requiring mulitple degrees of freedom to cancel a singe wideband return. With a frequency-invariant array, a single degree of freedom will suffice to null a singe source. In this section, we first review adaptive beamforming basics and apply them to our phase-mode system. We then provide some representative
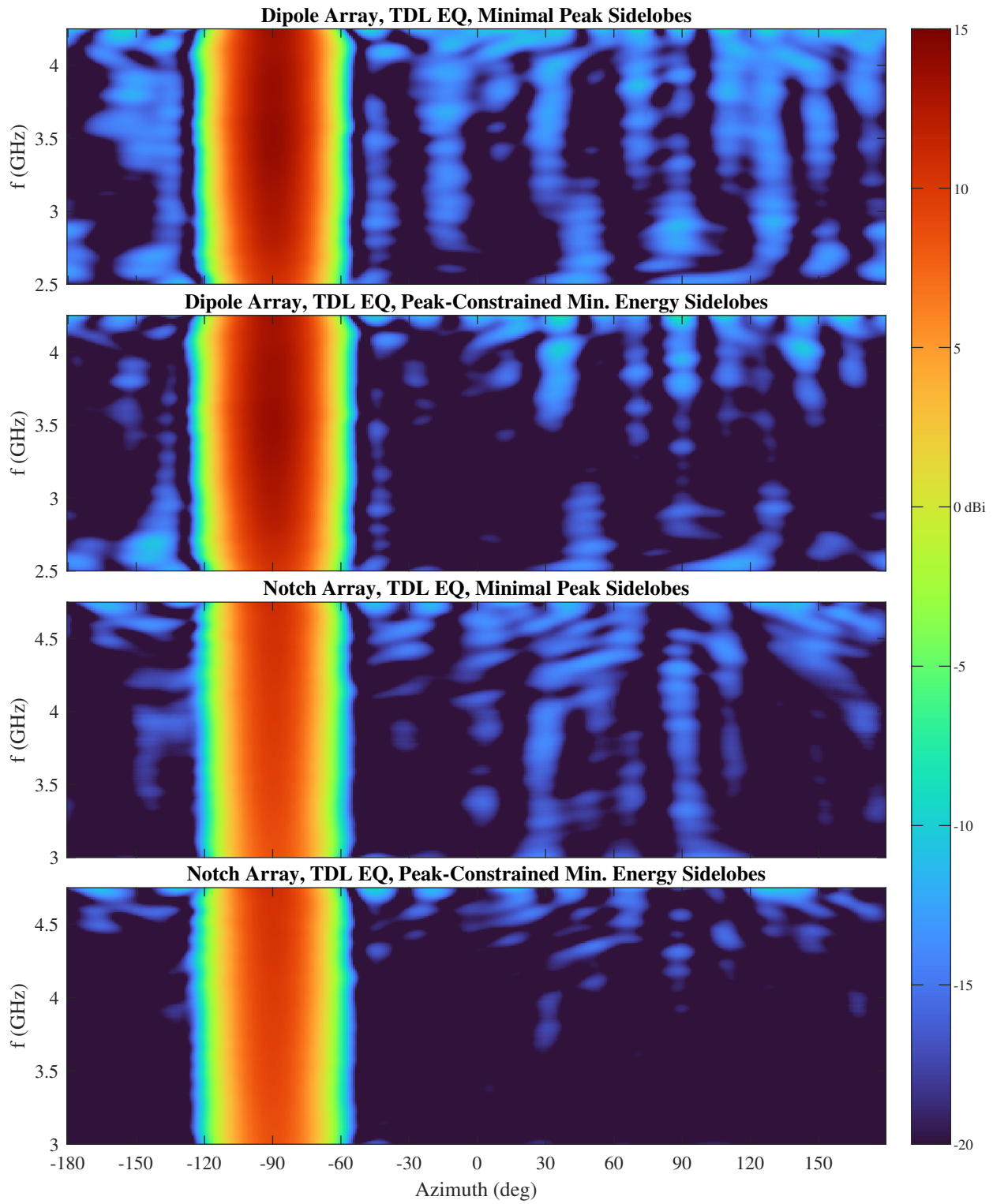
Fig. 41—A comparison of minimum-peak-sidelobe vs. peak-constrained
minimum-sidelobe-energy optimal designs for both arrays

examples to demonstrate adaptive beamforming and associated direction-of-arrival (DoA) processing using both the dipole and notch arrays. One interesting result is that, unlike a true linear array, the phase-mode virtual array can be used to estimate elevation angle as well as azimuth.

6.3.1   Adaptive Theory

To compute adaptive array patterns using the phase-mode beamformer, we must first define a model for the interference sources. Let us assume some number N_i of far-field signals at directions $\{(\phi_k, \theta_k)\}$ within the band of interest, each represented as a wide-sense stationary zero-mean random process with spectral density $S_{i,k}(f)$. We will assume that all sources are uncorrelated, and thus can be represented by a diagonal spectral sensity matrix $\mathbf{S}_i(f)$. The spectral density at the modal outputs due to these sources can be written

$$\mathbf{S}_{\text{int}}(f) = \left[\boldsymbol{v}(\phi_1, \theta_1, f), \dots, \boldsymbol{v}(\phi_{N_i}, \theta_{N_i}, f)\right] \mathbf{S}_i(f) \left[\boldsymbol{v}(\phi_1, \theta_1, f), \dots, \boldsymbol{v}(\phi_{N_i}, \theta_{N_i}, f)\right]^{\mathsf{H}}$$

$$= \sum_{k=1}^{N_i} S_{i,k}(\phi_k, \theta_k, f) \boldsymbol{v}(\phi_k, \theta_k, f) \boldsymbol{v}^{\mathsf{H}}(\phi_k, \theta_k, f),$$

where the wideband *steering vectors* $\{\boldsymbol{v}(\phi_k, \theta_k, f)\}$ are defined according to Eq. (26) as

$$\boldsymbol{v}(\phi_k, \theta_k, f) \triangleq \text{diag}\{\mathbf{H}(f)\} \mathbf{B}(f) \mathbf{Da}(\phi_k, \theta_k, f).$$

In Section 3.5, we previously derived the spectral density matrix of the receiver noise at the modal outputs as

$$\mathbf{S}_{\text{noise}}(f) = \text{diag}\{\mathbf{H}(f)\} \mathbf{B}(f) \mathbf{S_n}(f) \mathbf{B}^{\mathsf{H}}(f) \, \text{diag}\{\mathbf{H}(f)\}^{\mathsf{H}}.$$

Assuming that the noise is uncorrelated from the interference sources, the total spectral density at the beamformer output due to interference and noise is

$$S_{\text{i+n}}(f) = \mathbf{w}^{\mathsf{T}}\left(\mathbf{S}_{\text{int}}(f) + \mathbf{S}_{\text{noise}}(f)\right)\mathbf{w}^*.$$

Typically, in adaptive beaforming, the goal is to minimize the power due to residual noise and interference at the beamformer output, subject to a constraint that maintains the mainbeam gain in the steering direction. Here the noise-plus-interference output power is found by integrating the spectral density over the signal band:

$$P_{\text{i+n}} = \int_{f_1}^{f_2} S_{\text{i+n}}(f) \, \mathrm{d}f = \mathbf{w}^{\mathsf{T}}\left(\int_{f_1}^{f_2} \mathbf{S}_{\text{int}}(f) + \mathbf{S}_{\text{noise}}(f) \, \mathrm{d}f\right)\mathbf{w}^*$$

$$= \mathbf{w}^{\mathsf{T}} \mathbf{R}_{\text{i+n}} \mathbf{w}^*. \tag{50}$$

We implicitly assume that suitable filtering exists in the receiver so as to limit signal contributions from outside the RF interval $[f_1, f_2]$. Such filtering could be directly incorporated into the above expressions, but for simplicity we will assume ideal brick-wall filtering. We see in Eq. (50) that the expression for the power from our wideband array has been reduced to the standard form[5] for a narrowband array, with $\mathbf{R}_{\text{i+n}}$ playing the

---

[5]With the exception of the complex-conjugate convention on the weights, as the more-traditional form is $\mathbf{w}^{\mathsf{H}} \mathbf{R}_{\text{i+n}} \mathbf{w}$

role of the narrowband covariance matrix. If our array is exactly frequency invariant, then each interference source will appear to be from the same direction at all frequencies, and will thus contribute a single subspace to the covariance. Only a single degree of freedom would then be required to completely null out the source. Any errors such as the ones modeled that make the array pattern vary with frequency will cause a single source to "spill over" and contribute to more than one subspace. To compensate, the adaptive beamformer will require additional degrees of freedom to completely null the source, either reducing the number of sources that can be nulled or decreasing the null depth.

Having defined the interference-plus-noise power, we can design the adaptive weights **w** for a steering direction (ϕ, θ) using the classic minimum-variance distortionless response (MVDR) formulation:

$$\underset{\mathbf{w}}{\text{minimize}} \quad \mathbf{w}^{\mathsf{T}}\mathbf{R}_{\text{i+n}}\mathbf{w}^{*}$$
$$\text{subject to} \quad \mathbf{w}^{\mathsf{T}}\mathbf{v}(\phi, \theta) = 1.$$

Here $\mathbf{v}(\phi, \theta)$ is a narrowband steering vector, and the linear constraint serves to enforce a mainlobe in the direction (ϕ, θ) while the objective attempts to suppress everything else. For an ideal and perfectly equalized array using the error model of Section 3.4, the steering vector is $[\mathbf{v}(\phi, \theta_0)]_k = e^{-j2\pi m_k \phi}$ where m_k is the index of the kth mode. For elevation angles $\theta \neq \theta_0$ away from the reference elevation, the steering vector depends on the actual element modal patterns. Due to the various sources of error, the "ideal" steering vector may not match the true array manifold exactly at any frequency. An alternate approach is to use the actual value of the array manifold at some reference frequency:

$$\mathbf{v}(\phi, \theta) \triangleq \text{diag}\{\mathbf{H}(f_0)\}\mathbf{B}(f_0)\mathbf{Da}(\phi, \theta, f_0).$$

This will at least guarantee a match at a single frequency, and is the approach that will be used in the examples. The importance of the linear constraint matching the true manifold in MVDR is that errors allow the constraint to be met even while the mainbeam pattern is being partially suppressed. However the steering vector is defined, the MVDR solution is

$$\mathbf{w}_{\text{MVDR}}(\phi, \theta) = \frac{\mathbf{R}_{\text{i+n}}^{-\mathsf{T}}\mathbf{v}^{*}(\phi, \theta)}{\mathbf{v}^{\mathsf{T}}(\phi, \theta)\mathbf{R}_{\text{i+n}}^{-\mathsf{T}}\mathbf{v}^{*}(\phi, \theta)} = \frac{(\mathbf{R}_{\text{i+n}}^{-1}\mathbf{v}(\phi, \theta))^{*}}{\mathbf{v}^{\mathsf{H}}(\phi, \theta)\mathbf{R}_{\text{i+n}}^{-1}\mathbf{v}(\phi, \theta)},$$

where the second form relates the solution to the more traditional weight-conjugation convention. If we now apply the MVDR solution at each steering direction and compute the output power (variance), the result is the *MVDR spectrum*:

$$S_{\text{MVDR}}(\phi, \theta) \triangleq \mathbf{w}_{\text{MVDR}}^{\mathsf{T}}(\phi, \theta)\mathbf{R}_{\text{i+n}}\mathbf{w}_{\text{MVDR}}(\phi, \theta) = \frac{1}{\mathbf{v}^{\mathsf{H}}(\phi, \theta)\mathbf{R}_{\text{i+n}}^{-1}\mathbf{v}(\phi, \theta)}. \tag{51}$$

This provides an estimate of the power received from all directions. Because we are using narrowband array weights, we cannot estimate the power spectrum of the received signals in this way, but we can of course apply standard spectral estimation techniques to the signals captured in each steering direction.

A special case of particular interest is the no-interference case, in which we simply replace the noise-plus-interference covariance with the noise covariance:

$$\mathbf{w}_{\text{noise}}(\phi, \theta) = \frac{\left(\mathbf{R}_{\text{n}}^{-1}\mathbf{v}(\phi, \theta)\right)^*}{\mathbf{v}^{\mathsf{H}}(\phi, \theta)\mathbf{R}_{\text{n}}^{-1}\mathbf{v}(\phi, \theta)}.$$

Since this minimizes the noise power over the band of interest with a fixed pattern value, it effectively maximizes the average wideband gain of Eq. (41) over that same band. The resulting average gain is

$$G_{\mathbf{w},\text{avg}}(\phi, \theta) = \frac{1}{\mathbf{w}_{\text{noise}}^{\mathsf{T}}(\phi, \theta)\mathbf{R}_{\text{n}}\mathbf{w}_{\text{noise}}(\phi, \theta)} = \mathbf{v}^{\mathsf{H}}(\phi, \theta)\mathbf{R}_{\text{n}}^{-1}\mathbf{v}(\phi, \theta),$$

the reciprocal of the spectrum for the noise-only case. We can use this to normalize the MVDR spectrum:

$$\hat{S}_{\text{MVDR}}(\phi, \theta) \triangleq \frac{\mathbf{v}^{\mathsf{H}}(\phi, \theta)\mathbf{R}_{\text{n}}^{-1}\mathbf{v}(\phi, \theta)}{\mathbf{v}^{\mathsf{H}}(\phi, \theta)\mathbf{R}_{\text{i+n}}^{-1}\mathbf{v}(\phi, \theta)} = G_{\mathbf{w},\text{avg}}(\phi, \theta)S_{\text{MVDR}}(\phi, \theta).$$

Since the noise-only spectrum represents the ideal case, in which all interference is completely canceled, we have $1 \leq \hat{S}_{\text{MVDR}}(\phi, \theta)$ with a normalized MVDR spectrum value of unity indicating that the adaptive filter was able to eliminate the interference without raising the noise floor. Values greater than 1 represent some combination of residual interference and an increase in the noise floor due to the beamformer weights.

We can gain some important insight into the performance bounds of the MVDR beamformer by decomposing the covariance matrix. Let

$$\mathbf{R}_{\text{i+n}} = \mathbf{U}\mathbf{D}\mathbf{U}^{\mathsf{H}} = \sum_{k=1}^{K} d_k^2 \mathbf{u}_k \mathbf{u}_k^{\mathsf{H}} \tag{52}$$

be the eigenvalue (singular value) decomposition, where $\mathbf{U}$ is a unitary matrix whose columns $\{\mathbf{u}_k\}$ are the eigenvectors of $\mathbf{R}_{\text{i+n}}$ and $\mathbf{D}$ is a diagonal matrix of eigen/singular values. Let us order the diagonal entries in decreasing magnitude as $\mathbf{D}$ as $d_1^2 \geq d_2^2 \geq, \ldots, \geq d_K^2$. We can relate the singular values to the signal and noise powers in many cases. Let us first note that if $\{b_1^2, \ldots, b_K^2\}$ and $\{c_1^2, \ldots, c_K^2\}$ are the ordered singular values of $\mathbf{R}_{\text{i}}$ and $\mathbf{R}_{\text{n}}$, respectively, and the largest N_{i} singular values of $\mathbf{R}_{\text{i}}$ are much larger than the largest singular value of $\mathbf{R}_{\text{n}}$, then we have $\{d_1^2, \ldots, d_{N_{\text{i}}}^2\} \approx \{b_1^2, \ldots, b_{N_{\text{i}}}^2\}$. Now let us write the interference covariance as

$$\begin{aligned}
\mathbf{R}_{\text{i}} &= \sum_{k=1}^{N_{\text{i}}} \int_{f_1}^{f_2} S_{\text{i},k}(f)\, \boldsymbol{v}(\phi_k, \theta_k, f)\, \boldsymbol{v}^{\mathsf{H}}(\phi_k, \theta_k, f)\, \mathrm{d}f \\
&\approx \sum_{k=1}^{N_{\text{i}}} \left(\int_{f_1}^{f_2} S_{\text{i},k}(f)\, \mathrm{d}f \right) \mathbf{v}(\phi_k, \theta_k)\mathbf{v}^{\mathsf{H}}(\phi_k, \theta_k) \\
&= \sum_{k=1}^{N_{\text{i}}} P_{\text{i},k}\|\mathbf{v}(\phi_k, \theta_k)\|^2 \left(\frac{\mathbf{v}(\phi_k, \theta_k)}{\|\mathbf{v}(\phi_k, \theta_k)\|} \right) \left(\frac{\mathbf{v}(\phi_k, \theta_k)}{\|\mathbf{v}(\phi_k, \theta_k)\|} \right)^{\mathsf{H}},
\end{aligned}$$

where, in the second line, we recognize that the wideband steering vectors $\boldsymbol{v}$ have been designed to be nearly frequency invariant, and thus can be approximated by the narrowband steering vectors $\mathbf{v}$. In the third line,

the steering vectors have been normalized to unit length, and the overall sum now has a form very similar to Eq. (52). If the steering directions $\{\phi_k, \theta_k\}$ are sufficiently far apart that the steering vectors are approximately orthogonal, and we assume that the interference powers have been sorted such that $P_{i,1} \geq P_{i,2} \geq \cdots \geq P_{i,N_i}$, then we have $\{d_1^2, \ldots, d_{N_i}^2\} \approx \{P_{i,1}\|\mathbf{v}(\phi_1, \theta_1)\|^2, \ldots, P_{i,N_i}\|\mathbf{v}(\phi_{N_i}, \theta_{N_i})\|^2\}$. Thus, the largest singular values of the interference-plus-noise covariance correspond to inteference signals.

In a typical narrowband adaptive array environment, each interference source contributes at most one significant singular value, and thus, if there are fewer interference sources than elements, the remaining singular values are defined by the noise. These divide the signal space into an interference subspace and a noise subspace. For wideband arrays that are not perfectly frequency invariant, a single interference source can contribute significant energy to multiple singular values, which reduces the effective degrees of freedom in the array. Substituting Eq. (52) into Eq. (51) yields

$$S_{\mathrm{MVDR}}(\phi, \theta) = \frac{1}{\displaystyle\sum_{k=1}^{K} \frac{1}{d_k^2} |\mathbf{u}_k^H \mathbf{v}(\phi, \theta)|^2},$$

which is maximized when $\mathbf{v} = \alpha \mathbf{u}_1$ for some complex scalar α and minimized when $\mathbf{v} = \beta \mathbf{u}_K$ for some complex scalar β. Thus, we have the upper and lower bounds

$$\frac{d_K^2}{\|\mathbf{v}(\phi, \theta)\|^2} \leq S_{\mathrm{MVDR}}(\phi, \theta) \leq \frac{d_1^2}{\|\mathbf{v}(\phi, \theta)\|^2} \approx P_{i,1}.$$

The upper bound can be approached when the steering direction (ϕ, θ) coincides with the largest interference source; here the distortionless-response linear constraint makes it impossible for the beamformer to significantly reduce the power from that source. The lower bound is approached when the steering direction is sufficiently far from any interference sources that it lies in the noise subspace. As more interference sources are added and the more their energy spreads to multiple singular values, the smaller the dimension of the noise subspace and the less likely that any given steering vector lies within it. With enough sources and spreading, eventually the noise subspace is dominated by the interference subspace, and the lower bound is controlled entirely by the interference. A similar analysis can be used to augment the previous unity lower bound on the normalized MVDR spectrum as well:

$$\max\left\{1, \frac{d_K^2}{c_1^2}\right\} \leq \hat{S}_{\mathrm{MVDR}}(\phi, \theta) \leq P_{i,1} G_{\mathbf{w},\mathrm{avg}}(\phi, \theta).$$

This reinforces the concept that once the smallest noise-plus-interference eigenvalue d_k^2 exceeds the largest noise-only eigenvalue c_1^2, then the interference has dominated the noise subspace and complete cancellation is not possible. In many cases, the noise eigenvalue spread is minimal, such that $c_1^2 \approx c_K^2 \approx \tilde{c}^2$ and

$$G_{\mathbf{w},\mathrm{avg}}(\phi, \theta) = \mathbf{v}^H(\phi, \theta) \mathbf{R}_n^{-1} \mathbf{v}(\phi, \theta) \approx \|\mathbf{v}(\phi, \theta)\|^2 / \tilde{c}^2,$$

indicating the noise is spatially white.

Instead of normalizing to the noise response, one can also normalize the MVDR spectrum to that of some reference antenna so that the normalized spectrum now indicates some notion of cancellation ratio or improvement factor. It is not entirely obvious what the best reference is, however. One might use a single mode from the phase-mode beamformer, as it is omnidirectional in azimuth. However, the different modes can have significantly different elevation profiles, so choosing any particular mode can introduce a bias. We will sidestep this issue here and simply use the noise-normalized MVDR spectrum as our primary metric. The cancellation ratio at any given angle can be inferred as the distance from the upper bound.

6.3.2   *Adaptive Examples*

In this section, we will apply the results from the previous section to explore the performance of our phase-mode beamformer as a wideband adaptive beamformer. We will consider various combinations of the number of interference sources, the bandwidth and center frequency of those sources, and the power of the sources, and compare representative adaptive beam patterns and the normalized MVDR spectrum which results from applying beams adapted for all azimuth and elevation directions. To simplify the examples, we will assume that all interference sources are uncorrelated, have rectangular spectra, and are defined by three parameters: their center frequency, their bandwidth, and their interference-to-noise ratio (INR), which is the ratio of the interference power incident at the array per mode to the noise power per mode. All covariance matrices will be computed per Eq. (50) using the known system responses and wideband steering vectors simulated for each array. For both the dipole and notch arrays, we will use TDL filter responses optimized per Section 5.4 with 6-bit phase shifters for equalization. For the dipole array, we will define the passband to be the interval $[2.5\,\text{GHz}, 4.25\,\text{GHz}]$, and for the notch array, we will limit our examples to the band $[3.0\,\text{GHz}, 4.75\,\text{GHz}]$. Adaptive array patterns will be optimized using MVDR, and the normalized MVDR spectrum will be computed over a 360° azimuth range with 0.5° steps and elevation from the horizon (0°) up to zenith (90°) with 1° steps.

We will first look at the behavior of the array in the presence of a single interference source at band center with a very large INR of 60 dB as we vary the bandwidth from 10 MHz, which is the frequency resolution of the simulated data, up to the full equalized bandwidth of 1.75 MHz. Figure 42 compares the singular values $\{d_k^2\}$ of $\mathbf{R}_{\text{i+n}}$ for the noise-only and single-interference cases across bandwidth. We can see that the noise singular values $\{c_k^2\}$ are nearly constant at around -3 dB, with the only exceptions being the three largest ones. These outliers correspond to modes -8, -7, and 7 and are the result of excessive noise gain in the EQ filters at low frequencies. When we add a single 10 MHz interference source, we see the first singular value is now determined by that source, but because this represents only a single frequency point, the interference source is effectively narrowband and contributes to no other singular values. As we increase the bandwidth, however, the lone interference source starts to dominate more singular values until at around 640 MHz where even the smallest singular value starts to rise above the noise floor. Effectively, a wideband source looks like a single strong narrowband source plus a number of smaller narrowband sources. When the interference is very strong, as it is here, even a single source can exhaust the available degrees of freedom.

We can see this bandwidth effect more directly in the plots of Figs. 43 and 44, which compare adaptive results for a low- and high-bandwidth interference for the dipole and notch arrays, respectively. The top plot in each figure shows the adapted pattern at the horizon for a beam steered to $(\phi, el) = (0°, 0°)$ in the presence of a single strong interference at the horizon with a bandwidth of 160 MHz. The location and spectral width of the interference is indicated by the dotted magenta line, at $\phi = 45°$ in this case. In each case, there is a mainlobe at center and a deep null where the signal lies, as we would expect. The second plot shows the normalized MVDR spectrum that results from applying similarly optimized beams at each azimuth and elevation location.
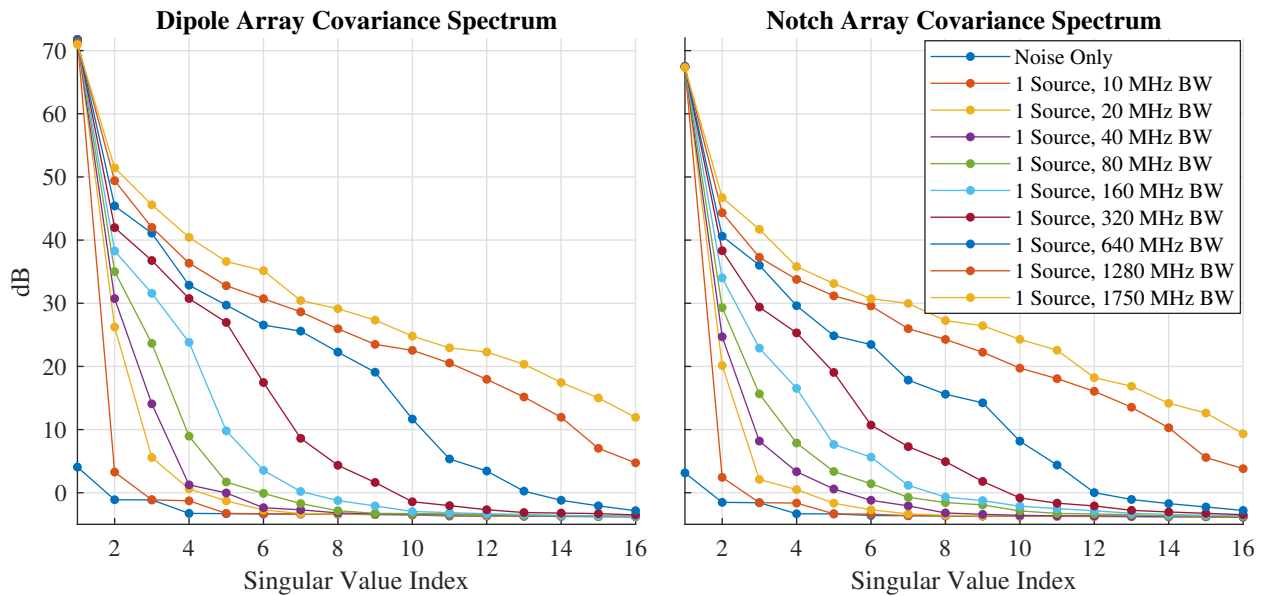
Fig. 42—A comparison of the singular values of the interference-plus-noise covariance matrix for the dipole and notch arrays with a single strong interference of varying bandwidth

Here the direction of the interference is indicated by the magenta circle. Near the location of the interference, the MVDR spectrum grows large, which can be interpreted in two different ways. If we think of the MVDR spectrum as the residual error power (noise plus interference) for beams centered in each direction, we see that the MVDR constraint prevents a null in the center of the mainlobe, and thus cancellation close to the interference is not possible. This is inevitable with any adaptive beamformer. Alternatively, if we view the MVDR spectrum as a direction-of-arrival (DoA) estimate, then the peak in the spectrum provides an estimate of the direction and power of the interference source. In either case, the width of the region of increased power is much narrower than the natural (Fourier) resolution of the array, as MVDR is a superresolution technique. Away from he interference source, the MVDR spectrum has a value very close to 0 dB, which indicates that the interference was canceled nearly completely with minimal increase in the noise gain over the noise-only case. Thus, for a single narrowband interference, we have nearly optimal performance.

The bottom two plots in Figs. 43 and 44 repeat the experiment with a full interference bandwidth of 1750 MHz. Here we can see several significant differences with the narrower-bandwidth case. The MVDR spectrum floor is significantly elevated, indicating significant residual interference-plus-noise power after beamforming. The adapted mainlobes for the representative patterns are somewhat distorted with reduced gain, the sidelobes are higher, and the width of the MVDR-spectrum peak is greater, yielding poorer DoA resolution. All of this is a result of the combination of high power and wide bandwidth consuming all of the degrees of freedom of the array. Comparing the two arrays, we see similar performance in terms of the MVDR spectrum, with the dipole performing slightly better for the narrow bandwidth and the notch array performing slightly better for the wide bandwidth. Their respective patterns are significantly different, in particular for the wideband case, which is presumably due to differences in the distortion modes between the arrays.

Having looked at the performance with one very strong interference, we now look at the performance with multiple interference sources of more modest power at the horizon. Figures 45 and 46 show representative

Fig. 43—Adaptive array patterns and normalized MVDR spectra for the dipole array in the presense of noise and a single strong interference source. In the top two plots, the interference has a modest bandwidth, while in the bottom two plots, the interference occupies the entire equalized band. The magenta, dotted lines and circles indicate the direction and spectral extent of the interference.
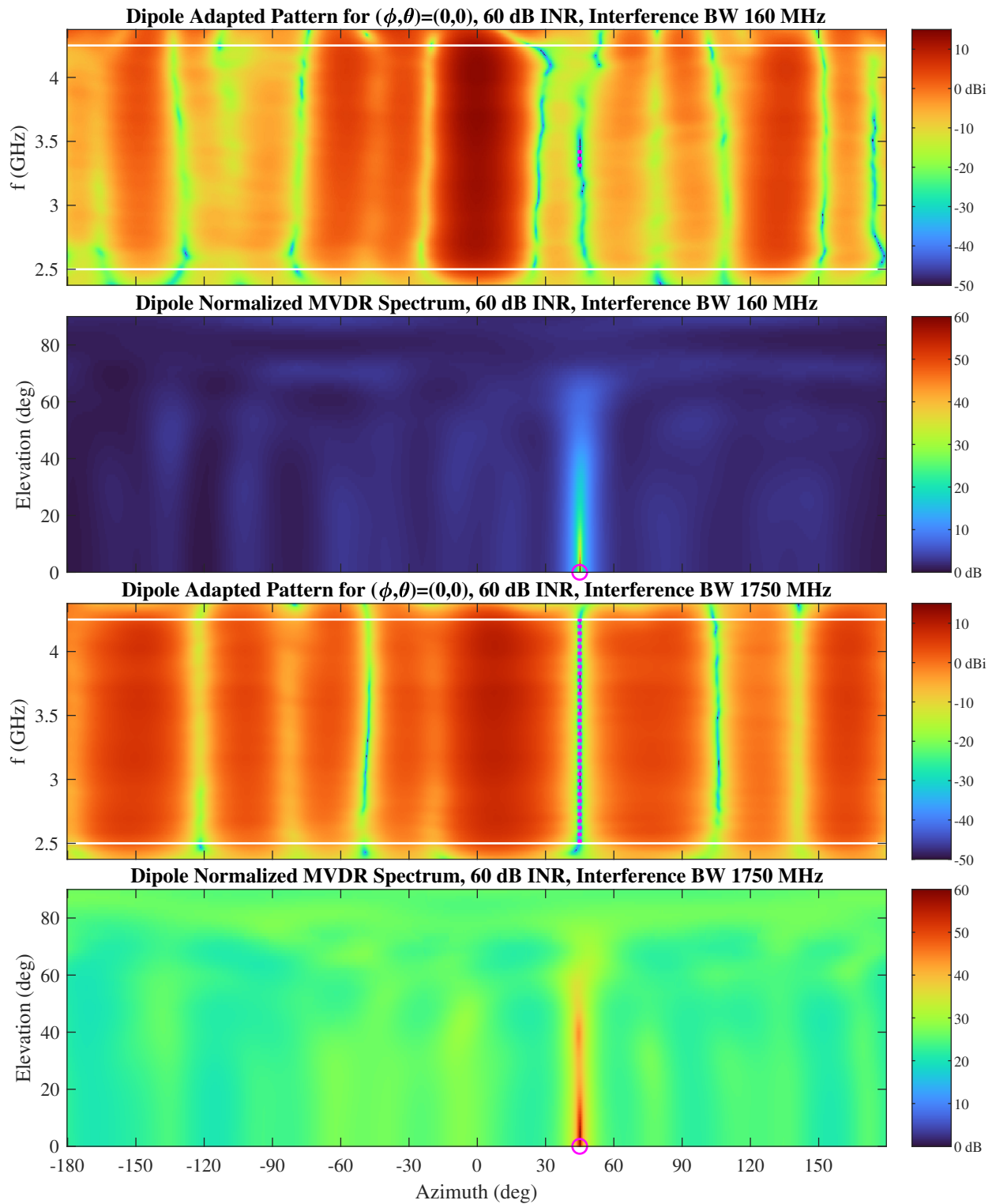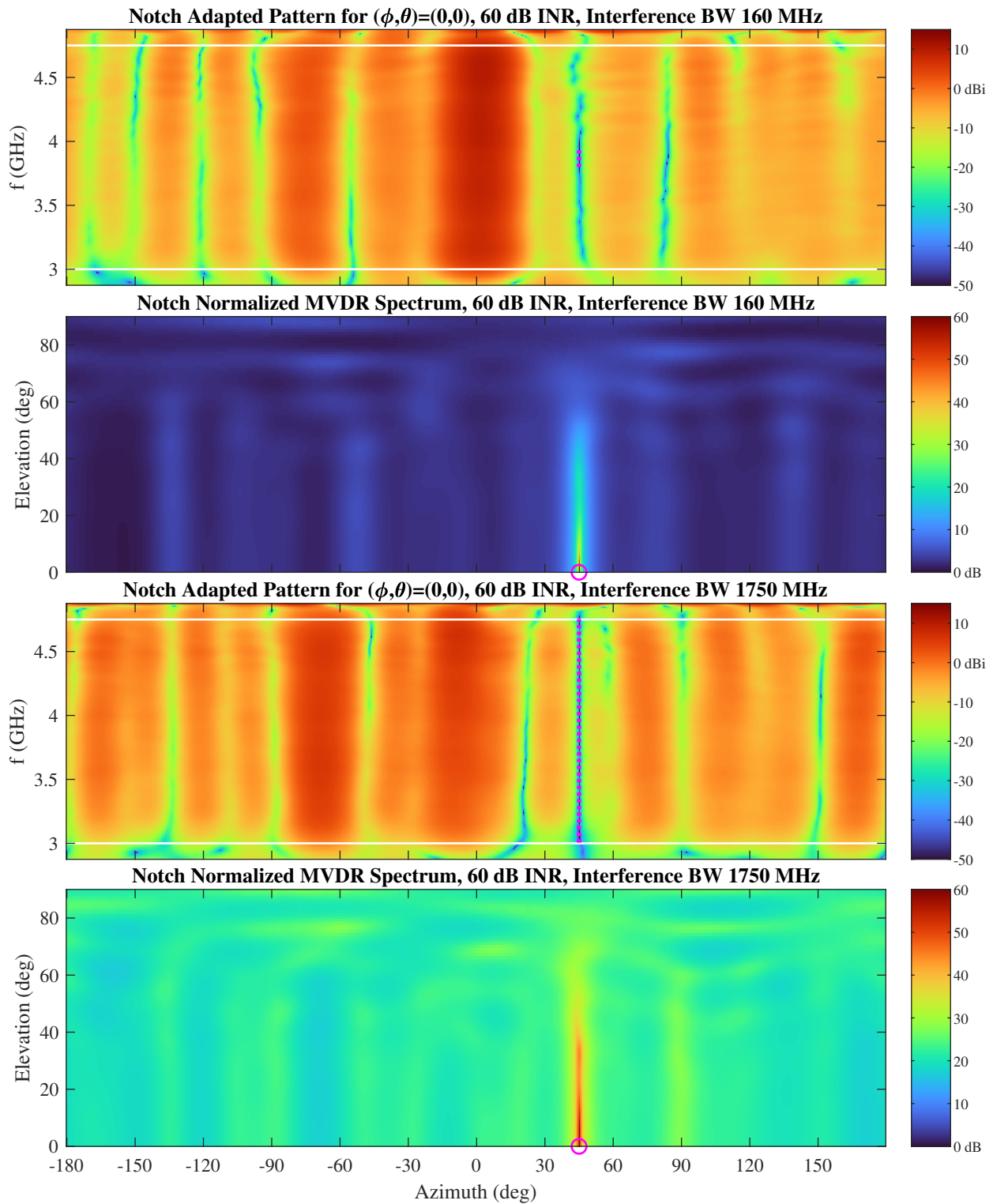
Fig. 44—Adaptive array patterns and normalized MVDR spectra for the notch array in the presense of noise and a single strong interference source. In the top two plots, the interference has a modest bandwidth, while in the bottom two plots, the interference occupies the entire equalized band.

adapted patterns and normalized MVDR spectra for the cases of four (top two plots) and eight (bottom two plots) interference sources with an INR of 30 dB for each array. The sources have varying center frequencies and bandwidths within the overall array operating band. For the four-source case, we can see the expected deep pattern notches at the source locations, and the corresponding peaks in the MVDR spectra. The interference-plus-noise floor in the MVDR spectra indicates good cancellation performance. The bottom two plots in each figure show an additional four interference sources, for a total of eight. All eight again receive nulls, although they are not quite as coherent or deep, and all eight sources are visible in the MVDR spectra. Comparing the arrays, the notch array appears to have slightly better overall cancellation performance.

A notable effect seen in the MVDR spectra is that the power levels of sources that are offset from the center of the band are underestimated. In particular, this is seen in the source at 150° azimuth in both cases and the source at −175° for the eight-interference case. This is a result of a mismatch between the true wideband steering vector seen by the signal as it passes through the array and beamformer and the narrowband steering vector (which is based on the overall center frequency) used in the MVDR processing. Because the linear constraint does not quite correctly fix the beam pattern at offset frequencies, the MVDR objective is able to cancel some of the interference power even in the direction of the interference. Besides the negative effects on the spectral and DoA estimation, this can also be an issue when desired signals are present and are incorporated into the covariance matrix, as it leads to self cancellation. Such effects in the presence of manifold errors (of various sources) are a well-known artifact from MVDR. In this case, the problem could be mitigated by using narrowband steering vectors tuned to the actual center frequency of the expected signals.

The total number of interference sources that the adaptive beamformer is effectively able to cancel depends on a combination of source power and bandwidth. Figures 47 and 48 explore the case of a large number of sources with modest bandwidths. Here the top two plots result from twelve interference sources on the horizon with bandwidths of only 10 MHz, while the bottom plots increase the bandwidths to 200 MHz. Here the results generally follow from the previous examples, which looked at bandwidth and the number of sources independently. Comparing the two arrays, we see that the large number of sources has caused there to be much less variation in the pattern shapes between the arrays. As in the previous examples, the notch array appears to have a lower interference-plus-noise floor for the higher-bandwidth case. Self-cancellation effects are again seen for the sources with offset center frequencies, although the severity decreases with increasing source bandwidth as the mismatch error is averaged over the wider band.

We can see for these narrower interference bandwidths that the sidelobes of the adaptive patterns are not particularly frequency invariant despite our best efforts in the system design. While this might seem like a flaw, in fact it shows the adaptive beamformer optimally using the actual degrees of freedom at hand. If we were to ignore the true array manifold and instead to optimize an idealized one, we would get theoretical frequency-invariant patterns that would then perform poorly once the actual hardware responses were included. The real power of an approximately frequency-invariant array comes when wideband interferences are present, and there we do see the invariant behavior.

In all of the examples to this point, the interference sources were placed along the horizon. This is a typical arrangement for a linear array, which has no independent pattern control in the elevation direction, and the analysis of the phase-mode beamformer was largely focused on its approximation of a virtual linear array. However, that analysis was largely confined to the single reference elevation at which the equalization filters were designed, and the phase modes have differing elevation profiles (as seen in Figs. 12 and 18) which could potentially be exploited. This is because fundamentally, a circular array is a two-dimensional array, albeit a sparse one, unlike a physical linear array. There is dependence across azimuth and elevation due to

Dipole Adapted Pattern for $(\phi,\theta)=(0,0)$, 4 Interferers, 30 dB INR

Dipole Normalized MVDR Spectrum, 4 Interferers, 30 dB INR

Dipole Adapted Pattern for $(\phi,\theta)=(0,0)$, 8 Interferers, 30 dB INR

Dipole Normalized MVDR Spectrum, 8 Interferers, 30 dB INR

Fig. 45—Adaptive array patterns and normalized MVDR spectra for the dipole array in the presence of noise and multiple interference sources. In the top two plots, four interference sources are present, versus eight in the bottom two plots.

Fig. 46—Adaptive array patterns and normalized MVDR spectra for the notch array in the presense of noise and multiple interference sources. In the top two plots, four interference sources are present, versus eight in the bottom two plots.

Fig. 47—Adaptive array patterns and normalized MVDR spectra for the dipole array in the presense of noise and 12 interference sources. In the top two plots, the interference bandwidth is 10 MHz, versus 200 MHz in the bottom two plots.
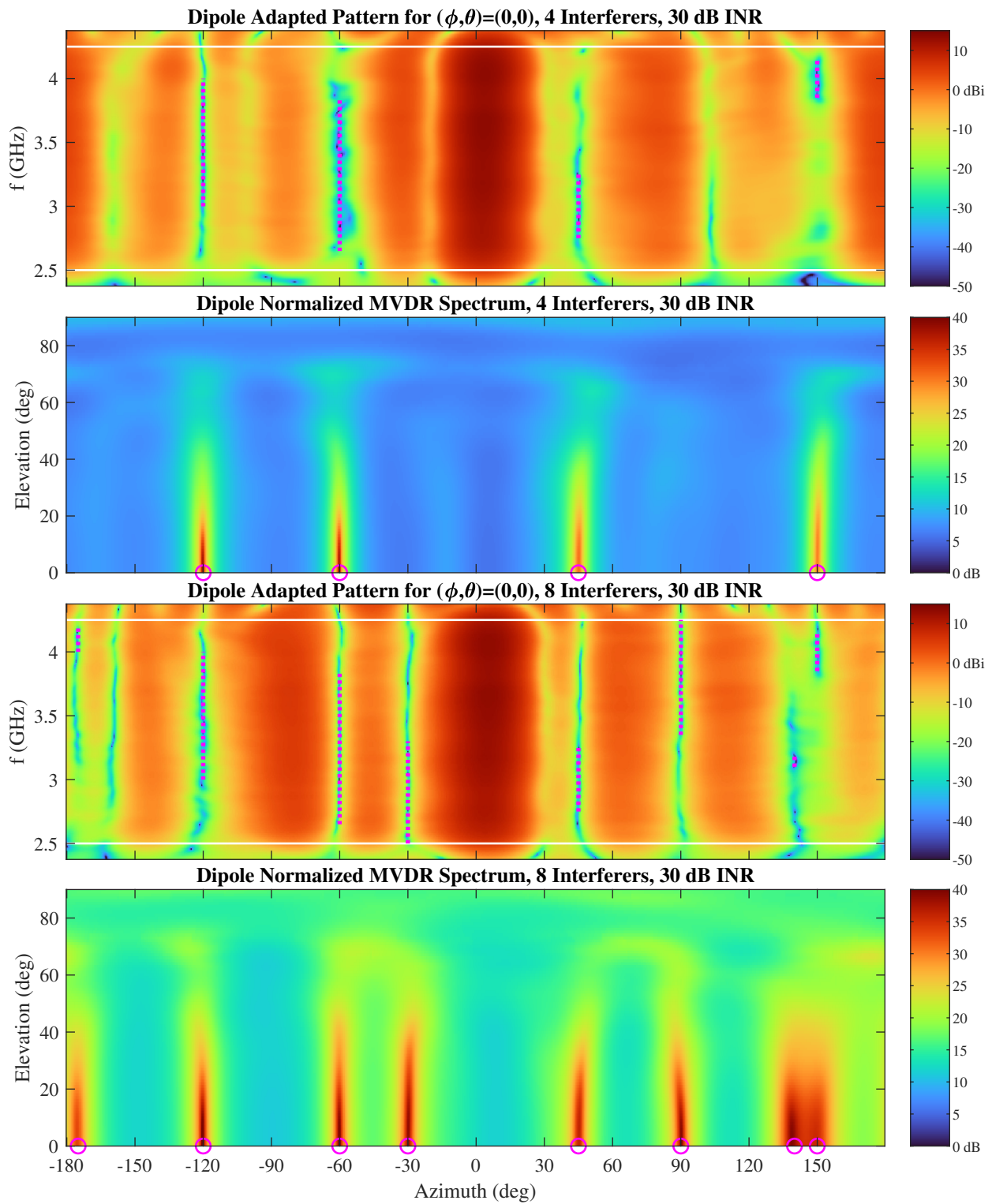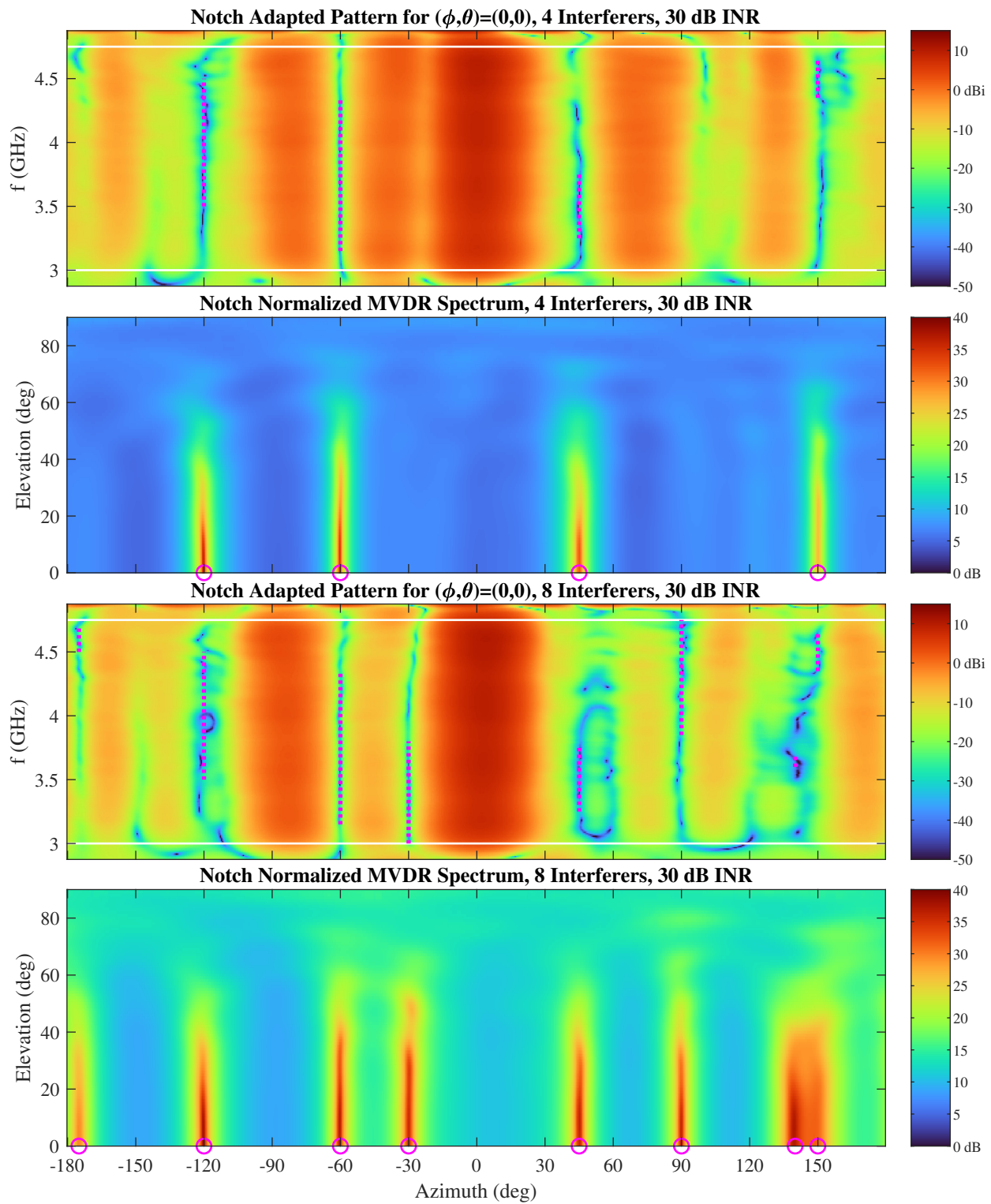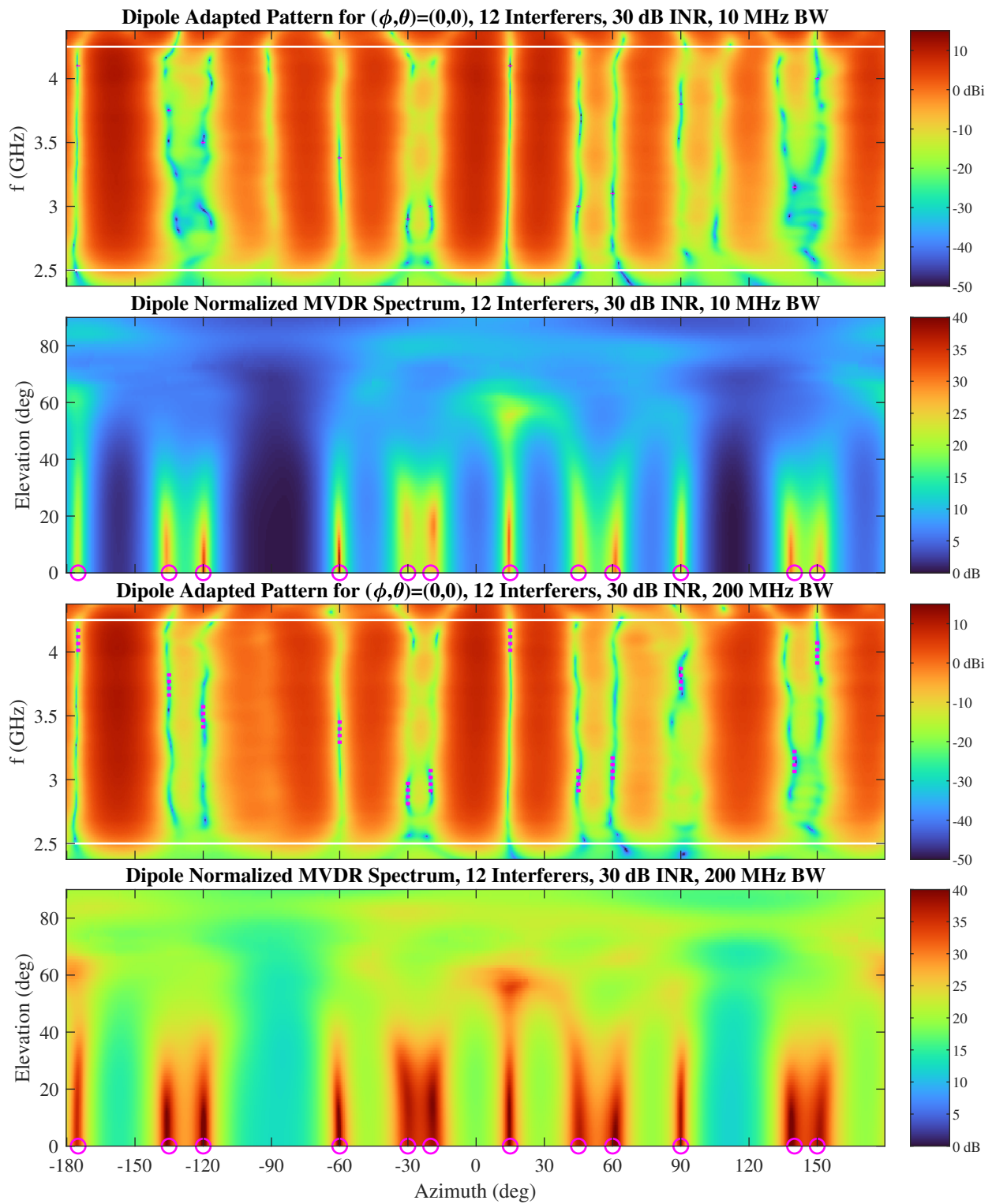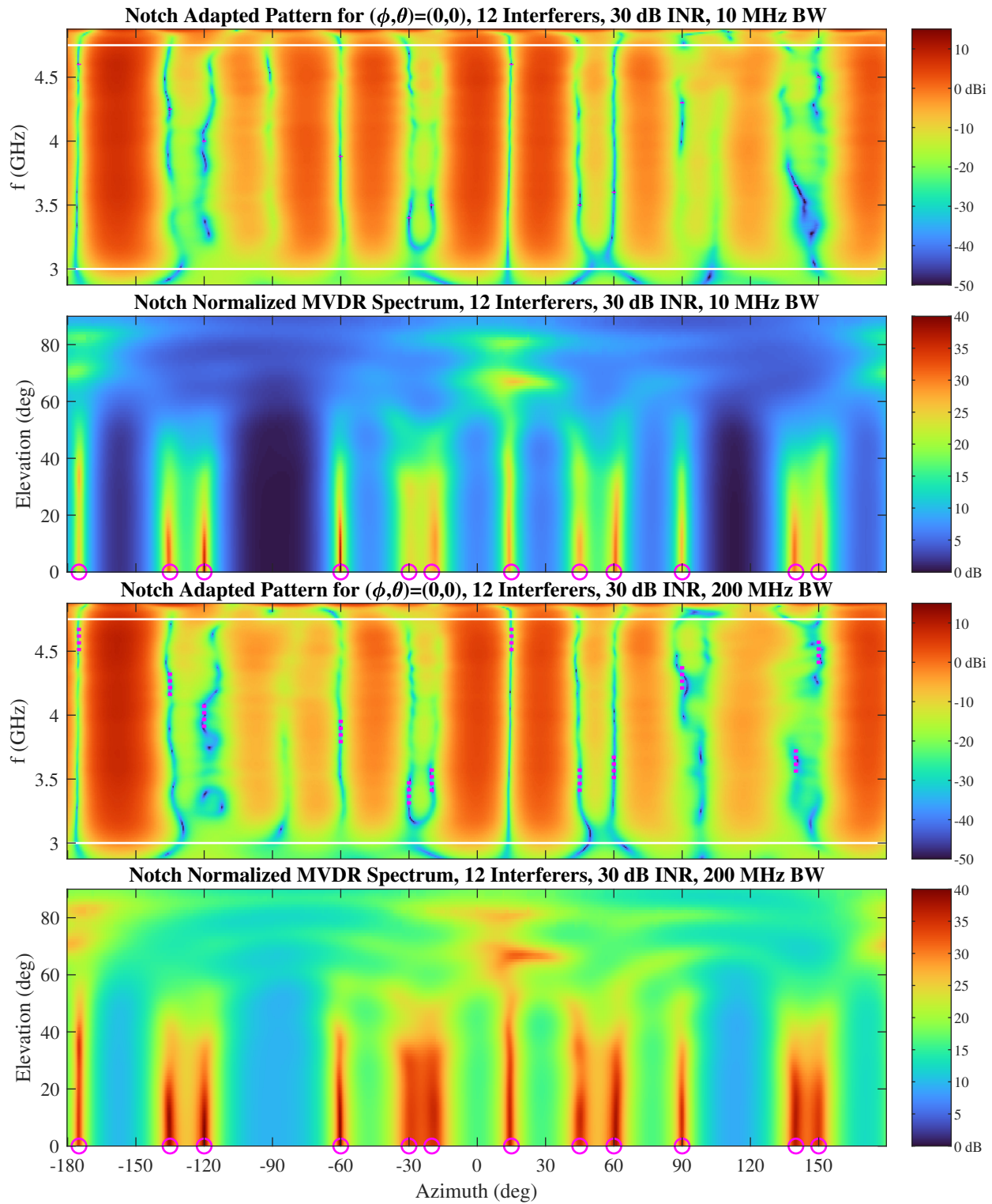
Fig. 48—Adaptive array patterns and normalized MVDR spectra for the notch array in the presense of noise and 12 interference sources. In the top two plots, the interference bandwidth is 10 MHz, versus 200 MHz in the bottom two plots.

the array's regular and sparse structure (like grating lobes, but more complicated) and thus all combinations of sources cannot necessarily be well separated even when sufficient degrees of freedom appear to exist. But it is inherently more capable in this sense than a linear array.

The elevation capability of the phase-mode beamformer is explored in Figs. 49 and 50, which show the responses of each array to five interference sources of varying elevation. Here the top three plots in each figure show azimuth-elevation slices of the adapted pattern at three frequencies within the band, while the fourth plot shows the normalized MVDR spectrum. The circles within each pattern plot show the locations of sources whose spectral support includes the frequency of that slice, while the MVDR spectrum shows all five source locations as before. We can see that we do get nulls in the direction of each interference, including the interference at $(\phi, \theta) = (0°, 75°)$ which is in the same azimuth direction as the mainlobe. This demonstrates that we do have at least some independent control over the pattern in azimuth and elevation. Looking at the MVDR spectrum, we see that at the horizon, the array has good azimuth resolution but very poor elevation resolution, which is a result of the approximately linear geometry of the array when viewed edge-on. However, at higher elevations the elevation resolution improves significantly as the projected view of the array becomes an ellipse and we essentially have an interferometer between the near and far edges of the ellipse. Near zenith, the azimuth resolution degrades, although this is primarily an artifact of the polar geometry. We do see strong self-cancellation effects here, due again to frequency-offset-induced manifold mismatch, which seemingly worsen at higher elevations. This is in part due to the low gain of many of the phase modes at high elevation, particularly for the dipole array. Indeed, comparing the two MVDR spectra shows that the dipole array provides much weaker estimates of the higher-elevation sources than the notch array. This is consistent with the previous comparison of the elevation responses of the arrays in Fig. 40, which showed that the notch pattern was significantly broader in elevation.

Fig. 49—Results of adaptive beamforming with the dipole array with targets above the horizon. The top three plots show a representative adapted pattern at three different frequencies, while the bottom plot shows the corresponding normalized MVDR spectrum. The circles indicate the locations of targets.
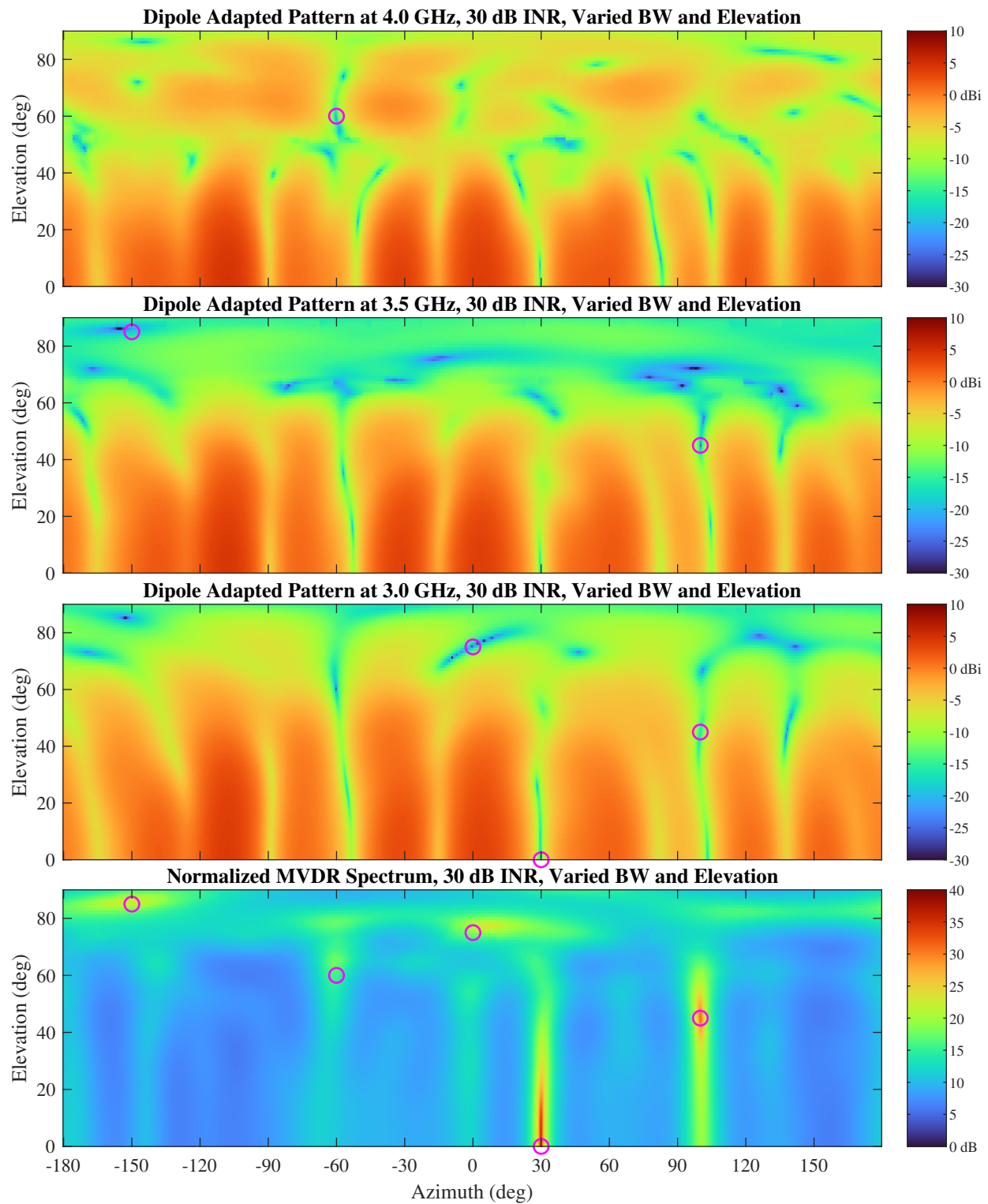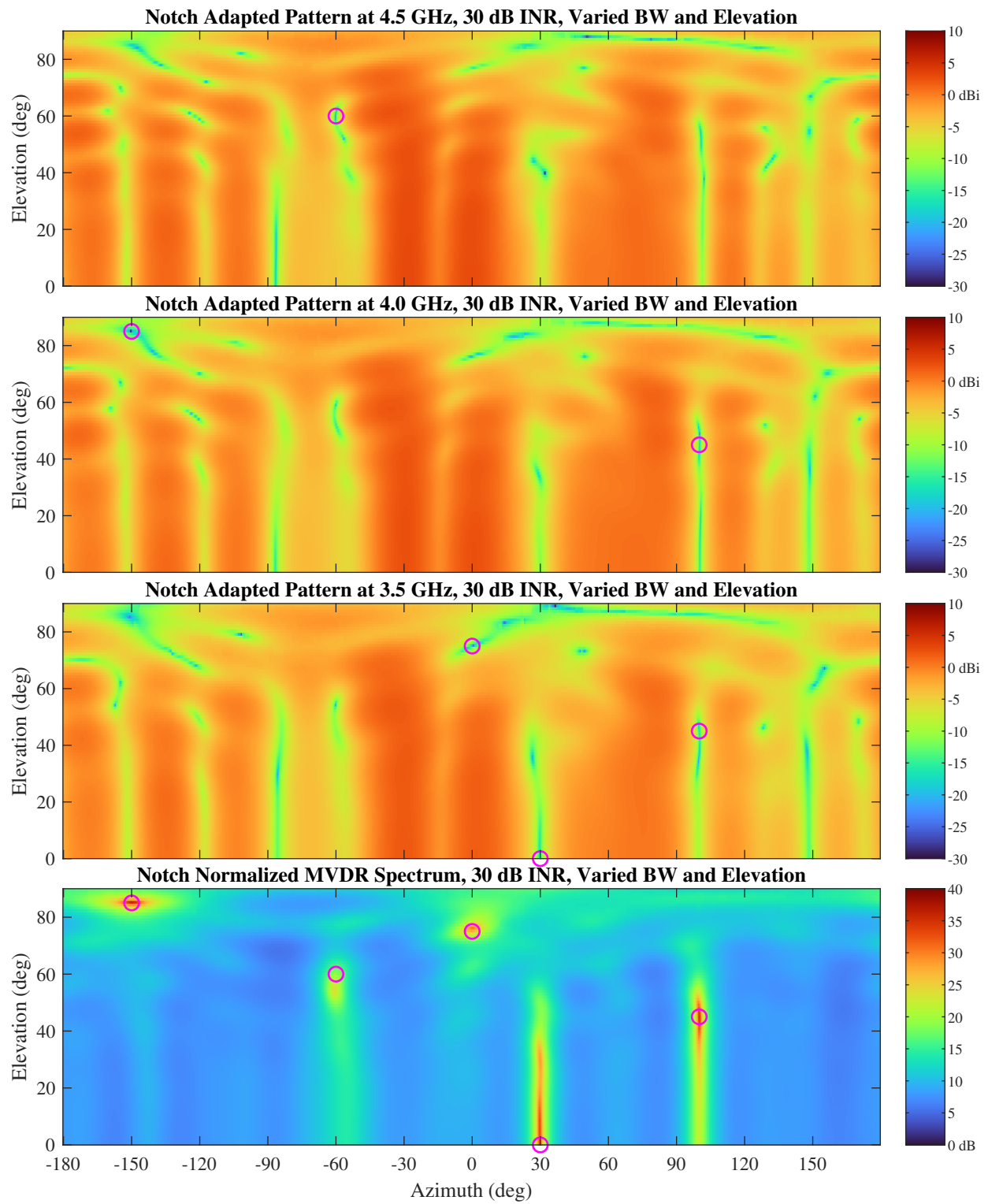
Fig. 50—Results of adaptive beamforming with the notch array with targets above the horizon. The top three plots show a representative adapted pattern at three different frequencies, while the bottom plot shows the corresponding normalized MVDR spectrum. The circles indicate the locations of targets.

7. CONCLUSION

The goal of this project was to perform a proof-of-concept design of a phase-mode beamformer, including the array, Butler-matrix-based modal beamformer, equalization, and virtual-array combining of the modes. The hardware design aspects are amply documented in prior reports. This report serves to analyze and simulate the end-to-end system, to model the various sources of error, to develop design techniques for the required equalization of the modes, and to demonstrate the wideband performance of the array. Notable contributions include:

1. A comprehensive error analysis and error model for the system, defining errors due to distortion modes in the array, nonideal responses in the Butler matrix, and residual errors in the equalization filters. By itemizing the errors in this way, it is made apparent which component is the limiting factor and which requires more attention to improve overall system performance. Here it was shown that the Butler matrix was the primary source of error, with the array distortion modes being significant in certain cases. The equalization is generally capable of lower errors, and can be further improved from what was shown here by adding additional taps and/or reducing the instantaneous bandwidth.

2. Optimization-based approaches to equalization filter design, including both digital FIR filters and analog TDL filters. Algorithms were developed to integrate the hardware responses and the attenuator and phase-shifter quantization into the design of TDL filters. These approaches are more generally applicable to TDL filters for other applications as well, such as programmable bandpass filters.

3. Using the prior system model, the hardware developed on this project was analyzed to show the error contributions.

4. FIR and TDL equalization filters were computed using the optimization algorithms previously described, integrating a commercial attenuator and various commercial phase shifters. The relative performance was compared, and some insight is shown into the progression of the steps of the TDL optimization algorithm.

5. The wideband frequency-invariant performance of the array using standard narrowband array tapers is demonstrated, both in terms of null locations and sidelobe depth.

6. Optimal deterministic array patterns were computed using narrowband weights, and it was shown that peak and mean-square sidelobes could be further improved over standard tapers, partially compensating for hardware errors.

7. Adaptive wideband beamforming performance of each array was demonstrated, varying the number, strength, and direction of interference sources. It was shown that the effect of hardware errors was to spread a single wideband interference source across multiple degrees of freedom, such that fewer sources could be nulled than in an ideal array, and that this effect grows with signal bandwidth. It was also shown that the array could be used for wideband direction-of-arrival processing, and that it had the ability to null and locate sources in elevation, a unique capability not available in true linear arrays.

Overall, this project and report should provide anyone looking to implement a phase-mode beamformer in the future a solid foundation of theory and a significant head start in terms of analysis and design.

REFERENCES

1. G. Trunk and D. Patel, "Optimal number of phased array faces and signal processors for horizon surveillance," *IEEE Transactions on Aerospace and Electronic Systems* **33**(3), 1002–1006 (July 1997), ISSN 2371-9877, doi:10.1109/7.599324.

2. G. Trunk, "Optimal number of phased array faces for horizon and volume surveillance revisited," Proceedings of the IEEE International Symposium on Phased Array Systems and Technology, Oct. 2003, pp. 124–129. doi:10.1109/PAST.2003.1256968.

3. D. E. N. Davies, "Circular Arrays," in *Handbook of Antenna Design*, volume 2, chapter 12 (IET Digital Library, Jan. 1983).

4. L. Josefsson and P. Persson, *Conformal array antenna theory and design*, volume 29 (John Wiley & Sons, 2006).

5. W. M. Dorsey and D. P. Scholnik, "Transmit and receive circular array pattern synthesis for radar applications," Proceedings of the 2016 IEEE Radar Conference, Philadelphia, PA, May 2016, pp. 1–6. doi:10.1109/RADAR.2016.7485277.

6. W. Dorsey, R. Mital, and D. Scholnik, "Phase-Only Synthesis of Omnidirectional Patterns with Multiple Nulls from a Uniform Circular Array," Proceedings of the IEEE Int'l Symp. Ant. and Prop., Fajardo, PR, 2016.

7. M. Galletti, D. Zrnic, G. Zhang, D. Doviak, and J. Crain, "CPPAR - cylindrical polarimetric phased array radar system design," Proceedings of the Proc. IEEE Radar Conference, May 2011, pp. 033–038. doi:10.1109/RADAR.2011.5960494.

8. G. Zhang, S. Karimkashi, L. Lei, R. Kelley, J. Meier, R. Palmer, C. Futon, R. J. Doviak, A. Zahrai, D. S. Zrnic, and Y. Al-Rashid, "A cylindrical polarimetric phased array radar concept — A path to multi-mission capability," Proceedings of the IEEE International Symposium on Phased Array Systems and Technology, Oct. 2013, pp. 481–484. doi:10.1109/ARRAY.2013.6731875.

9. Y. Wu and H. C. So, "Simple and Accurate Two-Dimensional Angle Estimation for a Single Source With Uniform Circular Array," *IEEE Antennas and Wireless Propagation Letters* **7**, 78–80 (2008), ISSN 1548-5757, doi:10.1109/LAWP.2008.916687.

10. T. J. Jung and K. Lee, "Closed-Form Algorithm for 3-D Single-Source Localization With Uniform Circular Array," *IEEE Antennas and Wireless Propagation Letters* **13**, 1096–1099 (2014), ISSN 1548-5757, doi:10.1109/LAWP.2014.2327992.

11. W. M. Dorsey, A. Stumme, K. M. Charipar, and N. A. Charipar, "3-D-Printed Circular Array for WiMAX Base Station," *IEEE Antennas and Wireless Propagation Letters* **18**(6), 1159–1163 (June 2019), ISSN 1548-5757, doi:10.1109/LAWP.2019.2911354.

12. A. Chepala, H. Tataria, and V. Fusco, "Beamspace Modulated Circular Array," *IEEE Transactions on Antennas and Propagation* **67**(5), 3496–3499 (May 2019), ISSN 1558-2221, doi:10.1109/TAP.2019.2901092.

13. D. Scholnik and J. Coleman, "Optimal Array-Pattern Synthesis for Wideband Digital Transmit Arrays," *IEEE Journal of Selected Topics in Signal Processing* **1**(4), 660–677 (2007).

14. S. M. Mohammadi, L. K. S. Daldorff, J. E. S. Bergman, R. L. Karlsson, B. Thide, K. Forozesh, T. D. Carozzi, and B. Isham, "Orbital Angular Momentum in Radio—A System Study," *IEEE Transactions on Antennas and Propagation* **58**(2), 565–572 (Feb. 2010), ISSN 1558-2221, doi:10.1109/TAP.2009.2037701.

15. Y. Yao, X. Liang, W. Zhu, J. Geng, and R. Jin, "Phase Mode Analysis of Radio Beams Carrying Orbital Angular Momentum," *IEEE Antennas and Wireless Propagation Letters* **16**, 1127–1130 (2017), ISSN 1548-5757, doi:10.1109/LAWP.2016.2623808.

16. F. Tamburini, E. Mari, A. Sponselli, B. Thidé, A. Bianchini, and F. Romanato, "Encoding many channels on the same frequency through radio vorticity: first experimental test," *New Journal of Physics* **14**(3), 033001 (Mar. 2012), ISSN 1367-2630, doi:10.1088/1367-2630/14/3/033001.

17. O. Edfors and A. J. Johansson, "Is Orbital Angular Momentum (OAM) Based Radio Communication an Unexploited Area?," *IEEE Transactions on Antennas and Propagation* **60**(2), 1126–1131 (Feb. 2012), ISSN 1558-2221, doi:10.1109/TAP.2011.2173142.

18. M. Tamagnone, C. Craeye, and J. Perruisseau-Carrier, "Comment on 'Encoding many channels on the same frequency through radio vorticity: first experimental test'," *New Journal of Physics* **14**(11), 118001 (Nov. 2012), ISSN 1367-2630, doi:10.1088/1367-2630/14/11/118001.

19. M. Tamagnone, C. Craeye, and J. Perruisseau-Carrier, "Comment on 'Reply to Comment on "Encoding many channels on the same frequency through radio vorticity: first experimental test" '," *New Journal of Physics* **15**(7), 078001 (July 2013), ISSN 1367-2630, doi:10.1088/1367-2630/15/7/078001.

20. F. Tamburini, B. Thidé, E. Mari, A. Sponselli, A. Bianchini, and F. Romanato, "Reply to Comment on 'Encoding many channels on the same frequency through radio vorticity: first experimental test'," *New Journal of Physics* **14**(11), 118002 (Nov. 2012), ISSN 1367-2630, doi:10.1088/1367-2630/14/11/118002.

21. L. B. Kish and R. D. Nevels, "Twisted Radio Waves and Twisted Thermodynamics," *PLOS ONE* **8**(2), e56086 (Feb. 2013), ISSN 1932-6203, doi:10.1371/journal.pone.0056086.

22. A. F. Morabito, L. Di Donato, and T. Isernia, "Orbital Angular Momentum Antennas: Understanding Actual Possibilities Through the Aperture Antennas Theory," *IEEE Antennas and Propagation Magazine* **60**(2), 59–67 (Apr. 2018), ISSN 1558-4143, doi:10.1109/MAP.2018.2796445.

23. D. K. Nguyen, O. Pascal, J. Sokoloff, A. Chabory, B. Palacin, and N. Capet, "Antenna gain and link budget for waves carrying orbital angular momentum," *Radio Science* **50**(11), 1165–1175 (2015), ISSN 1944-799X, doi:10.1002/2015RS005772.

24. Y. Zhang, W. Feng, and N. Ge, "On the restriction of utilizing orbital angular momentum in radio communications," Proceedings of the 8th International Conference on Communications and Networking in China, Aug. 2013, pp. 271–275. doi:10.1109/ChinaCom.2013.6694604.

25. K. Liu, Y. Cheng, X. Li, and Y. Gao, "Microwave-Sensing Technology Using Orbital Angular Momentum: Overview of Its Advantages," *IEEE Vehicular Technology Magazine* **14**(2), 112–118 (June 2019), ISSN 1556-6080, doi:10.1109/MVT.2018.2890673.

26. S. Zheng, Y. Chen, Z. Zhang, X. Jin, H. Chi, X. Zhang, and Z. N. Chen, "Realization of Beam Steering Based on Plane Spiral Orbital Angular Momentum Wave," *IEEE Transactions on Antennas and Propagation* **66**(3), 1352–1358 (Mar. 2018), ISSN 1558-2221, doi:10.1109/TAP.2017.2786297.

27. B. Sheleg, "A matrix-fed circular array for continuous scanning," *Proceedings of the IEEE* **56**(11), 2016–2027 (Nov. 1968), ISSN 0018-9219, doi:10.1109/PROC.1968.6778.

28. J. O. Coleman and W. M. Dorsey, "Phase-shift steer a uniform circular array in the Fourier-series domain," Proceedings of the 2017 IEEE 18th Wireless and Microwave Technology Conference (WAMICON), Apr. 2017, pp. 1–4.

29. W. Dorsey, J. Coleman, and W. Pickles, "Uniform circular array pattern synthesis using second-order cone programming," *IET Trans. on Microwaves, Antennas Propagation* **9**(8), 723–727 (2015), ISSN 1751-8725, doi:10.1049/iet-map.2014.0418.

30. W. M. Dorsey, G. C. Tavik, and K. Williams, "Ultrawideband Circular Array with Pattern Versatility," NRL Memo Report MR/5310–13-9460, Naval Research Laboratory, Washington DC, USA, Mar. 22, 2013.

31. R. Mital, M. P. Parent, and A. Stumme, "Circular Array Beamforming Using Phase Modes," Memorandum Report NRL/MR/5317–19-9908, US Naval Research Laboratory, Washington, DC, Dec. 2019.

32. R. Mital, W. R. Pickles, and M. G. Parent, "Design and Development of Butler Matrices for Circular Array Beamforming," Memorandum Report NRL/MR/5317–20-10,130, US Naval Research Laboratory, Washington, DC, Sept. 2020.

33. R. Mital and W. R. Pickles, "Final Report on Modal Beamformers using Passive Butler Matrices," Memorandum Report NRL/IR/5317–21-13-U, US Naval Research Laboratory, Washington, DC, Dec. 2021. in review.

34. D. P. Scholnik, *Shared Wideband Transmit Antenna Arrays: Optimal Pattern Synthesis and Spatio-Temporal Delta-Sigma Modulation*, Ph.D thesis. (University of Maryland, Baltimore County, Baltimore, MD, Jan. 2006).

35. D. P. Scholnik, "A Parameterized Pattern-Error Objective for Large-Scale Phase-Only Array Pattern Design," *IEEE Transactions on Antennas and Propagation* **64**(1), 89–98 (Jan. 2016).

36. R. C. Jones, "New Calculus for the Treatment of Optical Systems," *J. Opt. Soc. Amer.* **31**, 488–493 (1941).

37. M. Neiman, "The Principle of Reciprocity in Antenna Theory," *Proceedings of the IRE* **31**(12), 666–671 (Dec. 1943), ISSN 2162-6634.

38. R. F. Harrington and W. R. Lepage, "Directional Antenna Arrays of Elements Circularly Disposed About a Cylindrical Reflector," *Proceedings of the IRE* **40**(1), 83–86 (Jan. 1952), ISSN 2162-6634, doi:10.1109/JRPROC.1952.273940.

39. T. Taylor, "A synthesis method for circular and cylindrical antennas composed of discrete elements," *Transactions of the IRE Professional Group on Antennas and Propagation* **PGAP-3**, 251–261 (Aug. 1952), ISSN 2168-0647, doi:10.1109/T-AP.1952.28047.

40. C. E. Hickman, H. P. Neff, and J. D. Tillman, "The theory of a single-ring circular antenna array," *Transactions of the American Institute of Electrical Engineers, Part I: Communication and Electronics* **80**(2), 110–115 (May 1961), ISSN 2379-674X, doi:10.1109/TCE.1961.6373084.

41. D. E. N. Davies, "A transformation between the phasing techniques required for linear and circular aerial arrays," *Proceedings of the Institution of Electrical Engineers* **112**(11), 2041–2045 (Nov. 1965), ISSN 0020-3270, doi:10.1049/piee.1965.0340.

42. I. Longstaff, P. Chow, and D. Davies, "Directional properties of circular arrays," *Proceedings of the Institution of Electrical Engineers* **114**(6), 713–718 (June 1967), ISSN 0020-3270, doi:10.1049/piee.1967.0142.

43. T. Rahim, *Directional pattern synthesis in circular arrays of directional antennas*, Doctoral (University of London, 1980). URL `https://discovery.ucl.ac.uk/id/eprint/1317595/`.

44. T. Rahim and D. Davies, "Effect of directional elements on the directional response of circular antenna arrays," *IEE Proceedings H - Microwaves, Optics and Antennas* **129**(1), 18–22 (Feb. 1982), ISSN 0143-7097, doi:10.1049/ip-h-1.1982.0004.

45. S. C. Chan and C. K. S. Pun, "On the design of digital broadband beamformer for uniform circular array with frequency invariant characteristics," Proceedings of the Proc. IEEE Int'l Symposium on Circuits and Systems, volume 1, May 2002.

46. H. Steyskal, "Digital Beamforming Aspects of Wideband Circular Arrays," Proceedings of the IEEE Aerospace Conference, March 2008, pp. 1–6. doi:10.1109/AERO.2008.4526316.

47. M. Lobo, L. Vandenberghe, S. Boyd, and H. Lebret, "Applications of second-order cone programming," *Linear Algebr. Applicat.* **248**, 193–228 (Nov. 1998).

48. J. O. Coleman and D. P. Scholnik, "Design of nonlinear-phase FIR filters with second-order cone programming," Proceedings of the Proc. IEEE 42nd Midwest Symp. on Circuits and Systems, volume 1, Las Cruces, NM, USA, Aug. 1999, pp. 409–412.

49. J. O. Coleman, D. P. Scholnik, and P. E. Cahill, "Synthesis of a polarization-controlled pattern for a wideband array by solving a second-order cone program," Proceedings of the Proc. IEEE Int. Symp. on Antennas and Propag., volume 2B, 2005, pp. 437–440. doi:10.1109/APS.2005.1552039.

50. J. F. Sturm, "Using SeDuMi 1.02, a Matlab Toolbox for Optimization over Symmetric Cones," *Optimization methods and software* **11–12**, 625–653 (versions 1.02/1.03) (1999). updated in 2001 for version 1.05.

51. K. C. Toh, M. J. Todd, and R. H. Tütüncü, "SDPT3 version 4.0—a MATLAB software for semidefinite-quadratic-linear programming," July 2006. URL `http://www.math.nus.edu.sg/~mattohkc/sdpt3.html`.

52. A. Domahidi, E. Chu, and S. Boyd, "ECOS: An SOCP solver for embedded systems," *European Control Converence* (2013). URL `http://www.stanford.edu/~boyd/papers/pdf/ecos_ecc.pdf`.

53. R. J. Vanderbei and H. Yurttan, "Using LOQO to solve second-order cone programming problems," *Constraints* **1** (1998). URL `http://www.academia.edu/download/30589187/socp.pdf`.

54. J. Coleman, D. Scholnik, and J. Brandriss, "A specification language for the optimal design of exotic FIR filters with second-order cone programs," Proceedings of the Signals, Systems and Computers, 2002. Conference Record of the Thirty-Sixth Asilomar Conference on, volume 1, Nov. 2002, pp. 341–345.

55. M. Grant and S. Boyd, "CVX: Matlab Software for Disciplined Convex Programming, version 2.2," `http://cvxr.com/cvx`, Jan. 2020.

56. J. Löfberg, "YALMIP : a toolbox for modeling and optimization in MATLAB," Proceedings of the IEEE International Conference on Robotics and Automation, Taipei, Taiwan, 2004, pp. 284–289. doi:10.1109/CACSD.2004.1393890.

57. T. Macnamara, "Simplified design procedures for Butler matrices incorporating 90deg hybrids or 180deg hybrids," *Proc. IEEE* **134**(1) (1987).